HOKKAIDO UNIVERSITY

Title	Histories of covariation between the Indian Monsoon and human-activities since the dawn of the civilized-era
Author(s)	渡邉, 貴昭
Degree Grantor	北海道大学
Degree Name	博士(理学)
Dissertation Number	甲第13580号
Issue Date	2019-03-25
DOI	https://doi.org/10.14943/doctoral.k13580
Doc URL	https://hdl.handle.net/2115/91644
Type	doctoral thesis
File Information	Takaaki_Watanabe.pdf

博士学位論文

Histories of covariation between the Indian Monsoon and human-activities since the dawn of the civilized-era
（文明黎明期以降のインド洋モンスーンと人類活動の共変遷史）

渡邉 貴昭
北海道大学大学院理学院
自然史科学専攻

Contents

Histories of covariation between the Indian Monsoon and human-activities since the dawn of the civilized-era

（文明黎明期以降のインド洋モンスーンと人類活動の共変遷史）

Abstract

Chapter 1 Introductions: A climate in the Indian Ocean is characterized by the Indian monsoon which seasonally varied direction and intensity. The Indian monsoon in summer and winter makes much precipitation in the India and western Asia, respectively. 1/3 peoples in the world's population live in the Indian Ocean rim and engage agricultures by utilizing monsoonal rainfall. Recent abrupt climate changes due to global-warming modulate Indian monsoon. And citizens would be affected from the modulated Indian monsoon. The interrelationships between Indian Ocean climate and human activities are important matter for revealing reasons of historical incidents and future constructions. However, it is poorly understood that the interrelationships between Indian monsoon and human society in India and western Asia.

Research objective of this thesis is revealing interrelationships between Indian monsoon and human activities. To discuss the relationships of the Indian monsoon and human society, it is necessary that long-term and seasonal-resolution records of Indian monsoon. Skeletons in reef corals provide monthly resolution records (e.g. SST, SSS and solar radiation), because they have high growth rate (> 1 cm/yr) relative to sediment core and stalagmite.

Chapter 2 Materials and methods: We used modern and fossil coral skeletons which were collected from the Arabian Sea and the Gulf of Oman. X-ray photos were taken from 5 mm thick sliced coral skeletons. Coral powder was collected at 0.4-0.5 mm interval along the maximum coral growth axis. Sr/Ca and isotope ratios in coral skeleton ($\delta^{13}C_{coral}$ and $\delta^{18}O_{coral}$) were measured using Inductivity coupled plasma optical emission spectrometer and mass spectrometer, respectively. We reconstructed biweekly SSTs from coral Sr/Ca ratios and calculated the oxygen isotopic composition of seawater ($\delta^{18}O_{SW}$) by subtracting the reconstructed Sr/Ca-SST from $\delta^{18}O_{coral}$.

Chapter 3 Western Indian Ocean upwelling uncouples from the Indian Ocean Dipole during the global-warming hiatus: The Indian Ocean Dipole (IOD) is a dominant climate mode in the Indian Ocean and has intensified with anthropogenic global-warming thorough 20th century. However, air-temperature observations reveal a global-warming hiatus since the late-1990s. It is unknown that influences of the global-warming hiatus on large-scale teleconnections of the IOD. To show these relationships, we used a 26-year long, biweekly record of Sr/Ca and $\delta^{18}O_{coral}$ from an Omani *Porites* coral. Our records reveal that a regime shift in $\delta^{18}O_{sw-anom}$ towards lower mean values occurs in 1999. Before the regime shift, higher SST_{anom} and $\delta^{18}O_{sw-anom}$ values are observed in the summer of positive-IOD years due to the weakened upwelling. This changes after 1999. The regime shift is associated with an intensified upwelling in the western Indian Ocean/Arabian Sea. This upwelling intensification dominates climate variability in the western Indian Ocean/Arabian Sea. While the impact of the IOD on upwelling reduces, the western Indian Ocean would uncouple from the IOD.

Chapter 4 Past summer upwelling events in the Gulf of Oman derived from a coral geochemical record: Previous data was difficult to reveal upwelling in the Gulf of Oman because SST and chlorophyll-a measurement by satellite did not reflect in situ SST variations. Coral records from the Gulf of Oman were applied for revealing the past upwelling. Our $\delta^{13}C_{coral}$ record shows sharp negative excursions in the summer, which correlate with known upwelling events. Using $\delta^{13}C_{coral}$ anomalies as a proxy for upwelling, we found 17 summer upwelling events occurred in the last 26 years. These anomalous negative excursions of $\delta^{13}C_{coral}$ result from upwelled water depleted in ^{13}C (dissolved inorganic carbon) and decreased water-column transparency. Our results suggest $\delta^{13}C_{coral}$ anomalies can be used as a proxy for seasonal upwelling intensity in the Gulf of Oman, which is driven by the Indian/Arabian Summer Monsoon, is subject to interannual variability.

Chapter 5 Indian monsoon reconstruction in the last millennium using fossil corals from the Arabian Sea: Summer Indian monsoon generate upwelling in the Arabian Sea and provide wet seasons in India during summer. We showed the relationships between upwelling and Indian precipitations using modern and fossil Arabian *Porites* corals. Summer negative excursions of SST and $\delta^{18}O_{sw}$ reflected inflow of seawater with enriched $^{16}O_{sw}$ from deep sea. SST deduced from Sr/Ca correlated with the northwestern Indian precipitations. Active evaporation in weak upwelling would transport much precipitations to India and increase Indian precipitations.▼ SST records from fossil corals in Medieval warm period to little ice age (LIA) were not different from the present. However, $\delta^{18}O_{sw}$ in summer of LIA was much lower than the present. Period of lower excursions of $\delta^{18}O_{sw}$ in LIA was shorter than the present. These suggest that upwelling in LIA would be shorter and stronger than the present. Upwelling in LIA would decrease precipitation in northwestern India and made prosperity empire in India.

Chapter 6 Fossil coral records revealed the relationships between monsoon variability and ancient civilizations: India and Mesopotamia civilization along the Indus and Tigris-Euphrates Rivers start to decline and abruptly collapsed around 4.2±0.2kyrBP, respectively. There was not revealed these climatic states in the era of transitions/collapse. Here, we present biweekly resolution coral records from 6 fossil corals of different time-windows from the present and 3.1 to 4.3 kyrBP using the Omani modern and fossil corals.

Fossil Omani corals suggested that summer SST and $\delta^{18}O_{sw}$ gradually decreased from 4.3 to 3.5 kyrBP. This suggested summer Indian monsoon intensified. The gradual intensification of summer Indian monsoon would affect on the Indian civilization. The Indian civilization could move their center of civilization as a response of gradual climate changes in wet seasons.

Winter SST and $\delta^{18}O_{sw}$ abruptly decreased in 4.2kyrBP. At the present, event of intensified wind (Shamal) makes difficult to keep their agricultural systems due to cold/dry air flow to the Mesopotamia region. Winter records from the Omani modern coral reflected frequent Shamal and this suggested anomalous climate in 4.2kyrBP on the Mesopotamia was induced by frequent Shamal. Our result suggested that the Akkad empire collapse would have been triggered by the agricultural failure and the social unrest in the Mesopotamia region caused by the frequent Shamal.

Chapter 7 General conclusions: On this thesis, summer and winter Indian monsoon were reconstructed in the transitions era of civilizations using the modern and fossil corals from the Gulf of Oman and the Arabian Sea. Monthly resolution records from corals would be powerful tools to compare of seasonal climate changes (wet-dry seasons) and lifestyle of human activity which varied in response to these climate changes. Coral should provide important records for revealing he relationships between climate event (or climate changes) and historical incidents.

1. Introductions of reef corals for paleo-environmental recorders and climate in Indian Ocean.

1-1 Historical human activities around the Indian Ocean

Humans established old civilizations on alluvium along the Hwang Ho, Indus, Nile and, Tigris-Euphrates rivers in the Holocene epoch [Macklin and Lewin, 2015]. Old civilizations prospered engaging in irrigation and rainfall agriculture utilizing seasonal changed river-flowrate and precipitations thorough the warming period in the Holocene epoch (so called Hypsithermal). By civilians developing agricultural systems, they established kingdom/empire in each region [Weiss et al., 1993, Possehi et al., 1997]. Rainwater in wet seasons, flood water from river or passing river water were needed to engaging agriculture in the old civilizations.

Civilizations in western Asia and India also developed in the Hypthisamal. Mesopotamia and Indus civilizations were prospered on the fertile crescent along the Tigris-Euphrates rivers. Indus civilizations were prospered on the Indus valley along the Indus river. First empire in the Mesopotamia region was established in 4.6 ka and collapsed in 4.2ka [Weiss et al., 1993]. Civilized center of Indus civilization was moved to upper stream of Indus river and Indus civilizations were disappeared from 4.2ka [Possehi et al., 1997] Egyptian and Huang civilizations were also declined in 4.2ka [Stanley et al., 2003, Li et al., 2009].

Civilizations collapse was remarked by paleo climatologist and archeologist. Civilizations declined or collapsed in the major cooling era, eg. 4.2kyBP and 300 years ago (little ice age). Old civilizations in 4.2kyBP might be affected by the abrupt climate changes [Weiss et al., 1993, Staubwasser et al., 2003, Stanley et al., 2003 Drysdale et al., 2006, Kathayat et al., 2017]. On the little ice age, social unrests and war (including civil-war) increased. Various paleo-climate proxies in wide regions suggested that abrupt climate event around 4.2 kyBP had an impact on their civilizations [Walker et al., 2012]. Because previous studies were based on low temporal resolution proxy, it would be difficult to compare with paleo-climate and human societies. It is necessary to reconstruct the paleoclimate in over seasonal-resolution proxy for revealing the lifestyle of agricultural-basin civilizations.

Recent temperature observations revealed that anthropogenic green-house gases's emission would increase the global temperature [Abram et al., 2016]. As an influence of the global warming, ocean-atmosphere interactions and atmosphere circulations in Indian Ocean (eg. Indian Ocean Dipole and Indian monsoon) would be emphasizing [Abram et al., 2008, Goes et al., 2005]. Influence of the global warming on the climate in the Indian Ocean are still important matter for future perspective. It is necessary to reconstruct the long-term records for revealing the anthropogenic influence on the Indian Ocean climate,

In this thesis, we revealed the inter-relationship between climate variability and human society based on long-term/high-temporal resolution records in the Arabian Sea, the Indian Ocean.

1-2 Climate in the Indian Ocean

Indian monsoon

Indian monsoon is important climate factor to sustain agriculture in the circum of the Indian Ocean. Indian monsoon is a wind which seasonally changes intensity and directions, and a climatic factor to dominate oceanographic- and atmospheric- environments in the Indian Ocean [Fig.1-5]. The northern Indian Ocean faces on the Asian continent with high mountain (Himalaya), and there is the southern Indian Ocean. This latitudinal topography caused a characteristic temperature and pressure gradient between the Asian continent and the Indian Ocean [Schott and McCreary 2001]. Indian monsoon is generated by this temperature gradient which seasonally varied due to a difference of isolations between northern and southern hemisphere [Goes et al., 2005]. Indian monsoon systems possibly control latitudinal positions of rainfall belt (Inter-tropical convergence zone: ITCZ) [Fig.1-5, Lechleitner et al., 2017]. Indian monsoons in winter and summer have an influence on agricultural areas in the India and the western Asia. Agricultural areas in circum of the Indian Ocean contributed to food securities in the world. The variations of Indian monsoon are essential information for developing a sustainable society [Kelly et al., 2015, Kathayat et al., 2017].

The summer Indian monsoon which brows from the Indian Ocean to the India is stronger than in winter and provides a rainy season (May-October, over 2000 mm/month) in the India. The summer Indian monsoon causes coastal upwelling which brings cooler temperatures, nitrified water to the sea surface along the southern coast of the Arabian Peninsula and Somalia [Brock et al., 1991, Fig.1-6]. The northern Arabian Sea is therefore one of the most productive areas in the world [Qasim et al., 1982].

In winter, the Indian monsoon brows from the Eurasia continent to the Indian Ocean. Winter monsoon is generally weaker than summer. Because winter monsoon brings the Mediterranean low to the western Asia, the winter monsoon was a source of rainfall in the west Asia [Cullen et al., 2000, Fleitmann et al., 2007].

Paleo-climate reconstructions in the Indian Ocean using coral archives

Paleo-climate reconstructions based on coral archives in the Indian Ocean are relatively rare to these in the Pacific and the Atlantic [Abram et al., 2016]. Monthly to seasonally proxy using corals were not existed in the northern and southern Indian Ocean through the Holocene to Anthropocene (Fig 1-8 and Table 1-1). Modern and fossil corals used in two previous reports were collected from equators in the western and eastern Indian Ocean (Seychells and Mentawaii: Zinke et al., 2014 and Abram et al., 2006). One report used modern and fossil corals from red sea which were far from the Indian Ocean and strongly affected by Atlantic climatic variability. Although there are important climatic factors such as Indian monsoon for human activity in the Indian Ocean, high-resolution records were still few. Here we first time reconstructed Indian monsoon in monthly resolutions using coral records.

1-3 Reef corals

Skeletons in reef building corals (coral) are widely used for high temporal resolution paleoclimate archives. live in surface-sea from tropic to temperate. Corals have various morphology of skeletons depended on habitat and species. Corals consist from tissue layer which covered by polyps on surface and Aragonite skeleton ($CaCO_3$) under the tissue layer. Aragonite skeletons precipitate in calcification space deduced to locate between tissues and skeletons.

As a characteristic of reef corals, they have zooxanthellae in polyps to form a symbiotic relationship. Corals can use photosynthetic products from zooxanthellae for calcifications and protection themselves. Corals get much energy from zooxanthellae, corals can accumulate their skeletons to upwards with high growth rate (> 10mm/year: *Porites*.sp.). Some massive corals (e.g. *Porites*) live in over 100 years old (eg. Watanabe et al., 2001, Zinke et al., 2004).

Coral growths are affected by *e.g.* seasonal variations of insolation and SST. Influence of insolation/SST on coral growth are reflected on extension rate and density of coral skeletons. By taken X-ray photo of coral-skeletons sliced in thin thickness (-1cm) or CT-scan of coral cores, seasonal variations of density are visualized (usually a couple of density band: annual band: Knutson et al., 1972, Lough and Barnes, 2000, Burgess et al., 2009). Counting couples of density band provides us age of corals and extension rate of coral [Shen et al., 2008, Burgess et al., 2009].

1-4 Proxies in reef corals

Coral skeletons have been used for paleo-climate recorder. Chemical compositions in coral skeletons reflect environmental variations in seawater. Non-radiogenic isotopic and elemental compositions in coral skeletons do not varied without diagenetic effect on coral skeletons (e.g. dissolutions, recrystallizing, and precipitation of calcite/aragonite cement: Hendy et al., 2007 Sayani et al., 2011). Skeletons of dead-corals were preserved as fossil coral. Fossil corals which preserved pristine aragonite skeleton were usable to reconstruct paleoclimate and to estimate age [Cobb et al., 2003, Watanabe et al., Abram et al., 2009]. We can get long term records (over 100 years) from corals which has long lifespans. Because corals have high growth rate, we can get 12 powder subsamples between a couple of density bands along the growth axis [Shen et al., 1996]. Corals provide over monthly resolution geochemical records.

Sr/Ca ratio in coral skeletons

Strontium/Calcium ratio in coral skeletons (Sr/Ca) is one of the most suitable SST proxies among trace-elements in coral skeletons, because Sr/Ca have been believed to reflect only SST variations [Smith et al., 1987, Shen et al., 1996, Inoue et al., 2007, Delong et al., 2016]. Sr^{2+} can replace Ca^{2+} in $CaCO_3$ and Sr^{2+} contain as Strontianite

in coral skeletal aragonite [Greegor et al., 1997]. Sr^{2+} is contain about 1/45-1/60 times lower than Ca^{2+} in coral skeleton [Okai et al., 2002]. Variations of coral skeletal Sr/Ca are negatively correlated with SST variations in the timing of precipitation [Smith et al., 1987: Fig. 1-1]. The published-slopes of SST-Sr/Ca regressions are ranges of from -0.04 to -0.08 mmol/mol/ºC [Correge,2006]. The averaged slope of SST-Sr/Ca dependency in coral is -0.06 (mmol/mol/ºC) which is similar with that in inorganic Aragonite [Dietzel et al., 2004, Kinsman and Holland, 1969]. Sr/Ca still have a problem to reconstruct the absolute SST due to different intercepts of SST-Sr/Ca thermometry among inorganic aragonite, the sample sites and coral species [Gaetani et al., 2011].

Oxygen and carbon stable isotopes in coral skeletons.

Oxygen and carbon stable isotopes in coral skeletons have been used for temperature and environmental proxies. Oxygen have three stable isotopic species (^{16}O, ^{17}O and ^{18}O). Two common species of oxygen isotope (^{16}O and ^{18}O) have been mainly used for environmental reconstruction. Carbon has two stable isotopic species (^{12}C and ^{13}C) and one radiogenic isotope (^{14}C: radio carbon). Two common species (^{12}C and ^{13}C) have been mainly used for environmental reconstruction. One radiogenic isotope is used for age determinations of coral skeletons.

Delta value of oxygen or carbon isotope ratio is defined as a following equation using referenced carbonate made from Belemnite on PeeDee formations at State of South Carolina, the USA.

$$\delta_{VPDB} (‰_{VPDB}) = (R_{sample} - R_{PDB}) / R_{PDB} *1000$$

$$*R = {}^{18}O/{}^{16}O \text{ or } {}^{13}C/{}^{12}C$$

Coral skeletons are precipitated in isotopic disequilibrium with ambient seawater as a result of vital effects [McConnaughey, 1989a, Fig.1-2]. In the coral with low growth rate, the kinetic effect was dominant relative to the vital effect of isotopes. The kinetic effect selectively depletes ^{12}C and ^{16}O in coral skeletons and is particularly important when coral growth rates are very low (< 2 mm per year) [McConnaughey, 1989a]. Select of measurement line was also influenced on coral growth rate on measurement line and isotopic results [McConnaughey, 1989a, Cohen and Hart, 1997]. To get appropriate isotope values, maximum growth of corals should be select for analytical lines.

Oxygen isotopes in coral skeletons

Variations of $\delta^{18}O_{coral}$ are combinations of both variations of SST and hydrological cycles [Watanabe et al., in pres Fig.1-1]. Previous studies reported oxygen isotope ratio in carbonate strongly influenced by temperature in the timing of calcification [Kim and O'Neil, 1997, Kim et al., 2007]. And, oxygen isotope in H_2O is also affected on oxygen isotope in carbonate, because carbonate use H_2O in calcification processes. In the case of corals, oxygen isotope in seawater ($\delta^{18}O_{SW}$) is affected on $\delta^{18}O_{coral}$. $\delta^{18}O_{SW}$ are changed by hydrological cycles (precipitations-

evaporations balances, freshwater input and upwelling: Delaygue, 2000,). Variations of $\delta^{18}O_{SW}$ (hydrological cycles) can be known by subtracting the SST contribution inferred from the Sr/Ca ratio from $\delta^{18}O_{coral}$ [Gagan et al.,1998, Ren et al., 2002, Yudawati et al., 2008].

Carbon isotope in coral skeletons

Controlling factors of stable isotopes of carbon in coral skeletons ($\delta^{13}C_{coral}$) are more complex than $\delta^{18}O_{coral}$. $\delta^{13}C_{coral}$ are influenced by (1) kinetic effect [McConnaughey, 1989a, Fig.1-2] (2) vital effect [McConnaughey, 1989b, Watanabe et al., in pres. Fig.1-3], (3) variation of $\delta^{13}C_{DIC-SW}$ [McConnaughey, 1989a; McConnaughey, 1989b; Swart et al 1996; Abram., et al 2003] and (4) autotroph/heterotroph ratios [Grottoli and Wellington, 1999, Grottoli, 2002] (Fig.1-4).
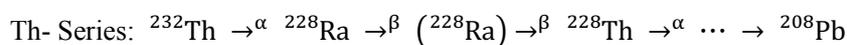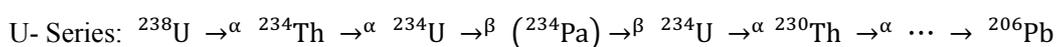
(1) Kinetic effect was dominated in low growth rate. (2) Photosynthetic activities of zooxanthellae affect $\delta^{13}C_{coral}$ by changing the carbon isotopes in the internal dissolved inorganic carbon pool of the coral [Fairbanks and Dodge, 1979]. Therefore, $\delta^{13}C_{coral}$ are used for proxy of insolation and turbidity. A 50% weakening of solar radiation induces a decrease of approximately $0.5‰_{VPDB}$ in $\delta^{13}C_{coral}$ [Grottoli, 2002]. The amount of solar radiation received by the coral varies depending on incoming solar radiation, cloud cover and water transparency [Fairbanks and Dodge 1979; Pätzold, 1984; Wellington and Dunbar,1995]. Water transparency are changed by high turbidity due to sediment and high primary-productions. (3) Carbon isotope in dissolved inorganic carbon in seawater ($\delta^{13}C_{DIC-SW}$) affected on $\delta^{13}C_{coral}$ [Nozaki et al., 1978, Swart et al., 2010] because DIC in seawater are entered into calcification spaces for using coral calcification [McConnaughey, 1989b]. $\delta^{13}C_{DIC-SW}$ varies by eg. enriched anthropogenic-CO_2 from fossil fuels in air and inflow of upwelling water from deep-sea [Swart et a.,1996] (4) ^{13}C-depleted zooplanktons fed by corals also decrease coral $\delta^{13}C_{coral}$ because low $\delta^{13}C$ in zooplankton (< -20 ‰) decrease $\delta^{13}C$ in DIC-pool of coral [Grottoli and Wellington, 1999, Felis et al., 1999].

Age determinations.

We can know ages of coral skeletons from chemical compositions with half-life. Coral skeletons contain radiogenic isotopes (Uranium and Thorium series, and ^{14}C). We can get age of coral to measure concentrations of Uranium (U) and Thorium (Th) series, or ^{14}C.

Uranium-Thorium age determinations

Simultaneous measurement of U and Th series provided us the absolute ages of coral (U-Th age).

$$U\text{- Series: } ^{238}U \to^{\alpha} {}^{234}Th \to^{\alpha} {}^{234}U \to^{\beta} \left(^{234}Pa\right) \to^{\beta} {}^{234}U \to^{\alpha} {}^{230}Th \to^{\alpha} \cdots \to {}^{206}Pb$$

$$Th\text{- Series: } ^{232}Th \to^{\alpha} {}^{228}Ra \to^{\beta} \left(^{228}Ra\right) \to^{\beta} {}^{228}Th \to^{\alpha} \cdots \to {}^{208}Pb$$

$$(\to^{\alpha} \text{ and } \to^{\beta}: \text{Alpha and beta decay, respectively})$$

Parent of U-series (238U) decays to ^{234}U and ^{230}Th. Age of coral skeletons is basically known from these three isotopes of U-series (^{238}U, ^{234}U and ^{230}Th). Accuracy of U-Th age get higher by applying earlier coral specimens (eg. Accuracy of U-Th age for corals: 9.6 years ago coral: ±0.45 year, 6883 years ago: ±19 year: Shen et al., 2012). By measuring parent of Th series (^{232}Th), we correct the secondary input of ^{230}Th. Th is enriched in solidus and easy to contaminate into coral skeletons. U-Th age should be used with note the initial uranium isotopic ratio ($\delta^{234}U_{initial}$) in coral skeletons, because coral skeletons was "semi-closed system" about U series (Shen et al., 2008). Uranium isotopes could escape from aragonite skeletons (α-recoil) in long preservation times (>100kyr: Thomson et al., 2003).

Radiocarbon isotopes

Radiocarbon dating technique provided us relative age of any specimens containing carbon. ^{14}C decayed to ^{14}N with half-life (5568 year). We can estimate the age from ^{14}C concentration in the specimens. Concentrations of ^{14}C in atmosphere and ocean vary with geomagnetic, solar modulation of the cosmic-ray flux and the carbon cycles (reservoir effect). Because ^{14}C in environment is increased due to dramatical increase of artificial radiations around World War II (CE1945), ages are reported relative to CE1950 (before present: BP). To get accurate relative-age, we need to correct the reservoir effect by comparing absolute ages with ^{14}C ages (eg. Tahiti IODP corals, Barbados corals, Cariaco varved and Hulu cave speleothems: IntCal13, Reimer et al., 2013). Because we can apply any specimens with carbon, we get relative age of wide range of specimens (eg. wooden samples, carbonates: Weiss et al., 1993).

1-5 Sampling locations

the Gulf of Oman

The Gulf of Oman is located on the northeastern coast of the Arabian Peninsula and both the Arabian Sea and the Gulf of Oman are located in arid environments. Summer upwelling in in the Gulf of Oman was reported by the logger-based SST and in situ nutrient measurement. The driving factor of upwelling was considered that the upwelled water flows northward, and gyres and eddy systems sweep into the Oman Sea [Al-Azri et al., 2010]. In the Gulf of Oman, Satellite based sea surface temperature (SST) in the Gulf of Oman did not reflect low SST excursions in summer measured by CTDs. (Fig.1-7). Long-term and *in situ* records of primary production, salinity and temperature are necessary in order to understand upwelling events and ocean-atmospheric interaction in the northwestern Indian Ocean.

the Mashira Island

The Mashira island locates along the southern coast of the Arabian Peninsula. The southern coast of the Arabian Peninsula is directly affected by the coastal upwelling in summer triggered by summer Indian Monsoon [Qasim,

1982, Tudhope et al., 1996]. This upwelling brings cold seawater mass with high nutrient. Due to upwelling, summer SST (June to September) decreases similar values with winter SST. Because of high nutrient water mass came from upwelling, the Arabian Sea in summer is one of the highest primary productive oceans in tropics.

1-6 research objectives and structure of this thesis

General research objective in this thesis is revealing the relationships between historical human activities and climate changes.

First section is that revealing how the large-scales ocean-atmosphere circulations in the Indian ocean (Indian Ocean dipole) are affected from both the anthropogenic global-warming and nature global-warming hiatus. Although global warming due to anthropogenic CO_2 emissions would affect on the ocean-atmosphere circulations in global-scales, the reduction of global warming trend was confirmed from last 1990s to mid-2010s due to shift change of SST patterns in the Pacific. We discuss influence of global-warming trend/hiatus on the Indian monsoon and Indian Ocean dipole on Chapter 3.

Second is that establishing calibration using modern coral in the Gulf of Oman to reconstruct past upwelling (Chapter 4,5). In previous studies, calibration works were conducted in corals from various sample sites. However, there are no exists of coral records from the Gulf of Oman [Fig. 1-6]. And $\delta^{18}O_{sw}$ both Sr/Ca and $\delta^{18}O_c$ records are not established in the Arabian Sea, although salinity proxy would be important for detecting the past upwelling.

Third section is that revealing relationships historical human activities and climate changes. Humans developed agriculture utilizing monsoonal rainwater. Water sources should be varied by the seasonal Indian monsoon fluctuations. However, previous studies which discussed past human history were based on low-temporal resolution records (eg. speleothems and sediment cores). We revealed these relationships based on monthly resolution climate records to reconstruct a seasonal variability of Indian monsoon.

Finally (chapter 7), the key points are summarized, and my future perspective is discussed.

Reference

1. Abram, N. J. et al. Early onset of industrial-era warming across the oceans and continents. Nature 536, 411–418 (2016).

2. Abram, N. J., Gagan, M. K., McCulloch, M. T., Chappell, J. & Hantoro, W. S. Coral reef death during the 1997 Indian Ocean Dipole linked to Indonesian wildfires. Science 301, 952–955 (2003).

3. Abram, N., Webster, J., Davies, P. & Dullo, W. Biological response of coral reefs to sea surface temperature variation: Evidence from the raised Holocene reefs of Kikai-jima (Ryukyu Islands, Japan). Coral Reefs 20, 221–234 (2001).

4. Al-Azri, A. R., Piontkovski, S. A., Al-Hashmi, K. A., Goes, J. I. & Do Gomes, H. R. Chlorophyll a as a measure of seasonal coupling between phytoplankton and the monsoon periods in the Gulf of Oman. Aquat. Ecol. 44, 449–461 (2010).

5. Beck, J. W. et al. Sea-Surface Temperature from Coral Skeletal Strontium/Calcium Ratios. Science (80-.). 257, 644–647 (1992).

6. Brock, J. C. & McClain, C. R. Interannual variability in phytoplankton blooms observed in the northwestern Arabian Sea during the southwest monsoon. J. Geophys. Res. 97, 733 (1992).

7. Burgess, S. N., McCulloch, M. T., Mortimer, G. E. & Ward, T. M. Structure and growth rates of the high-latitude coral: Plesiastrea versipora. Coral Reefs 28, 1005–1015 (2009).

8. Cahyarini, S. Y., Pfeiffer, M., Timm, O., Dullo, W. & Schönberg, D. G. Reconstructing seawater δ18O from paired coral δ18O and Sr/Ca ratios: Methods, error analysis and problems, with examples from Tahiti (French Polynesia) and Timor (Indonesia). Geochim. Cosmochim. Acta 72, 2841–2853 (2008).

9. Cohen, A. L. & Hart, S. R. The effect of colony topography on climate signals in coral skeleton. Geochim. Cosmochim. Acta 61, 3905–3912 (1997).

10. Corrège, T. Sea surface temperature and salinity reconstruction from coral geochemical tracers. Palaeogeogr. Palaeoclimatol. Palaeoecol. 232, 408–428 (2006).

11. Crueger, T., Zinke, J. & Pfeiffer, M. Patterns of Pacific decadal variability recorded by Indian Ocean corals. Int. J. Earth Sci. 98, 41–52 (2009).

12. Cullen, H. M. et al. Climate change and the collapse of the Akkadian empire: Evidence from the deep sea. Geology 28, 379 (2000).

13. DeLong, K. L., Quinn, T. M., Taylor, F. W., Shen, C. & Lin, K. Improving coral-base paleoclimate reconstructions by replicating 350years of coral Sr/Ca variations. Palaeogeogr. Palaeoclimatol. Palaeoecol. 373, 6–24 (2013).

14. Dietzel, M., Gussone, N. & Eisenhauer, A. Co-precipitation of Sr2+and Ba2+with aragonite by membrane diffusion of CO2between 10 and 50 °C. Chem. Geol. 203, 139–151 (2004).

15. Drysdale, R. et al. Late Holocene drought responsible for the collapse of Old World civilizations is recorded in an Italian cave flowstone. 101–104 (2006). doi:10.1130/G22103.1

16. Fairbanks, R. G. & Dodge, R. E. Annual periodicity of the 18O/16O and 13C/12C ratios in the coral Montastrea annularis. Geochim. Cosmochim. Acta 43, 1009–1020 (1979).

17. Felis, T. et al. Increased seasonality in Middle East temperatures during the last interglacial period. Nature 429, 164–168 (2004).

18. Felis, T., Pätzold, J., Loya, Y. & Wefer, G. Vertical water mass mixing and plankton blooms recorded in skeletal stable carbon isotopes of a Red Sea coral. J. Geophys. Res. 103, 30731 (1998).

19. Fleitmann, D. et al. Holocene ITCZ and Indian monsoon dynamics recorded in stalagmites from Oman and Yemen (Socotra). Quat. Sci. Rev. 26, 170–188 (2007).

20. Gagan, M. K. et al. Temperature and Surface-Ocean Water Balance of the Mid-Holocene Tropical Western Pacific. Science 279, 1014–1018 (1998).

21. Goes, J. I., Thoppil, P. G., Gomes, H. R. & Fasullo, J. T. Warming of the Eurasian Landmass Is Making the Arabian Sea More Productive. Science (80-.). 308, 545–547 (2005).

22. Greegor, R. B., Pingitore, N. E. & Lytle, F. W. Strontianite in coral skeletal aragonite. Science 275, 1452–1454 (1997).

23. Grottoli, A. Effect of light and brine shrimp on skeletal δ13C in the Hawaiian coral Porites compressa: a tank experiment. Geochim. Cosmochim. Acta 66, 1955–1967 (2002).

24. Grottoli, a. G. & Wellington, G. M. Effect of light and zooplankton on skeletal δ13C values in the eastern Pacific corals Pavona clavus and Pavona gigantea. Coral Reefs 18, 29–41 (1999).

25. Hendy, E. J., Gagan, M. K., Lough, J. M., McCulloch, M. & DeMenocal, P. B. Impact of skeletal dissolution and secondary aragonite on trace element and isotopic climate proxies in Porites corals. Paleoceanography 22, 4 (2007).

26. Hennekam, R. et al. Cocos (Keeling) Corals Reveal 200 Years of Multidecadal Modulation of Southeast Indian Ocean Hydrology by Indonesian Throughflow. Paleoceanogr. Paleoclimatology 33, 48–60 (2018).

27. Inoue, M., Suzuki, A., Nohara, M. & Hibino, K. Empirical assessment of coral Sr / Ca and Mg / Ca ratios as climate proxies using colonies grown at different temperatures. 34, 2–5 (2007).

28. Janowiak, J. E. and P. Xie, CAMS_OPI: A Global Satellite-Rain Gauge Merged Product for Real-Time Precipitation Monitoring Applications. J. Climate, 12, 3335-3342 (1999).

29. Kajita, H. et al. Holocene sea surface temperature variations recorded in corals from Kikai Island, Japan. Geochem. J. 51, 9–14 (2017).

30. Kathayat, G. et al. The Indian monsoon variability and civilization changes in the Indian subcontinent. Sci. Adv. 3, e1701296 (2017).

31. Kelley, C. P., Mohtadi, S., Cane, M. A., Seager, R. & Kushnir, Y. Climate change in the Fertile Crescent and implications of the recent Syrian drought. Proc. Natl. Acad. Sci. 112, 3241–3246 (2015).

32. Kim, S. T., O'Neil, J. R., Hillaire-Marcel, C. & Mucci, A. Oxygen isotope fractionation between synthetic aragonite and water: Influence of temperature and Mg^{2+} concentration. Geochim. Cosmochim. Acta 71, 4704–4715 (2007).

33. Kim, S.-T. & O'Neil, J. R. Equilibrium and nonequilibrium oxygen isotope effects in synthetic carbonates. Geochim. Cosmochim. Acta 61, 3461–3475 (1997).

34. Cobb, K. M., Charles, C. D., Cheng, H. & Edwards, R. L. El Niño/Southern Oscillation and tropical Pacific climate during the last millennium. *Nature* **424,** 271–276 (2003).

35. Kinsman, D. J. J. & Holland, H. . The co-precipitation of cations with $CaCO_3$—IV. The co-precipitation of Sr^{2+} with aragonite between 16° and 96°C. Geochim. Cosmochim. Acta 33, 1–17 (1969).

36. Knutson, D. W., Buddemeier, R. W., & Smith, S. V. Coral chronometers: seasonal growth bands in reef corals. Science, 177(4045), 270-272 (1972).

37. Lechleitner, F. A. et al. Tropical rainfall over the last two millennia: evidence for a low-latitude hydrologic seesaw. Sci. Rep. 7, 45809 (2017).

38. Li, X., Dodson, J., Zhou, J. & Zhou, X. Increases of population and expansion of rice agriculture in Asia, and anthropogenic methane emissions since 5000BP. Quat. Int. 202, 41–50 (2009).

39. Lough, J. M. & Barnes, D. J. Environmental controls on growth of the massive coral Porites. J. Exp. Mar. Bio. Ecol. 245, 225–243 (2000).

40. Macklin, M. G. & Lewin, J. The rivers of civilization. Quat. Sci. Rev. 114, 228–244 (2015).

41. McConnaughey, T. 13C and 18O isotopic disequilibrium in biological carbonates : I. Patterns. Geochim. Cosmochim. Acta 53, 151–162 (1988).

42. McConnaughey, T. 13C and 18O isotopic disequilibrium in biological carbonates: II. In vitro simulation of kinetic isotope effects. Geochim. Cosmochim. Acta 53, 163–171 (1989).

43. McCulloch, M. T et al.. Coral Record of Equatorial Sea-Surface Temperatures During the Penultimate Deglaciation at Huon Peninsula. Science (80-.). 283, 202–204 (1999).

44. Nozaki, Y., Rye, D. M., Turekian, K. K. & Dodge, R. E. A 200 year record of carbon-13 and carbon-14 variations in a Bermuda coral. Geophys. Res. Lett. 5, 825–828 (1978).

45. O'Reilly, et al. SeaWiFS postlaunch calibration and validation analyses, part 3. NASA tech. memo 206892.11: 3-8 (2000).

46. Okai, T., Suzuki, A., Kawahata, H., Terashima, S. & Imai, N. Preparation of a New Geological Survey of Japan Geochemical Reference Material: Coral JCp-1. Geostand. Geoanalytical Res. 26, 95–99 (2002).

47. Pätzold, J. Growth rhythms recorded in stable isotopes and density bands in the reef coral Porites lobata (Cebu, Philippines). Coral Reefs 3, 87–90 (1984).

48. Pfeiffer, M., Timm, O., Dullo, W. & Podlech, S. Oceanic forcing of interannual and multidecadal climate variability in the southwestern Indian Ocean: Evidence from a 160 year coral isotopic record (La Réunion, 55°E, 21°S). Paleoceanography 19, n/a-n/a (2004).

49. Possehl, G. L. The transformation of the Indus Civilization. J. World Prehistory 11, 425–472 (1997).

50. Qasim, S. Z. Oceanography of the northern Arabian Sea. Deep Sea Res. Part A. Oceanogr. Res. Pap. 29, 1041–1068 (1982).

51. Quinn, T. M., Taylor, F. W., Crowley, T. J. & Link, S. M. Evaluation of sampling resolution in coral stable isotope records: A case study using records from New Caledonia and Tarawa. Paleoceanography 11, 529–542 (1996).

52. Reimer, P. J. et al. IntCal13 and Marine13 Radiocarbon Age Calibration Curves 0–50,000 Years cal BP. Radiocarbon 55, 1869–1887 (2013).

53. Ren, L., Linsley, B. K., Wellington, G. M., Schrag, D. P. & Hoegh-guldberg, O. Deconvolving the δ18O seawater component from subseasonal coral δ18O and Sr/Ca at Rarotonga in the southwestern subtropical Pacific for the period 1726 to 1997. Geochim. Cosmochim. Acta 67, 1609–1621 (2003).

54. Reynolds, R.W., N.A. Rayner, T.M. Smith, D.C. Stokes, and W. Wang, An Improved In Situ and Satellite SST Analysis for Climate. J. Climate, 15, 1609-1625 (2002).

55. Sayani, H. R. et al. Effects of diagenesis on paleoclimate reconstructions from modern and young fossil corals. 75, 6361–6373 (2011).

56. Schott, F. A. & McCreary, J. P. The monsoon circulation of the Indian Ocean. Prog. Oceanogr. 51, 1–123 (2001).

57. Shen, C. et al. High-precision and high-resolution carbonate 230Th dating by MC-ICP-MS with SEM protocols. Geochim. Cosmochim. Acta 99, 71–86 (2012).

58. Shen, C. et al. Variation of initial 230Th/232Th and limits of high precision U–Th dating of shallow-water corals. Geochim. Cosmochim. Acta 72, 4201–4223 (2008).

59. Shen, C.-C. et al. The calibration of D[Sr/Ca]versus sea surface temperature relationship for Porites corals. Geochimica et Cosmochimica Acta 60, 3849–3858 (1996).

60. Smith, S. V., Buddemeier, R. W., Redalje, R. C. & Houck, J. E. Strontium-Calcium Thermometry in Coral Skeletons. Science (80-.). 204, 404–407 (1979).

61. Stanley, J., Krom, M. D., Cliff, R. A. & Woodward, J. C. Short contribution: Nile flow failure at the end of the Old Kingdom, Egypt: Strontium isotopic and petrologic evidence. Geoarchaeology 18, 395–402 (2003).

62. Staubwasser, M., Sirocko, F., Grootes, P. M. & Segl, M. Climate change at the 4 . 2 ka BP termination of the Indus valley civilization and Holocene south Asian monsoon variability. 30, 3–6 (2003).

63. Swart, P. K. et al. The 13 C Suess effect in scleractinian corals mirror changes in the anthropogenic CO 2 inventory of the surface oceans. 37, 1–5 (2010).

64. Swart, P. K., Leder, J. J., Szmant, a. M. & Dodge, R. E. The origin of variations in the isotopic record of scleractinian corals: II. Carbon. Geochim. Cosmochim. Acta 60, 2871–2885 (1996).

65. Thompson, W. G., Spiegelman, M. W., Goldstein, S. L. & Speed, R. C. An open-system model for U-series age determinations of fossil corals. 210, 365–381 (2003).

66. Tierney, J. E. et al. Tropical sea surface temperatures for the past four centuries reconstructed from coral archives. Paleoceanography 30, 226–252 (2015).

67. Tudhope, A. W., Lea, D. W., Shimmield, G. B., Chilcott, C. P. & Head, S. Monsoon Climate and Arabian Sea Coastal Upwelling Recorded in Massive Corals from Southern Oman. Palaios 11, 347 (1996).

68. Walker, M. J. C. et al. Formal subdivision of the Holocene Series/Epoch: a Discussion Paper by a Working Group of INTIMATE (Integration of ice-core, marine and terrestrial records) and the Subcommission on Quaternary Stratigraphy (International Commission on Stratigraphy). J. Quat. Sci. 27, 649–659 (2012).

69. Watanabe, T., Winter, A. & Oba, T. Seasonal changes in sea surface temperature and salinity during the Little Ice Age in the Caribbean Sea deduced from Mg/Ca and 18O/16O ratios in corals. Mar. Geol. 173, 21–35 (2001).

70. Watanabe, T. *et al.* Permanent El Niño during the Pliocene warm period not supported by coral evidence. *Nature* **471,** 209–211 (2011).

71. Weiss, H. et al. The Genesis and Collapse of Third Millennium North Mesopotamian Civilization. Science (80-.). 261, 995–1004 (1993).

72. Wellington, G. M. & Dunbar, R. B. Stable isotopic signature of El Niño Southern Oscillation events in eastern tropical pacific reef corals. Coral Reefs 14, 5–25 (1995).

73. YAMAZAKI, A. et al. Reconstructing palaeoenvironments of temperate regions based on high latitude corals at Tatsukushi Bay in Japan. J. Japanese Coral Reef Soc. 11, 91–107 (2009).

74. Zinke, J., Dullo, W.-C., Heiss, G. A. & Eisenhauer, A. ENSO and Indian Ocean subtropical dipole variability is recorded in a coral record off southwest Madagascar for the period 1659 to 1995. Earth Planet. Sci. Lett. 228, 177–194 (2004).
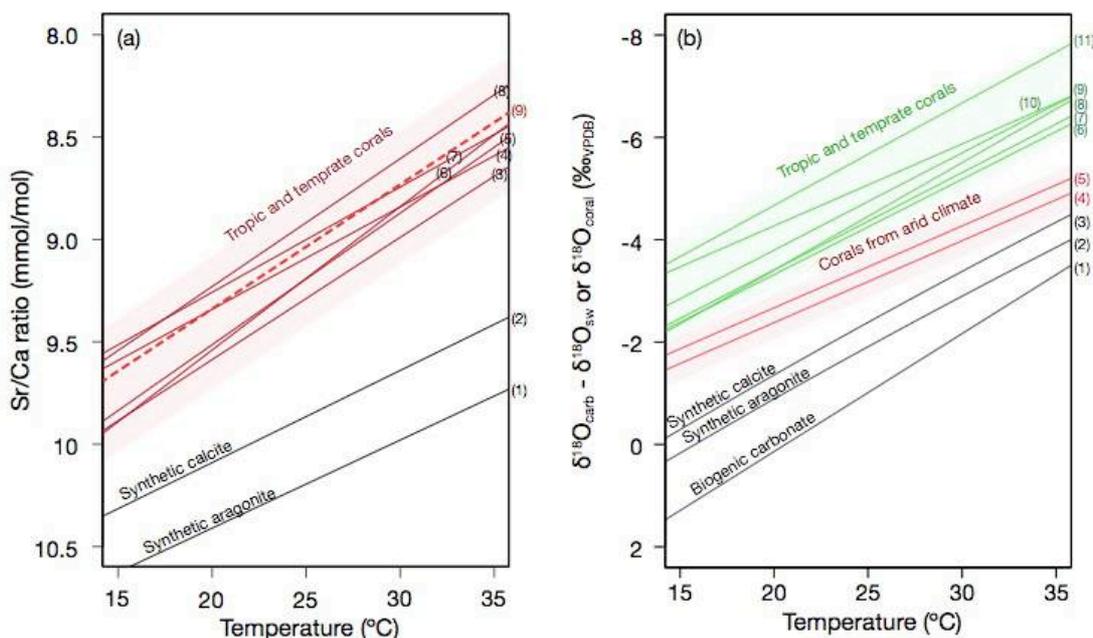
Fig. 1-1

(a) SST dependency of Sr/Ca ratios

Inorganic aragonite: (1) Dietzel et al., 2004, (2) Kinsman and Holland, 1969 (3) Gulf of Eilat (Felis et al., 2004) (4) Myotte (Zinke et al., 2004) (5) Kikai island (Kajita et al., 2017) (6) Various locations (Smith et al., 1979) (7)Taiwan (Shen et al., 1996) (8) New Caledonia (Beck et al., 1992), (9) Averaged in published slopes (Correge, 2006)

(b) SST dependency of oxygen isotope

$\delta^{18}O$ in inorganic carbonate subtracting by $\delta^{18}O_{sw}$: (1) Biogenic carbonate: Grossman and Ku,1986 (2) Synthetic aragonite: Kim et al., 2007 (3) Synthetic calcite: Kim and O'Neil, 1997, $\delta^{18}O$ in *Porites* coral from arid climate (red line): (4) Gulf of Eilat, Red sea (Watanabe et al., in pres.), (5) Gulf of Eilat, Red sea (Felis et al., 2004), $\delta^{18}O$ in *Porites* coral from tropic or temprate climate (green line): (6) Kikai island, northwestern Pacific (Abram et al., 2001), (7) Madagascar, south western Indian ocean (Zinke et al., 2004), (8) La Réunion, south western Indian ocean (Pfeiffer et al., 2004), (9)New Caledonia, southwestern Pacific (Quinn et al., 1996), (10)Kochi, northwestern Pacific (Yamazaki et al., 2009), (11) Okinawa, northwestern Pacific (Watanabe et al in pres).
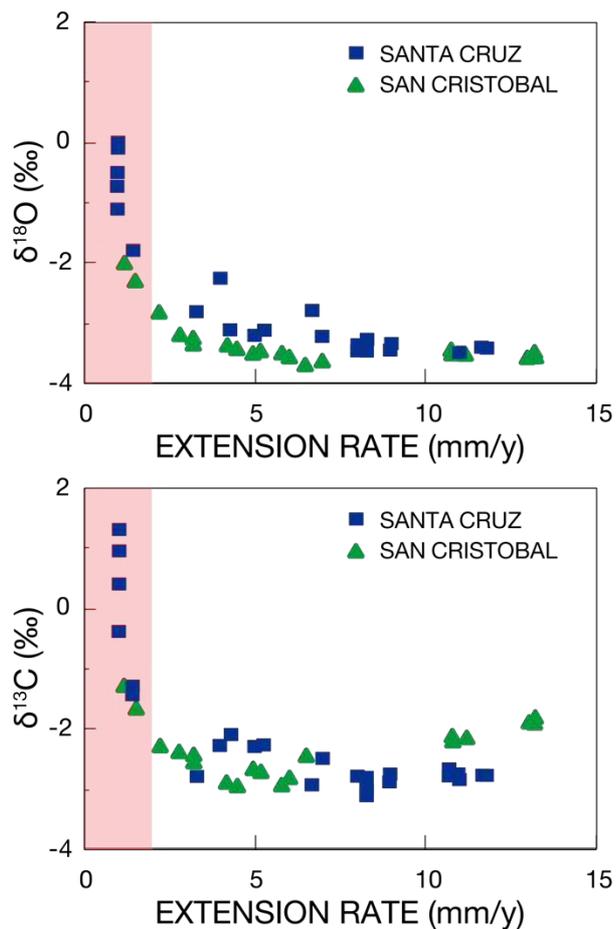
Fig. 1-2

Crossplots between coral skeletal isotopes ($\delta^{18}O$: top, $\delta^{13}C$: bottom) and extension rate. Coral samples were collected from Santa Cruz (blue dot) and San Cristobal (green triangle), Galapagos archipelago. Red colored area showed under 2mm/year extension rate. Figure was modified from McConnaughey,1989a
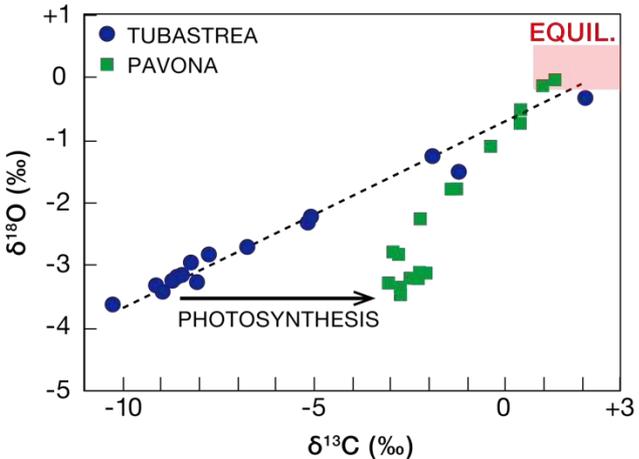
22

Fig. 1-3

Isotopic comparison between the photosynthetic coral (*Pavona clavus*: green square) and the non-photosynthetic coral (*Tubastrea sp.*: blue circle). Figure was modified from McConnaughey,1989a
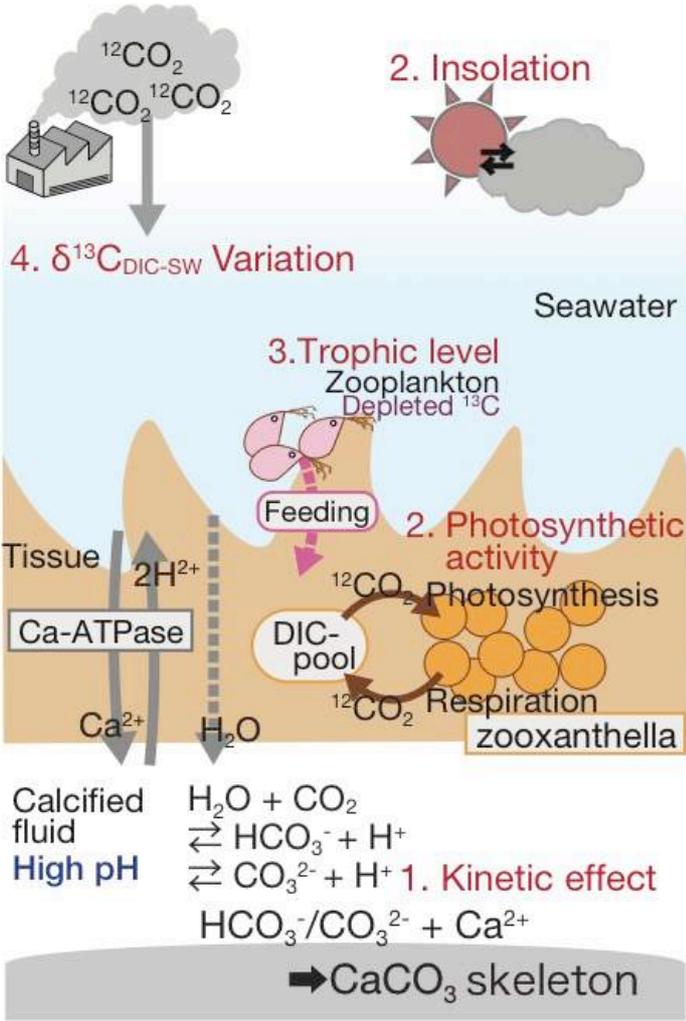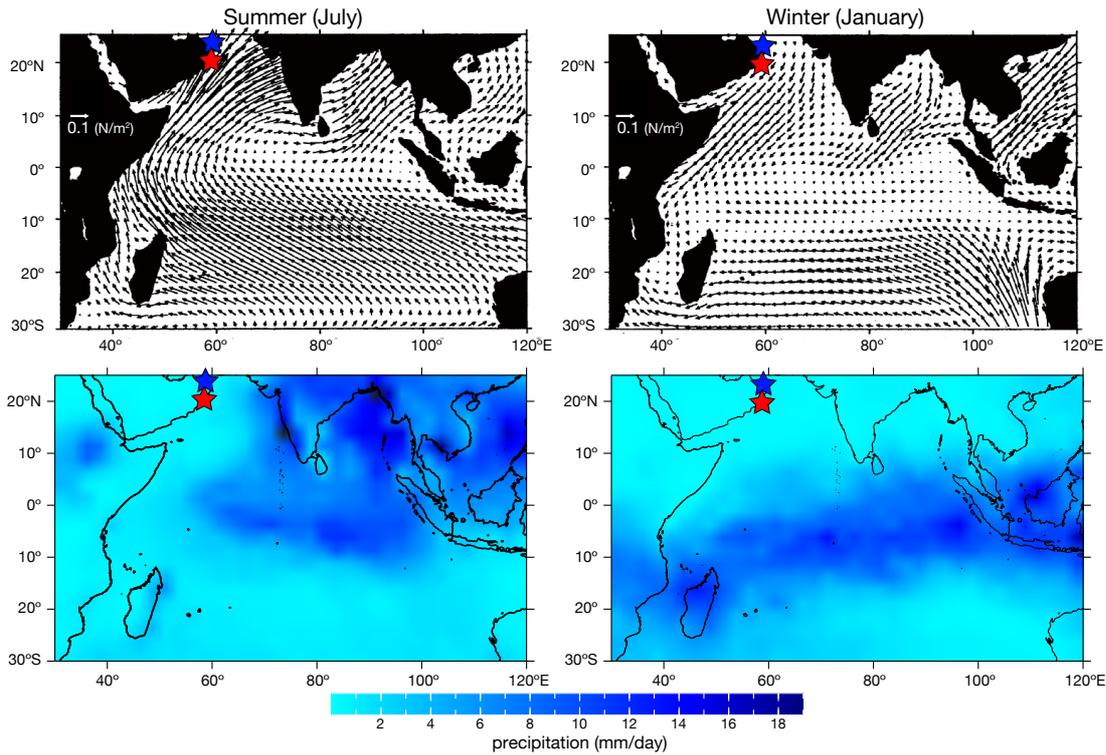
Fig. 1-4

Variation factors of $\delta^{13}C_{coral}$ described on schematic figure.
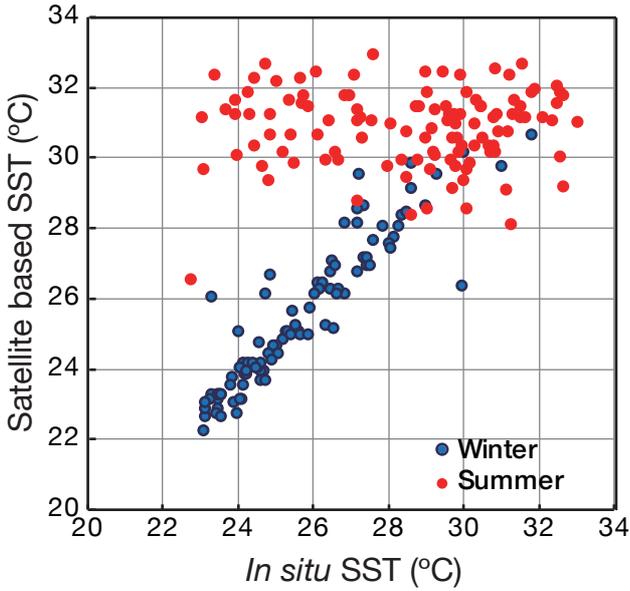
Figure.1-5

Distribution map of wind directions and speed in summer (July) and winter (January). Contour maps of rainfall in July and January. Longer arrows shows stronger wind (a and c), and deeper blue indicates higher precipitation in each month (b and d). Wind distribution maps are modified from Schott and McCreary, 2001. Precipitation data was averaged values in July and January over 1980-2017 and provided from CAMS OPI dataset. Blue and red stars indicate sample sites of Omani and Arabian corals, respectively.
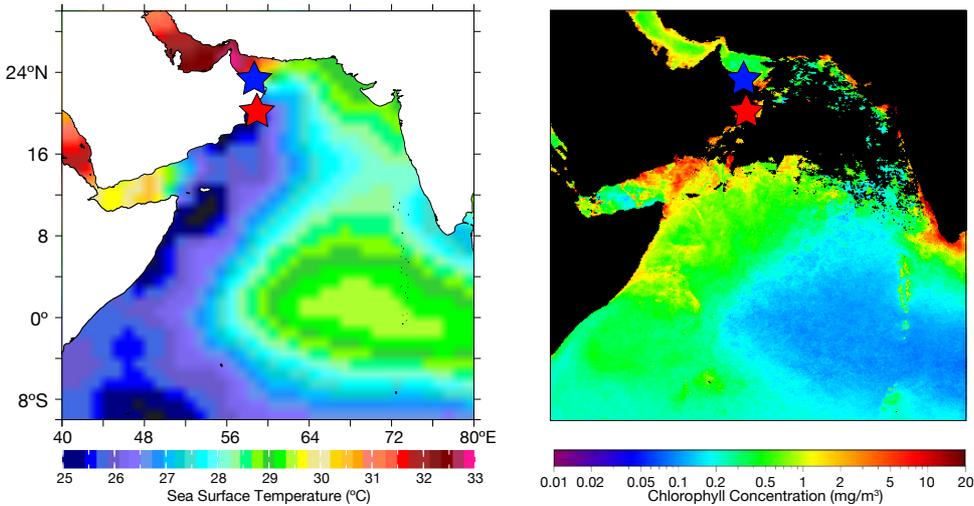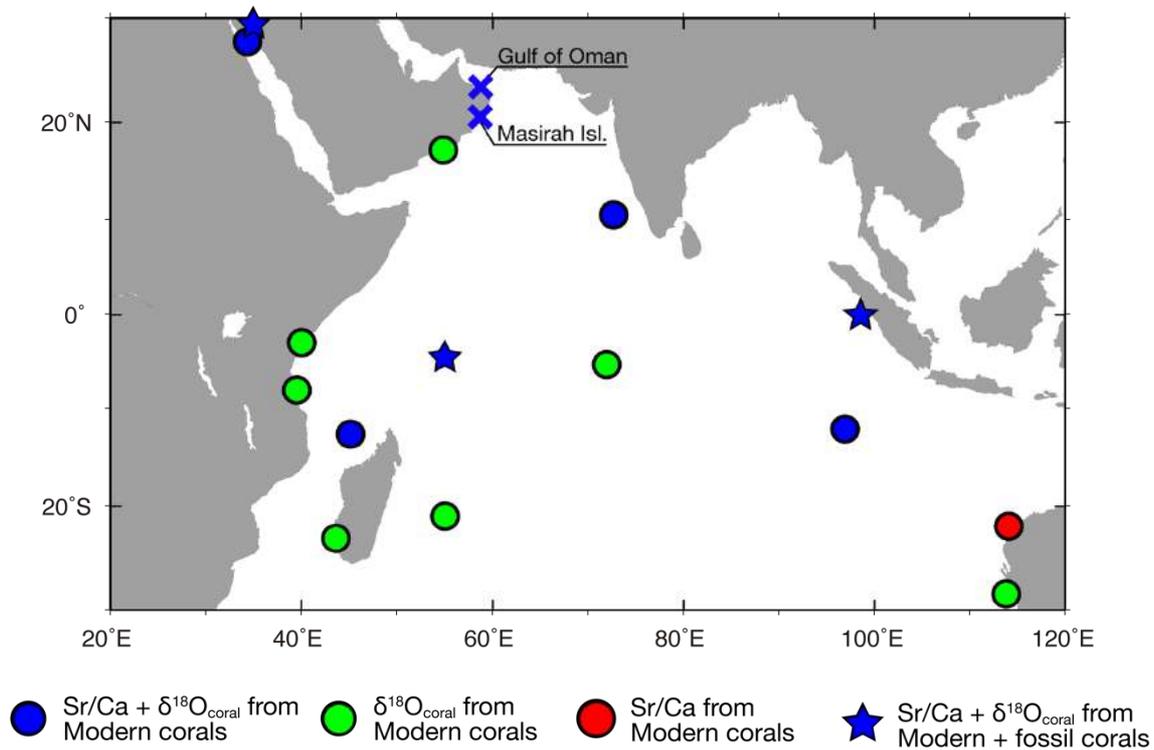
Figure.1-6

Contour maps of SST and densities of chlorophyll-a in July. SST and densities of chlorophyll-a data were provided by COADS and SeaWifs, respectively [Reynolds et al., 2002, O'Reilly et al., 2001]. SST and chlorophyll-a were averaged over 1982-2017 and 1992-2017, respectively. Blue and red stars indicate sample sites of Omani and Arabian corals, respectively.

Figure. 1-7

Scatterplot of SST measured by CTD vs. SST based on satellite in the Gulf of Oman for 10 years. Winter SST had a high correlation between *in situ* SST and satellite-based. Whereas for summer temperature, the correlation between *in situ* SST and satellite was nearly 0.

Figure.1-8

Sample sites of previous studies using modern (circles) or both modern and fossil corals (stars). Blue,

green and red color showed sample sites based on both Sr/Ca and d18Ocoral, only d18Ocoral and only

Sr/Ca respectively.

Cross plot showed our sample site.

Coral sample sites were plotted based on table 1-1.

Latitude	Longitude	Location	Proxy	Fossil	References
23.50	**58.75**	**Gulf of Oman**	**$\delta^{18}O_c$, Sr/Ca**	◯	**This study**
		Arabian Sea	**$\delta^{18}O_c$, Sr/Ca**	◯	**This study**
-0.13	98.52	Mentawai	$\delta^{18}O_c$, Sr/Ca	◯	Abram et al., 2006
-4.62	55	Seychelles	$\delta^{18}O_c$, Sr/Ca	◯	Chales et al., 1997
29.43	34.97	Gulf of Aqaba	$\delta^{18}O_c$, Sr/Ca	◯	Felis et al., 2002
10.53	72.67	Western India	$\delta^{18}O_c$, Sr/Ca	×	Sagar et al.,2016
-12.09	96.88	Cocos	$\delta^{18}O_c$, Sr/Ca	×	Hemmekam et al., 2018
-12.65	45.1	Mayotte	$\delta^{18}O_c$, Sr/Ca	×	Zinke et al., 2009
27.85	34.31	Southern Gulf of Aqaba	$\delta^{18}O_c$, Sr/Ca	×	Felis et al., 2018
-23.15	43.58	Western Madagascar	$\delta^{18}O_c$	×	Zinke et al., 2008
-28.46	113.77	Western GBR	$\delta^{18}O_c$	×	Kuhnert, H. et al.1999
-8.02	39.5	Tanzania	$\delta^{18}O_c$	×	Damassa et al., 2006
-3.2	40.1	Kenya	$\delta^{18}O_c$	×	Nakamura et al.,2009
-21	55	La Reunion	$\delta^{18}O_c$	×	Pfeiffer et al., 2004
17.21	54.84	Arabian Sea	$\delta^{18}O_c$	×	Tudhope et al., 1996
-5.33	71.92	Chagos	$\delta^{18}O_c$	×	Pfeiffer et al., 2004
-21.91	113.97	Western GBR	Sr/Ca	×	Clarke et al, 2017

Table1

List of coral archives related to SST in the Indian Ocean.

2. Methodology for paleo-climate reconstructions using modern and fossil corals

Abstract

On this chapter, method was described for climate reconstruction using modern and fossil corals. On this thesis, high temporal resolution records should be provided from both modern and fossil corals. Coral specimens were collected from two sample sites (the Gulf of Oman and Mashirah island). For paleoclimate reconstructions, Sr/Ca and $\delta^{18}O_{coral}$ analysis were conducted using ICP-OES and isotope ratios mass spectrometry, respectively. $\delta^{18}O_{sw}$ were calculated from combinations of Sr/Ca and $\delta^{18}O_{coral}$ following Ren et al., 2002. SEM observations and XRD were conducted to check diagenetic alternations in fossil corals. Age of fossil corals were determined using 14C or U-Th techniques.

2-1 Coral sampling

On February 23, 2013, a *Porites* sp. coral colony were drilled in the Gulf of Oman (23°30′ N, 58°45′ E: Figs 1-4 and 1-5 and 1-6). This *Porites* colony was living at a 2 m water depth in a small bay (Bandar Khayran) south of Muscat. In total, the coral core was 71 cm long [Fig.2-1]. In the same survey, High-energy deposited corals were collected from the Fins [Gosta et al., 2013, Fig.2-2]. Fins were in the northeastern coast of the Arabian Peninsula (Fins: 22°54' N, 59°13' E) and developed the Holocene terrace. The distance between sample sites between the modern and the fossil corals is within 90km.

On March 25, 2015, *Porites sp.* Coral colonies were collected from the Mashirah island, the southern coast of Arabian Penisula [Fig.2-3]. High energy deposited coral from the Mashirah island were also collected in this survey [Fig.2-4].

Coral colonies were sliced into 5-mm-thick slabs. For modern coral core from the Gulf of Oman, we took X-radiographs of the coral slabs and manually developed X-ray photo. Slabs of coral colonies from the Mashira island and fossil corals were taken X-ray image using Digital X-ray scanner. From X-ray photos/images, density band and the coral growth axis were confirmed.

2-2 Screening diagenesis

We conducted X-ray diffraction to check secondary-calcite contents on coral skeletons and observed microstructure in coral skeleton using Scanning Electron Microscope installed at Institute for the Advancement of Higher Education, Hokkaido university.

2-3 Age determinations

The ages of fossil coral specimens from Fins were determined with radiocarbon isotope (^{14}C) technique. We corrected the local oceanic reservoir effect following to the method described in Cullen et al. [2000]. Cullen et al. were reported the corrected ^{14}C ages of archeological sites in the Mesopotamia region using the same method with us. We can compare the fossil coral records with histories of archeological sites in the Mesopotamian region.

The ages of fossil coral from Mashira island were determined using high precision U-Th dating technique (Fig.2-5). U-Th age determinations were conducted at High-Precision Mass Spectrometry and Environment Change Laboratory, Department of Gesciences, National Taiwan University [Shen et al., 2012]. U-Th chemistry was carried out in clean room on a class 100 bench in a class-10,000 clean -room.

Chemistry of U-Th age determinations were conducted as following steps (Fig.2-6). Coral carbonates were weighed, 0.1 (for modern and young fossil corals) and 0.3 g (for fossil corals) coral carbonates were used for

U-Th age determinations. Weighed coral skeletons were dissolved with HNO_3 in Teflon beaker. Dissolved carbonates were added iron, $HClO_4$ and artificial isotopes of U and Th for standard. The Teflon beaker with Teflon-cap was heated until 180ºC on a hot plate during one day for reflux. After one day reflux, Teflon-cap was opened, and Teflon beaker heated until 260ºC to make a yellow or orange precipitation (for removing HNO_3). Yellow precipitation was dissolved with HCl and transferred to a centrifuge-tube. NH4OH was added in the centrifuge tube to make Fe-colloid. In this step, U and Th co-precipitated with Fe-colloid. The centrifuge tube was centrifuged in three times while adding with milli-Q water after each centrifuge. Co-precipitations of Fe, U and Th colloid were dissolved using HNO_3. Dissolved co-precipitations were dried on a 260ºC hot-plate. Sample precipitations were concentrated and purified by repeat adding $14HNO_3$ and drying on a 260ºC hot plate. Sample precipitations were dissolved with 7N HNO_3.

Column for separating U and Th were cleaned with milli-Q. Cation-resin was filled in column using pipet. For getting cation free resin, HNO_3 were loaded on the column and Column preparation was done.

Sample precipitations were loaded on column. HNO_3 were loaded on the column to take away Fe^{2+} from resin. 6N HCl were loaded on the column to collect Th into 30mL Teflon beaker. H2O were loaded on the column to collect U into 7mL Teflon beaker. Both 30mL and 7mL Teflon beaker were heated until 260ºC on the hot plate to make a precipitation. Sample precipitations were concentrated and purified by repeat adding $14HNO_3$ and drying on a 260ºC hot plate in 3 times. Both U and Th sample precipitation were dissolved using 1% HNO_3 with HF. U and Th sample solutions were transferred to vials.

U and Th isotopic compositions in coral skeletons were measured on a Thermo Fisher NEPTUNE multi collector inductively coupled plasma mass spectrometer (MC-ICP-MS). The sample solutions were measured in the order of "instrumental blank (1% HNO_3 with HF)", Th solutions, U solutions.

2-4 Subsamples for geochemical analysis

We prepared ledges of 1.5-2 mm in thickness along the maximum growth axis and obtained coral powder at 0.2-0.5 mm interval for geochemical analysis (Fig. 2-7). Sampling interval and ledge thickness were degermed to get biweekly resolution records and enough powder for Sr/Ca ratios and oxygen isotopes.

2-5 Analytical procedures for stable $\delta^{13}C_{coral}$ and $\delta^{18}O_{coral}$

Oxygen and carbon isotope measurements for modern corals

The coral powder was weighed, and 100 μg (±20 μg) were taken for oxygen and carbon stable isotope analysis. The sample powder was reacted with 100% H_3PO_4 at 70 °C in an automated carbonate preparation device

(Kiel II). The $\delta^{13}C_{coral}$ and $\delta^{18}O_{coral}$ were analyzed with a Finnigan MAT251 stable isotope ratio mass spectrometer system installed at Hokkaido University. Analytical errors for $\delta^{13}C_{coral}$ and $\delta^{18}O_{coral}$ were determined to be 0.03 and 0.06‰, respectively, based on replicate measurements of the NBS-19 standard (Fig. 2-8, 1σ, n=5).

After measurement of the Arabian modern coral, we used on reference gas on the MAT251 (2016, July 26th) and replaced to new one on 2016, September 2nd. The isotopic values of new reference gas were reported following values: $\delta^{13}C_{coral}$: -10.41 ‰$_{VPDB}$ and $\delta^{18}O_{coral}$: -9.84 ‰$_{VPDB}$. Test sequences using new reference gas was listed on table 2-1. Analytical results of CO2 isotopes were: 12.017±0.021 for $^{45}CO_2/^{44}CO_2$ and 6.339±0.024 for $^{46}CO_2/^{44}CO_2$ (Fig. 2-8, table 2-1). Calculated results of $\delta^{13}C_{coral}$ and $\delta^{18}O_{coral}$ were 1.951±0.02 ‰$_{VPDB}$ and -2.213±0.02 ‰$_{VPDB}$ (Fig. 2-8). After this measurement, we used new reference gas for MAT251 measurement.

Oxygen and carbon isotope measurements for fossil corals

The coral powder was weighed, and 30 μg (±10 μg) were taken for oxygen and carbon stable isotope analysis. The sample powder was reacted with 100% H_3PO_4 at 70 °C in an automated carbonate preparation device (Kiel IV). The $\delta^{13}C_{coral}$ and $\delta^{18}O_{coral}$ were analyzed with a Finnigan MAT253 stable isotope ratio mass spectrometer system installed at environmental science department, Hokkaido University. Analytical results of isotopic measurement in 2 years were -2.20 ± 0.05 ‰$_{VPDB}$ for $\delta^{18}O$ and 1.95 ± 0.03 ‰$_{VPDB}$ for $\delta^{13}C$ based on NBS19(Fig. 2-9, from 2015 April 24 to 2017 April 29, n = 229). Analytical results of isotopic measurement in one month were -2.20 ± 0.03 ‰$_{VPDB}$ for $\delta^{18}O$ and 1.95 ± 0.01 ‰$_{VPDB}$ for $\delta^{13}C$ based on NBS19(Fig. 2-10, 2016 December, n = 14). These average values corresponded with certified values from IAEA ($\delta^{18}O$: -2.20 ‰$_{VPDB}$, $\delta^{13}C$: 1.95 ‰$_{VPDB}$).

2-6 Analytical procedures for Sr/Ca

Calibration

We developed new Sr/Ca measurement methods (see Appendix). Our new method was to directly determine Sr/Ca form coral-dissolved solutions (modified method from Villers, 2002). We gravimetrically prepared 6 solution with different Me/Ca ratio values (Sr/Ca values are 0.0, 6.0, 8.0, 8.4, 8.8, 9.2, 9.8 mmol/mol). Mg^{2+} and Ba^{2+} were also added in standard solutions for matrix matching with solutions dissolved coral skeletons (Mg/Ca: 0.0 - 6.0 mmol/mol, Ba/Ca: 0.0 – 10.0 umol/mol). These solutions were prepared from each element standard solution (WAKO Pure Chemical Industrials, Ltd) and MilliQ, and stored in 250mL PP bottles. Ca concentrations were constant in *ca*. 7 ppm, and Me (Sr, Mg and Ba) concentrations were variable depending on Me/Ca values. The calibration line (as follows) was established for converting from Intensity ratio$_{Me/Ca}$ (Intensity of Me per Intensity of Ca) to Me/Ca ratio based on the analytical results of standard solutions (Fig. 2-11, de Villers, 2002).

$$Me/Ca \ ratio \ = A \times \frac{Intensity\ _{Me}}{Intensity\ _{Ca}} + B$$

Coral samples were weighed 80-100ug into 10mL PP centrifuge tubes and dissolved with *c.a.* 0.5 ml 25%HNO$_3$ acid. Dissolved coral samples were diluted in 7 ppm Ca concentration and *ca.* 3%HNO$_3$ with Milli-Q. Sample solutions were analyzed using same analytical line with standard solutions.

ICP-OES status

Instrumental status of ICP-OES was listed on table2-2. We used so called normal-nebulizer provided from Thermo Fisher Scientific (sample uptake: 0.4 mL/min, particle: 75 um). Sample (drain) tubes for inducing solutions to nebulizer should be replaced before extended. Nebulizer, chamber and torch loaded on ICP-OES were cleaned with HNO$_3$ and Aqua-Regia in every season. If we replace micro-mist nebulizer (lower sample uptake and smaller particle), it has a possibility to get high sensitivity for trace element in coral carbonate. Intensity ratio were measured smaller range for wavelength with higher peaks (eg. Ca and Sr).

Analytical calculations of Sr/Ca

After every five sample measurements, one JCp-1 solutions (7ppm Ca concentration and 3% HNO$_3$) were measured for running standard to correct an effect of instrumental drift. JCp-1 were weighed and dissolved with 25%HNO$_3$ acid. Dissolved JCp-1 were diluted in 7 ppm Ca concentration and *ca.* 3%HNO$_3$ with Milli-Q. JCp-1 solutions were stored in 0.5-1L PP bottle. 5mL JCp-1 solutions were dispensed from the bottle to 10mL PP centrifuge tubes. Calibration line from Intensity ratio$_{Me/Ca}$ to Me/Ca ratio were adapted on the analytical results of Intensity ratio$_{Me/Ca}$ in each sample solutions. Instrumental drift in Me/Ca ratio was corrected using a best-fit curve estimated from running standard (Fig.2-12, Schrag, 1999). Using this method, analytical precisions were 0.07%RSD (Fig.2-12: 0.006 mmol/mol: 1σ, n = 40). Uncorrected JCp-1 results in CREES lab was compiled and shown on Fig.2-13. Average value of uncorrected JCp-1 for one years (38 sequences) was 8.841 ± 0.099 mmol/mol. Averaged value of compiled JCp1 was same with Interlaboratory calibration (Sr/Ca: 8.838±0.042 mmol/mol). Therefore, external precision of our Sr/Ca method was 0.01 %.

Reference

1. Cullen, H. M. *et al.* Climate change and the collapse of the Akkadian empire: Evidence from the deep sea. *Geology* **28,** 379 (2000).

2. de Villiers, S., Greaves, M. & Elderfield, H. An intensity ratio calibration method for the accurate determination of Mg/Ca and Sr/Ca of marine carbonates by ICP-AES. *Geochemistry, Geophys. Geosystems* **3,** 1 (2002).

3. Hathorne, E. C. et al. Interlaboratory study for coral Sr / Ca and other element / Ca ratio measurements. 14, **9** (2013).

4. Hoffmann, G., Reicherter, K., Wiatr, T., Grützner, C. & Rausch, T. Block and boulder accumulations along the coastline between Fins and Sur (Sultanate of Oman): Tsunamigenic remains? *Nat. Hazards* **65,** 851–873 (2013).

5. Schrag, D. P. Rapid analysis of high-precision Sr/Ca ratios in corals and other marine carbonates. *Paleoceanography* **14,** 97–102 (1999).

6. Shen, C. *et al.* High-precision and high-resolution carbonate 230Th dating by MC-ICP-MS with SEM protocols. *Geochim. Cosmochim. Acta* **99,** 71–86 (2012).

ID	Sample name	Weight (μg)	Leak	Check	$^{45}CO_2/^{44}CO_2$	$^{46}CO_2/^{44}CO_2$	$\delta^{18}O_{VPDB}$	$\delta^{13}C_{VPDB}$
25571	C1	114	41	822	12.504±0.015	6.116±0.053	-2.436	2.476
25572	NBS19	107	44	834	11.996±0.01	6.359±0.043	-2.193	1.927
25573	NBS19	97	45	780	12.018±0.023	6.312±0.039	-2.240	1.953
25574	NBS18	92	63	757	4.707±0.016	-14.803±0.069	-23.183	-5.020
25575	NBS18	84	60	739	4.7±0.024	-14.805±0.053	-23.185	-5.027
25576	NBS19	83	63	757	12.038±0.002	6.346±0.021	-2.207	1.973

Table 2-1

Results of test measurement using MAT253 with new reference gas.

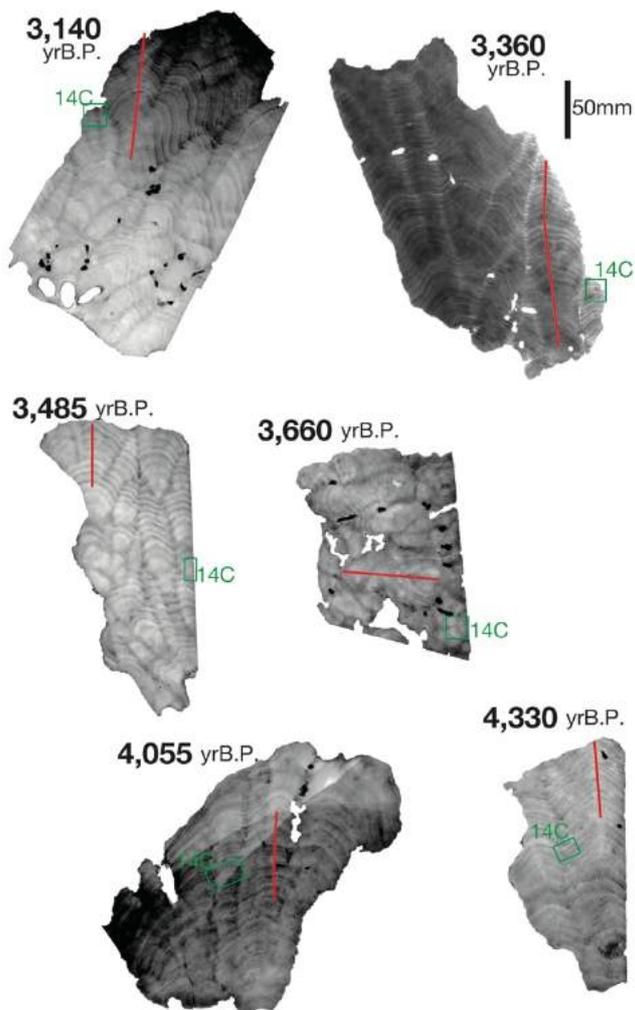| Parameter	
Power	1.15 kW
Auxiliary gas flow	0.5 L/min
Nebuliser flow	0.2 Mpa
Pump ratec	45 rpm
Integration time	5 sec.
Replicates	5 times
Rince time	1 min.

Table 2-2

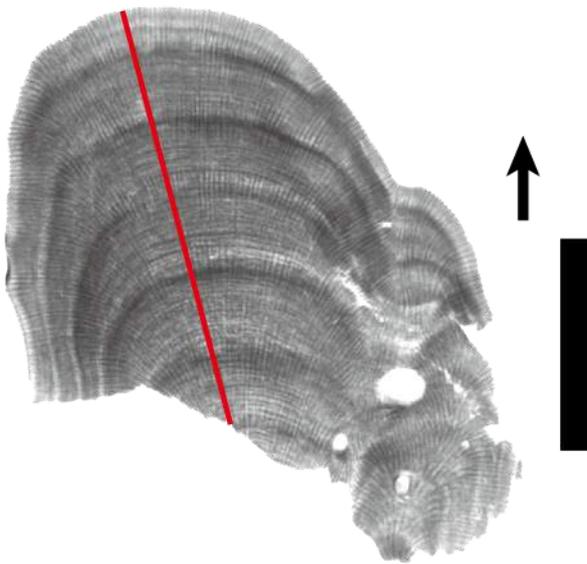Operating Condition of ICP-OES (iCAP6200).

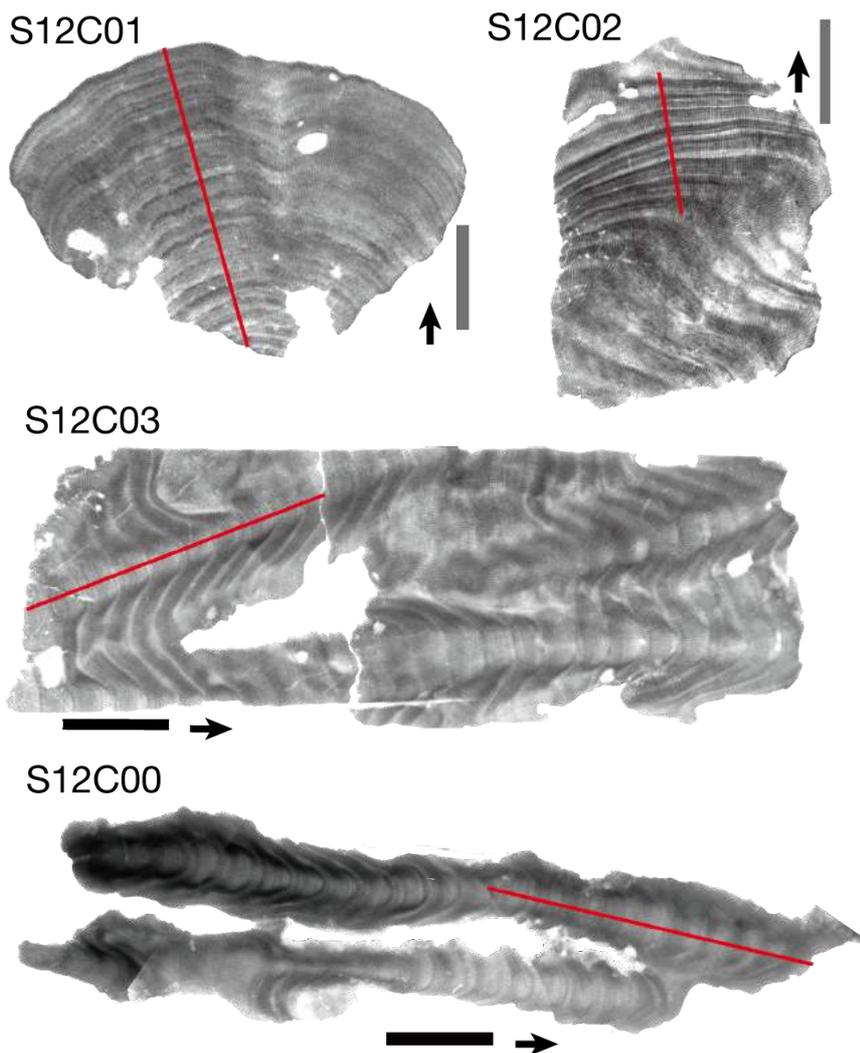**Figure 2-1**

X-ray photo of Omani coral core

Figure 2-2

X-ray photo of Omani fossil corals

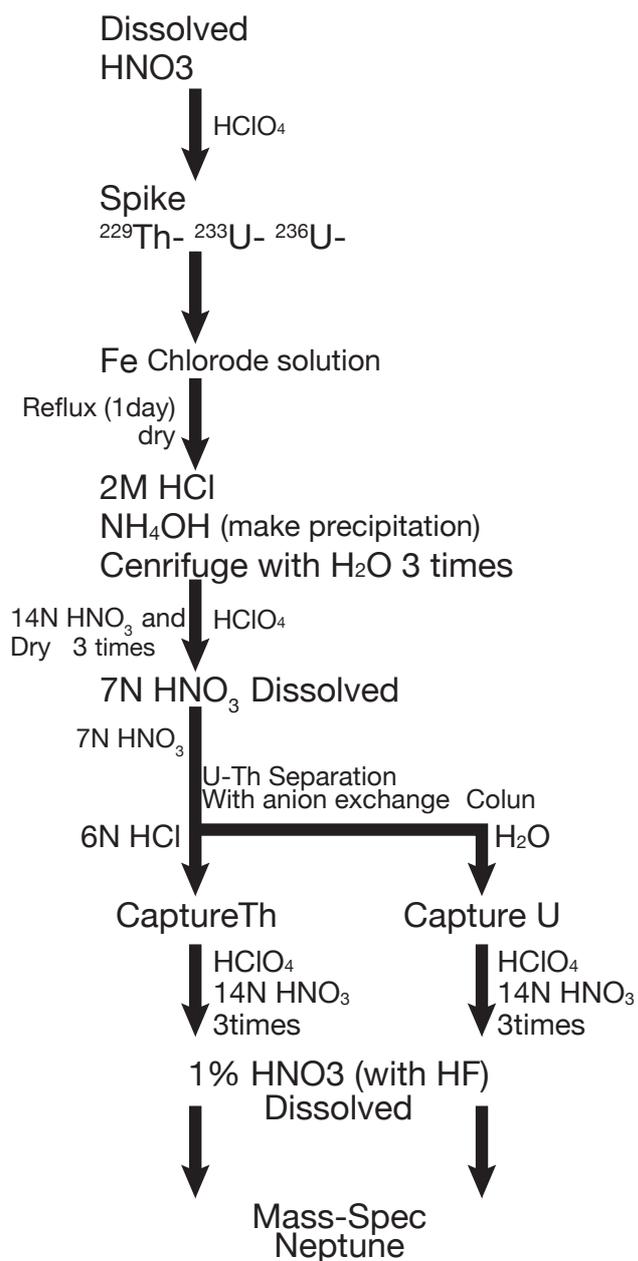**Figure 2-3**

X-ray photo of Arabian coral

Black bar shows 5cm scale, Arrow shows growth direction.

S12C01

S12C02

S12C03

S12C00

Figure 2-4

X-ray photo of Arabian fossil corals

Black bars show 5cm scale, Arrows show growth direction.

Dissolved
HNO3

$\downarrow$ HClO$_4$

Spike
^{229}Th- ^{233}U- ^{236}U-

$\downarrow$

Fe Chlorode solution

Reflux (1day)
dry $\downarrow$

2M HCl
NH$_4$OH (make precipitation)
Cenrifuge with H$_2$O 3 times

14N HNO$_3$ and HClO$_4$
Dry 3 times $\downarrow$

7N HNO$_3$ Dissolved

7N HNO$_3$

U-Th Separation
With anion exchange Colun

6N HCl   H$_2$O

CaptureTh   Capture U

HClO$_4$ HClO$_4$
14N HNO$_3$ 14N HNO$_3$
3times   3times

1% HNO3 (with HF)
Dissolved

Mass-Spec
Neptune

Fig.2-5
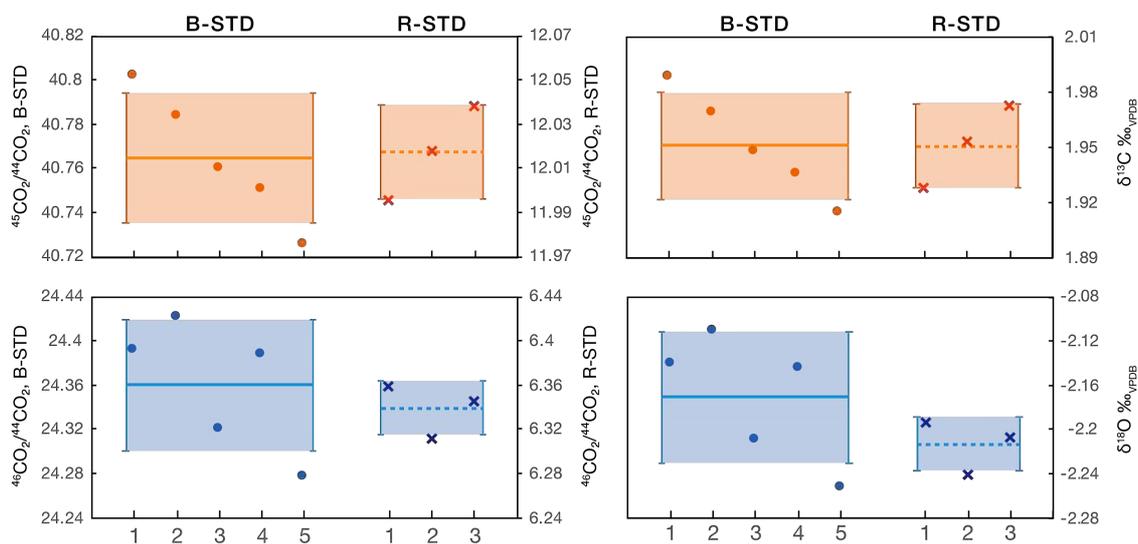
Flowchart for U-Th age determination

41
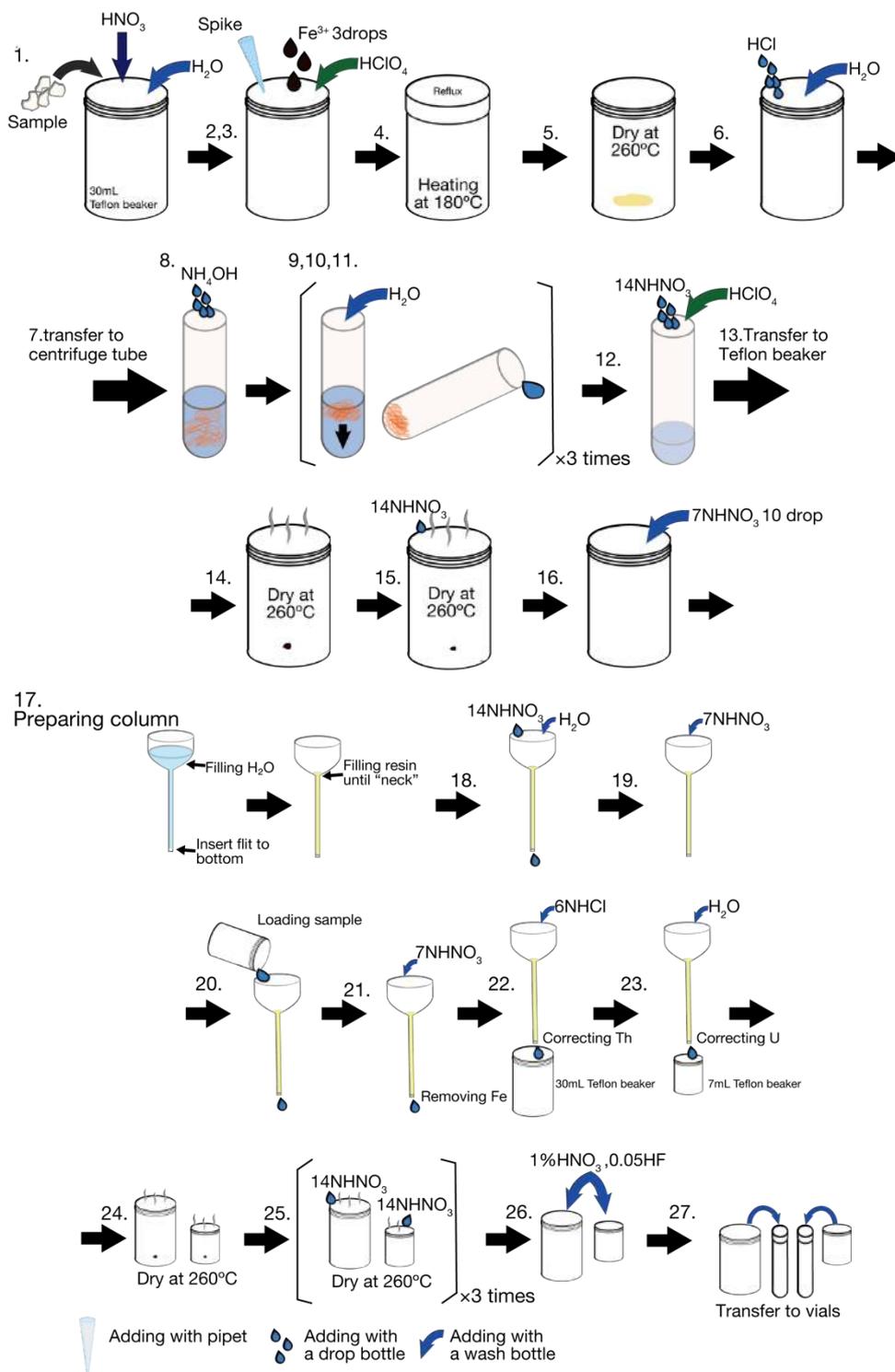
Fig.2-6
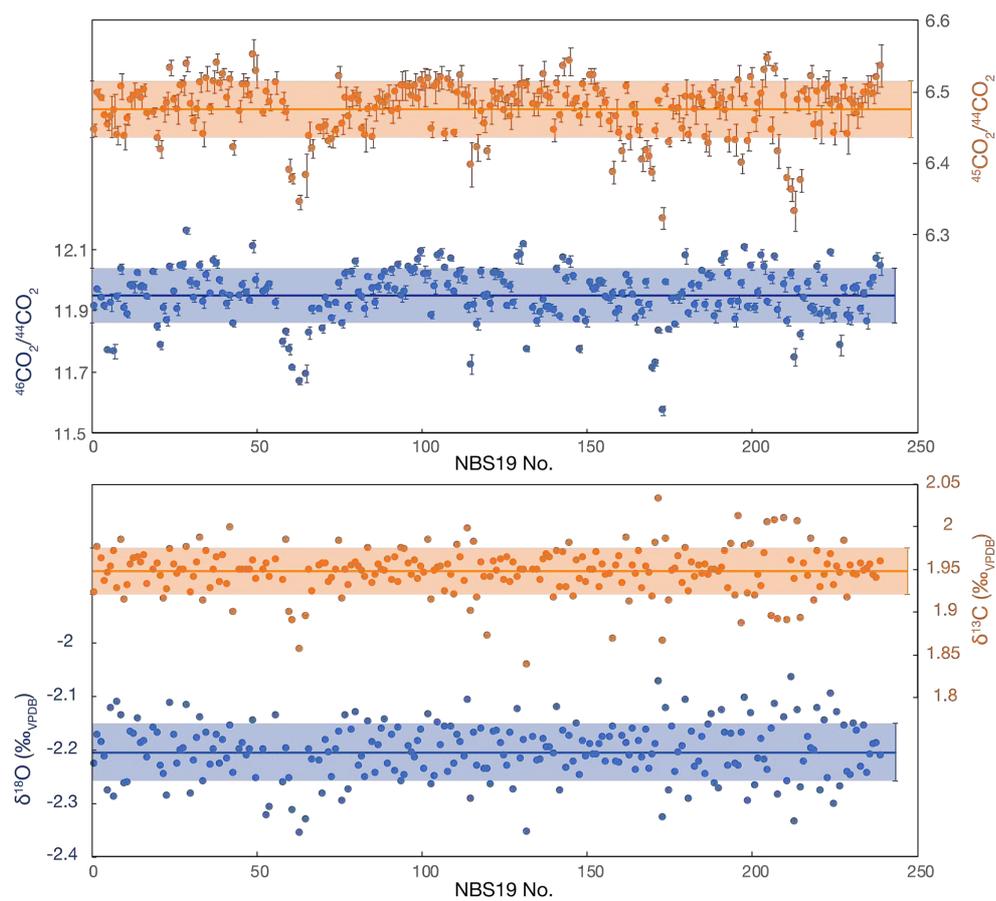
Methods for U-Th age determination
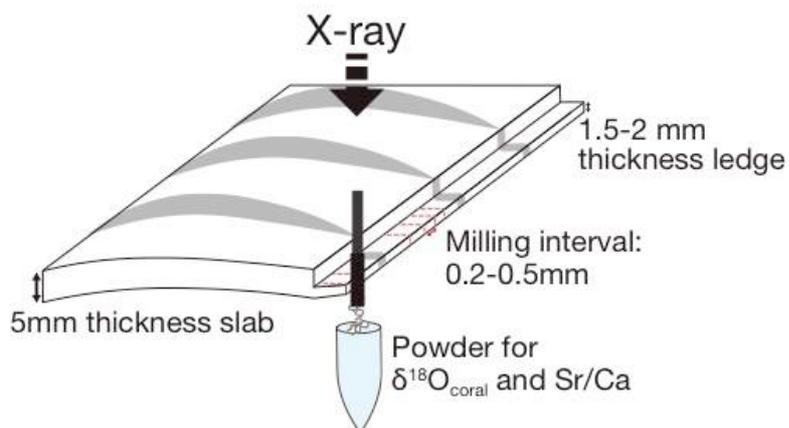
Figure 2-7

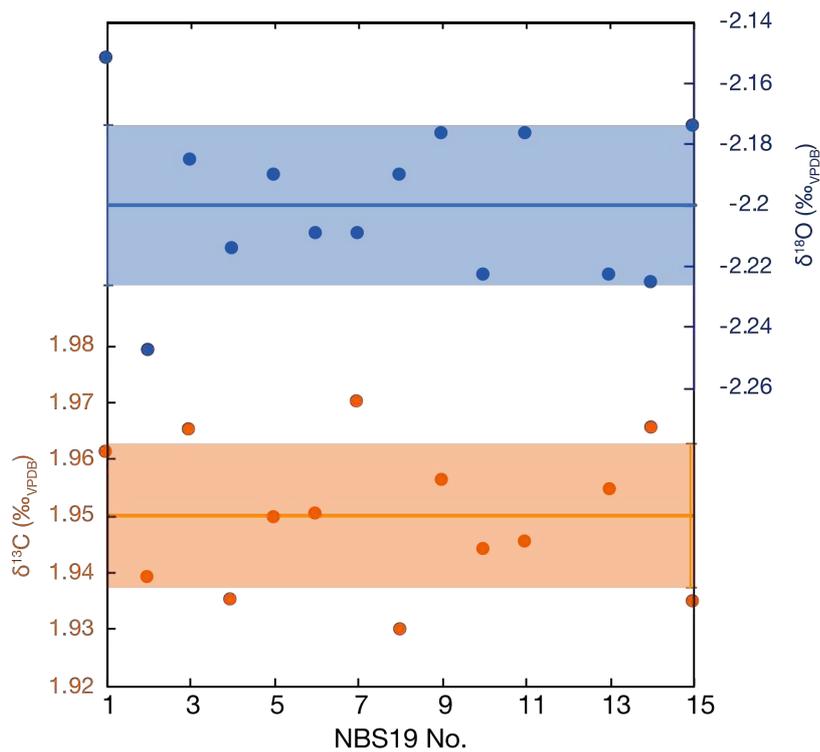Schematic figure of collecting powder-sample from coral-slabs

Figure 2-8

NBS19 results of test sequences. Left panels showed results before calculations. Right panels showed results of NBS19 using different reference gas.

Figure 2-9

NBS19 results from 2015 April 24 to 2017 April 29 using MAT 253.

Figure 2-10

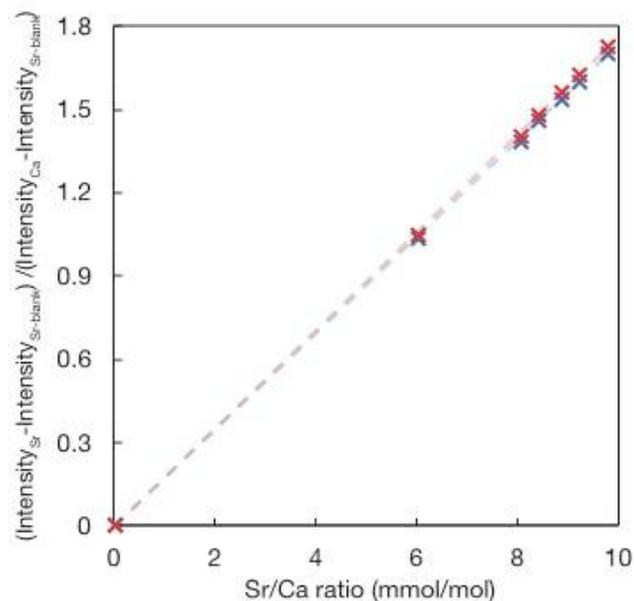NBS19 results in one month using MAT 253.

Fig.2-11

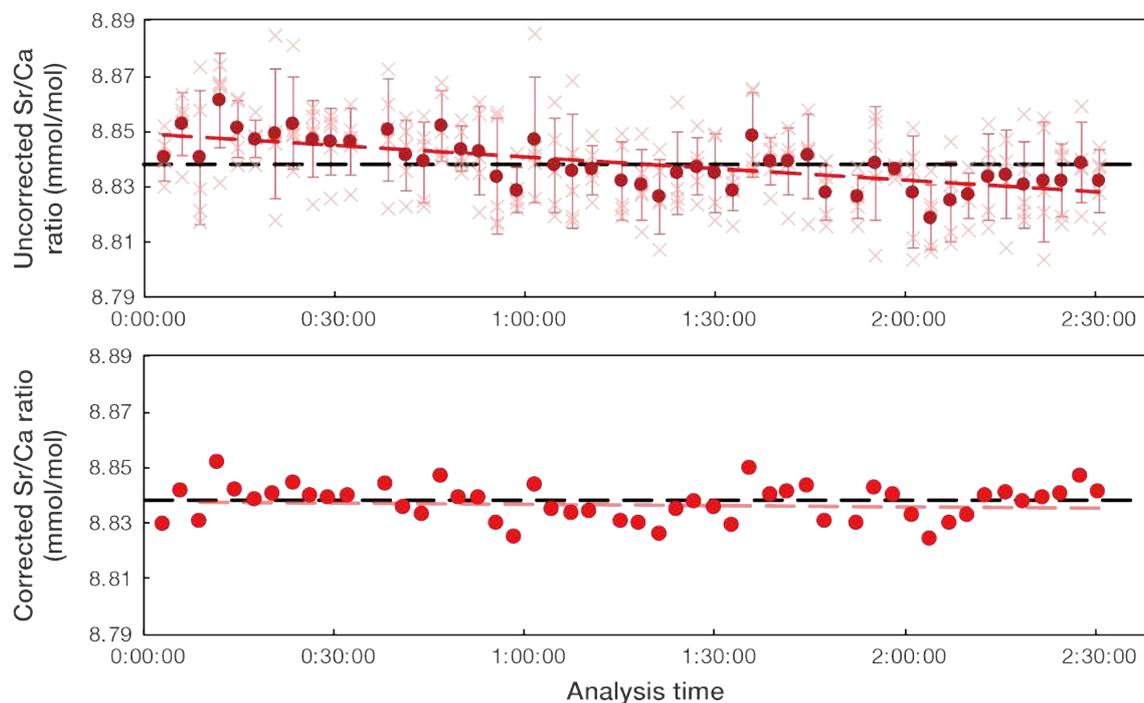Relationships of Sr/Ca in standard solutions and intensity ratio of Sr per that of Ca
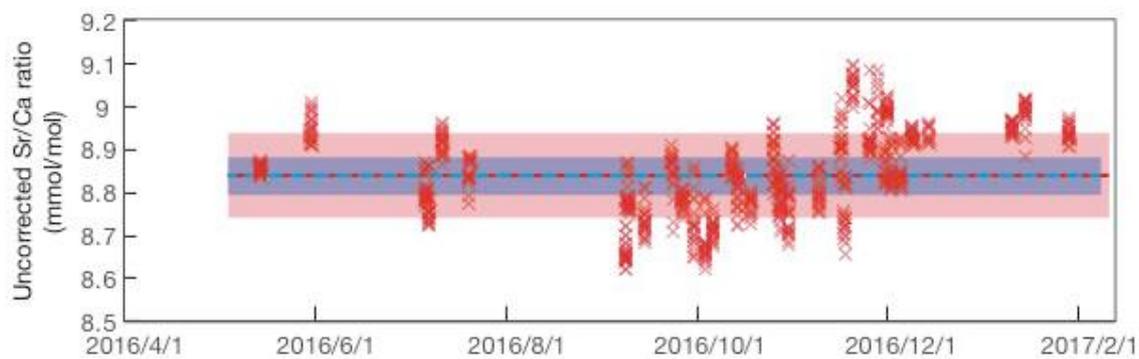

Fig.2-12

Replicate measurement ofJCp-1. Upper panel: uncorrected Sr/Ca ratio, lower panel: corrected JCp-1 using running standard of JCp-1.

Fig.2-13

Analytical results of running standard of Sr/Ca (JCp-1, uncorrected) from 2016 May to 2017 January.
Blue bar showed range of JCp-1 which Hathorne et al., 2012 reported. Red bar showed range of
uncorrected JCp-1 in CREES lab.

3. Western Indian Ocean upwelling uncouples from the Indian Ocean Dipole during the global-warming hiatus

Abstract

On this chapter, it was shown the influence of change in the global-warming trend on climate in the Indian Ocean. The Indian Ocean Dipole (IOD) is a dominant climate mode in the Indian Ocean and has intensified with 20th century global warming. However, air-temperature observations reveal a global warming hiatus since the late-1990s. We demonstrate the influence of this global-warming hiatus on large-scale IOD teleconnections via sea surface temperature (SST_{anom}) and seawater oxygen isotope ($\delta^{18}O_{sw-anom}$) reconstructions inferred from a *Porites* coral proxy record in the Gulf of Oman. The coral records in the Gulf of Oman were developed a 26-year long, biweekly record of Sr/Ca and $\delta^{18}O$. SST_{anom} is calculated from Sr/Ca ratios, and $\delta^{18}O_{sw-anom}$ is estimated by subtracting the temperature component from coral $\delta^{18}O$. Our records reveal that a regime shift in $\delta^{18}O_{sw-anom}$ towards lower mean values occurs in 1999. Before the regime shift, higher SST_{anom} and $\delta^{18}O_{sw-anom}$ values are observed in the summer of positive-IOD years. This changes after 1999. The regime shift is associated with an increase of upwelling in the western Indian Ocean/Arabian Sea, which is likely triggered by an intensified Walker circulation during the global-warming hiatus. This upwelling intensification dominates climate variability in the western Indian Ocean/Arabian Sea, while the impact of the IOD on upwelling reduces.

3-1 Introduction

Indian Ocean dipole

The Indian Ocean Dipole (IOD) is an aperiodic oscillation of SST in the equatorial Indian Ocean with socio-economic impacts in the circum-Indian Ocean region (*e.g.,* increasing flooding and malaria occurrence in Kenya; severe drought in Australia; coral reef death and wildfires in Indonesia: Hashizume et al., 2012, Ummenhofer et al., 2009, Abram 2003). The IOD is defined by the difference in sea surface temperature (SST) anomalies between the western Indian Ocean (Arabian Sea) and the eastern Indian Ocean (Sumatra, Indonesia) (Fig. 3-1: Saji et al., 1999). In neutral states of the IOD, SSTs in the western Indian Ocean are colder than in the east, due to intense monsoon-driven upwelling in the Arabian Sea during boreal summer. During the positive phase of the IOD, the zonal SST pattern in the Indian Ocean reverses, with cool SSTs and upwelling in the eastern Indian Ocean off Sumatra, and warm SST anomalies/reduced upwelling in the western Indian Ocean/Arabian Sea. During the negative phases of the IOD, the SST pattern is comparable to the neutral state but amplified.

Global-warming trend

An obvious global-warming trend is confirmed by observations of global surface air-temperatures over the 20th century, and there is still debate about whether the global-warming trend affects ocean-atmospheric interaction phenomena. Coral records from Indonesia, the Seychelles and Kenya suggest that the IOD intensified due to a weakened Indo-Pacific Walker circulation following the onset of global-warming during the 20th century [Abram et al., 2008, Nakamura et al., 2009]. This suggests that IOD variability may intensify during future global-warming [Abram et al., 2008].

Global-warming hiatus

However, previous studies report the period that the global surface air-temperatures has not risen between the late-1990s and 2015, so called a global-warming hiatus (Kosaka and Xie, 2013). Satellite-based SST data suggest that the Interdecadal Pacific Oscillation (IPO), which is the dominant mode of atmosphere-ocean interactions in the subtropical north Pacific, reversed from a positive to a negative phase at the same time with the onset of the global-warming hiatus. The anomalous cooling conditions in the eastern Pacific caused by the negative-IPO state are thought to have contributed to the global-warming hiatus [Kosaka and Xie, 2013, Power et al., 1999]. The regime shift of 1999 has been observed in satellite-based SST and precipitation data in various regions of the tropics [Lyon et al., 2014, Hong et al., 2014]. Satellite-based wind stress dataset suggests that the Indo-Pacific Walker circulation intensifies during the global-warming hiatus [England et al., 2014].

It is poorly understood how the global-warming hiatus influences on the large-scale ocean-atmospheric

teleconnections including the IOD. The Walker circulation of the Pacific and Indian Ocean are connected via an "atmospheric bridge" over Indonesia, which links climate changes in the Pacific and in the Indian Ocean [Han et al., 2014]. The strength of IOD fluctuations may also respond to changes in the Pacific Walker circulation, as the IOD primarily reflects a perturbation of the Indian Ocean Walker circulation. The coral records previously used to investigate past IOD behavior end in the late 20th century [Abram et al., 2008]. Hence, they do not encompass the recent global-warming hiatus between 1999 and 2015.

In order to investigate IOD variability before and after the global-warming hiatus, we use biweekly-resolution records (0.5mm sampling interval) of seawater oxygen isotope ($\delta^{18}O_{sw}$) and Strontium/Calcium ratio in coral skeletons (Sr/Ca) from a 26-year long coral core drilled in the Gulf of Oman, Arabian Sea [Fig. 1-4 to 6]. Previous coral studies have demonstrated that Sr/Ca reflects SST variations [Beck et al., 1992, Shen et al., 1992], while oxygen isotope in coral skeleton ($\delta^{18}O_{coral}$) is influenced both by SST and $\delta^{18}O_{SW}$. Therefore, $\delta^{18}O_{SW}$ can be estimated by subtracting the SST contribution inferred from the Sr/Ca ratio from $\delta^{18}O_{coral}$. $\delta^{18}O_{SW}$ is mainly influenced by the balance between evaporation and precipitation and by mixing of water masses with different $\delta^{18}O_{SW}$ compositions [Gagan et al., 1998]. A previous study of the Oman coral proxy records has demonstrated that they record summer upwelling driven by the Indian/Arabian monsoon in summer (IMS) [Watanabe et al., 2017, discussed in Chapter.4].

3-2 Statistical methods

To detect the regime shift, and to evaluate its timing and statistical significance, we adopted the sequential t-test approach on to the SST_{anom} and $\delta^{18}O_{sw\text{-}anom}$ record [Rodionov, 2004]. For time-series of SST_{anom} and $\delta^{18}O_{sw\text{-}anom}$, [$Xk$, k = 1, 2, …, n], the mean of the first regime (R1), X_{R1} is determined as

$$\overline{X}_{R1} = \sum_{k=1}^{l} X_k \quad (1 \leq k \leq l)$$

where l is the "cut-off length" of regimes to be determined the mean. The cut-off length controls the time-scale of the detected regime shift. The cut-off length determines the minimum length of the regime shift not altering the magnitude of the shift [Rodionov, 2004, Liu et al., 2013]. To identify the major change of regime in all time-series, we chose a long cut-off length (13 years). The difference from the mean of next regimes (R2) that would be statistically significant (Student's t-test) is given by

$$\text{diff} = t\sqrt{2\sigma_l^2/l}$$

where t is the value of the t-distribution with $2l - 2$ degrees of freedom at 1 % probability level. $2\sigma_l^2$ is the average variance for the intervals during the cut-off length. Every Xk ($k \geq l + 1$) is evaluated in a sequential order.

If Xk is within the range of ±diff (from X$_{R-1}$ - diff to X$_{R-1}$ + diff), the X$_{R-1}$ is recalculated with the Xk value and l-1 previous Xk values. If Xk is out of the range of ±diff, it is considered as a possible starting point ($k = j$) of the next regime (*R2*). The regime shift index (RSI) is determined to confirm the significance of the next regime stating point at year j,

$$RSI_{i,j} = \sum_{i=j}^{j+m} \frac{x_i - (X_{R1} + diff)}{l\sigma_l}$$

$$(m = 0, 1 \dots, l\text{-}1)$$

If the RSI has the same signal at year j with evaluation using "diff", it increases the confidence of the shift occurrence. The evaluation for the next regime shift was conducted from the following data of the current regime until all the time-series were evaluated.

3-3 Results and discussions

SST-Sr/Ca and δ^{18}O$_{coral}$ thermometry in the Gulf of Oman

The average of Sr/Ca was 9.28 (mmol/mol). The maxima and minima of Sr/Ca values were 9.56 and 8.98 (mmol/mol). The δ^{18}O$_{coral}$ averaged -4.33 (‰$_{VPDB}$) and ranged from -4.92 to 3.41 (‰$_{VPDB}$) (Fig.3-2).

The regression line of AVHRR-SST and Sr/Ca was established using seasonal maxima and minima, as follows (Fig.3-3):

$$\text{Sr/Ca (mmol/mol)} = -0.044 \pm 0.003 \text{ SST (°C)} + 10.46 \pm 0.18$$

$$(r = 0.95: P < 0.01)$$

The regression line of AVHRR-SST and δ^{18}O$_{coral}$ was established using seasonal maxima and minima assuming δ^{18}O$_{coral}$ reflect only SST, as follows (Fig.3-3):

$$\delta^{18}O_{coral} \text{ (‰}_{VPDB}) = -0.104 \pm 0.005 \text{ SST (°C)} - 1.28 \pm 0.14$$

$$(r = -0.92 \ P < 0.01)$$

Satellite-based SST in the Gulf of Oman did not reflect low SST excursions in summer measured by CTDs [Watanabe et al., 2017, Fig. 1-7]. In order to evaluate effect of uncertainty in satellite-based SST, we established SST dependency of Sr/Ca and δ^{18}O$_{coral}$ using seasonal minima (maxima) (Table 3-1, Fig.3-3). The slope of SST-Sr/Ca (δ^{18}O$_{coral}$) regression using both winter and summer peaks was similar with the slope using winter peaks, while SST-Sr/Ca (δ^{18}O$_{coral}$) regression using summer peaks could not established (non-significant). Our SST-Sr/Ca regression using both winter and summer peaks would be suitable for estimation of SST-variations, because our slope value of Sr/Ca-SST regression was consistent within the range of the previous published values

(from -0.08 to -0.04 mmol/mol) (Fig.3-3-a and Table3-2). Our slope value of $\delta^{18}O_{coral}$ -SST regression was higher than the previously reported values (Fig.3-3-b and Table3-3). Only Timor coral $\delta^{18}O$ showed similar slope values, and this record was shown to record seasonal-scale $\delta^{18}O_{SW}$/salinity variations. At Timor, maximum SST coincided with maximum salinity, so the seasonal cycle of coral $\delta^{18}O$ with respect to temperatures was dampened. The coral $\delta^{18}O$-temperature relationship of the Omani coral suggested that $\delta^{18}O_{SW}$ affects $\delta^{18}O_{coral}$ in either winter or summer, in the sense that colder (warmer) SSTs coincided with depleted (enriched) $\delta^{18}O_{SW}$.

The coral $\delta^{18}O_{sw}$ record indicates a significant regime shift in 1999

Step-changes are confirmed in both Sr/Ca and $\delta^{18}O_{SW}$ anomalies ($\delta^{18}O_{SW-anom}$) in the late-1990s (Fig.3-2). To show the significances of these step-changes in coral records, we calculate SST anomalies (SST_{anom}) from Sr/Ca and $\delta^{18}O_{SW-anom}$ by subtracting the Sr/Ca-temperatures from $\delta^{18}O_{coral}$ (see supplemental information). Both time series of SST_{anom} and $\delta^{18}O_{SW-anom}$ show a shift towards lower values after the late-1990s (Fig. 3-2). SST_{anom} ($\delta^{18}O_{SW-anom}$) inferred from our coral show a gradual cooling (decrease) over the past 26-years (-0.03±0.01°C/year and -0.02±0.00‰$_{VSMOW}$/year). The sequential t-test approach is adopted to determine the timing and the statistical significances of these shifts (see methods section). The 26-year SST_{anom} record shows a significant peak (0.202; P < 0.01) indicating a regime shift in October 1996 (Fig. 3-4). The mean SST_{anom} in the two time periods before and after 1996 are 0.73±2.59 °C and -0.46±2.71 °C, respectively (Fig. 3-4). The range of SST_{anom} before and after the regime shift is 10.96 and 11.72 °C, respectively. The 26-year $\delta^{18}O_{SW-anom}$ record indicates a major regime shift in July 1999 (peak: 0.583; P < 0.01; Fig. 3-4). The mean $\delta^{18}O_{sw-anom}$ values before and after 1999 are 0.17±0.33 ‰$_{VSMOW}$ and -0.16±0.34‰$_{VSMOW}$, respectively (Fig. 3-4). The range of $\delta^{18}O_{sw-anom}$ before and after the regime shift is 1.41 and 1.81‰$_{VSMOW}$, respectively. The regime shift detected in the $\delta^{18}O_{sw-anom}$ record in 1999 is more pronounced than that in 1996 in the SST_{anom} record (compare Fig. 3-4).

The regime shift in the coral proxy data: timing

The regime shift detected in the $\delta^{18}O_{sw-anom}$ record (1999) occurs three years later than the regime shift in the SST_{anom} record (1996), and the regime shift in the $\delta^{18}O_{sw-anom}$ (1999) record is much more pronounced, compared to the SST_{anom} record (1996). So what is the correct timing of the regime shift? Which record is more reliable? $\delta^{18}O_{sw}$ varies depending on the hydrological balance and is closely related to salinity. The regime shift in 1999 observed in $\delta^{18}O_{sw-anom}$ could be caused by the following two mechanisms: (1) an increase in precipitation relative to evaporation in the region where the coral was sampled and (2) an intensification of upwelling in the western Indian Ocean/Arabian Sea.

To evaluate the influence of precipitation on the $\delta^{18}O$ of sea surface waters [McCulloch et al., 1994], we

compare the Omani coral record with *in situ* precipitation rates around the Arabian Sea. The precipitation rates in eastern Oman (Seeb airport: 23.60° N, 58.30° E; GHCN-Month ver. 2: https://www.ncdc.noaa.gov/ghcnm/v2.php, Fig. 3-2) are compared with $\delta^{18}O_{sw\text{-}anom}$. We find that the precipitation rate in the Oman decreases after the regime shift in 1999 (average precipitation before the regime shift: 8.5±19.7 mm/month, after the regime shift: 4.7±13.6 mm/month). The observed reduction in precipitation rates would cause more enriched $\delta^{18}O_{sw}$ values. However, the coral $\delta^{18}O_{sw\text{-}anom}$ record shows a depletion, $\delta^{18}O_{sw\text{-}anom}$ shifts towards lower mean values. This means, the observed regime shift in $\delta^{18}O_{sw\text{-}anom}$ after 1999 is not related to regional precipitation (Oman is an arid area and precipitation is very low).

Alternatively, intensified upwelling in the western equatorial Indian Ocean/Arabian Sea may be responsible for the regime shift towards lower mean $\delta^{18}O_{sw\text{-}anom}$ values observed in 1999. Upwelling brings colder water masses with a more enriched-$^{16}O_{sw}$ composition to the sea surface [Schmidt, 1999, Pfeiffer et al., 2004, Sengupta et al., 2013]. In the Arabian Sea, $\delta^{18}O_{sw}$ decreases with depth (Fig. 3-5: Schmidt, 1999). The IMS causes strong coastal upwelling along the coast of Somalia and the southern Arabian Peninsula in boreal summer [Schott and McCreary, 2001]. The upwelled water flows northward, and gyres and eddy systems sweep into the Oman Sea [Al-Azri et al., 2013]. While upwelling influences both $\delta^{18}O_{sw}$ and SST, the latter adjusts more quickly to the overlying atmosphere. Hence, the upwelling-related cooling would not be as distinct in the SST_{anom} record as the depletion in the $\delta^{18}O_{sw\text{-}anom}$ record. This makes it also more difficult to accurately determine the timing of the regime shift in the SST_{anom} data. The regime shift detected in $\delta^{18}O_{sw\text{-}anom}$, in the year 1999, is therefore considered accurate.

The regime shift in 1999: a consequence of the global-warming hiatus?

The timing of the regime shift in 1999 inferred from the coral proxy records towards colder and lower mean values coincides with the onset of the global-warming hiatus, which lasts from 1999 to 2015. Concurrent shifts in several areas in the late-1990s have been reported in satellite-based SST and precipitation datasets (*e.g.,* cooling in the eastern equatorial Pacific; drought in east Africa) [Kosaka and Xie, 2013, Lyon et al., 2014]. The year 1999 also marks a phase reversal of the IPO, which changed from a positive to a negative polarity.

The intensification of upwelling in the Arabian/Oman Sea after the regime shift in 1999 inferred from our $\delta^{18}O_{sw\text{-}anom}$ record may reflect an intensification of the Walker circulation in the tropical Indo-Pacific [Wyrtki, 1973]. During the global-warming hiatus from 1999-2015 [Fig. 3-4], the Walker circulation intensifies, caused by low SSTs in the eastern Pacific, a spatial pattern typical of the negative IPO-phase [England et al., 2014]. In contrast, the Walker circulation appears to have weakened during 20th century warming [Vecchi et al., 2006], although this issue is still subject of debate[12]. An intensified Walker circulation as seen during the global-warming hiatus should also strengthen

upwelling in the Arabian Sea, as the Walker circulation in the Indian and Pacific Ocean is connected by the "atmospheric bridge" over Indonesia. In summary, our results suggest that an intensified Walker circulation, which is thought to be the main cause of the global-warming hiatus, also causes intensified upwelling in the western Indian Ocean/Arabian Sea. This leads to cooling and more depleted $\delta^{18}O_{sw}$ at our coral site.

The Indian Ocean Dipole signatures in the coral proxy data before and after 1999

The IOD signatures would be altered by an intensified Walker circulation during the global-warming hiatus from 1999. To evaluate whether the regime shift in 1999 is related to IOD variability, we subdivide the time series of SST_{anom} and $\delta^{18}O_{sw-anom}$ into neutral, positive-IOD and post-IOD years based on the Dipole mode Index (Fig. 3-4)[4]. Positive-IOD years are defined as years when the Dipole mode index exceeds plus one standard deviation. We compare the seasonal cycles of SST_{anom} ($\delta^{18}O_{sw-anom}$) during neutral, positive-IOD and post-IOD years, because the IOD tends to cause biannual variations of SST and winds stress in the Indian Ocean [Li et al., 2003]. The time series of SST_{anom} and $\delta^{18}O_{sw-anom}$ are split in two sub-periods (before and after the regime shift in 1999, respectively). The mean seasonal cycles of SST_{anom} and $\delta^{18}O_{sw-anom}$ are estimated from the biweekly mean values for each of the 3 classes (neutral, positive-IOD and post-IOD) during each sub-period (Fig. 3-6). We apply a t-test to detect statistically significant differences between the monthly mean values of SST_{anom} and $\delta^{18}O_{sw-anom}$ in each of the three classes (neutral year vs. positive-IOD year and neutral year vs. post IOD-year). The Dipole mode index shows 10 positive-IOD events in the 26-year records of SST_{anom} and $\delta^{18}O_{sw-anom}$ (Fig. 3-4). Positive-IOD events occur four times prior to the regime shift in 1999, and six times afterwards. Prior to the regime shift in 1999, the mean summer values (June to July) of SST_{anom} and $\delta^{18}O_{sw-anom}$ are significantly higher during both the positive-IOD year and the post-IOD year than during the neutral year (t-value < 0.05: Fig. 3-6). The difference in the mean summer SST_{anom} ($\delta^{18}O_{sw-anom}$) between neutral and positive-IOD years is 2.79±1.55 °C (0.46±0.32‰$_{VSMOW}$) (Fig. 3-6). The mean summer values between neutral and post-IOD years differ by 3.07±2.07 °C (SST_{anom}) and 0.54±0.37 ‰$_{VSMOW}$ ($\delta^{18}O_{sw-anom}$), respectively (Fig. 3-6). After the regime shift in 1999, the mean seasonal cycles and the mean summer values of SST_{anom} and $\delta^{18}O_{sw-anom}$ during positive- and post-IOD years are not significantly different from neutral years (t-value > 0.05 Fig. 3-6).

The Indian Ocean Dipole signatures in instrumental sea surface temperature data before and after 1999

To confirm the relationships between an occurrence of the regime shift in 1999 and SST variations in the IOD regions, the Dipole mode index is statistically analyzed with the same method as we conducted on the Omani coral records. Prior to the regime shift in 1999, the Dipole mode index shows significant positive departures during positive-IOD years compared to neutral years (t-value < 0.05: Fig. 3-7), but not during post-IOD years. After 1999,

positive departures of the Dipole mode index continue from positive-IOD to post-IOD years (Fig. 3-7). SST anomalies in the eastern IOD region (Sumatra, Indonesia) drop during positive-IOD years (due to upwelling of cold water) and increase during post-IOD years relative to neutral years (Fig. 4b). The difference between summer SST anomalies of neutral and positive IOD years is 0.57°C (t-value < 0.05) prior to 1999. After the regime shift, this difference reduces to 0.25ºC (Fig. 3-7). In the western IOD region (Arabian Sea) SST anomalies increase during the summer of positive-IOD years and stay warmer than normal until the fall of post-IOD years (Fig. 3-7). However, after the regime shift in 1999, the summer SST anomaly differences between neutral and positive-IOD years are much smaller (0.21ºC compared to 0.33°C prior to 1999). The duration of warm SST anomalies shortens (Fig. 3-7).

Influences of the global-warming hiatus on the IOD signatures

Our Omani coral records show differences of the IOD signatures between before and after the regime shift. The western Indian Ocean/Arabian Sea is considered sensitive to the IOD, which normally causes a warming of surface waters. This is clearly seen in the proxy data prior to 1999, i.e. prior to the onset of the global-warming hiatus: summer SST_{anom} and $\delta^{18}O_{sw-anom}$ of positive-IOD years are significantly higher than during neutral years. During the global-warming hiatus, however, positive-IOD years and neutral years do not show significantly different signatures in the SST_{anom} ($\delta^{18}O_{sw-anom}$) record. These results suggest that the IOD weakens during the global-warming hiatus and/or that its impact on upwelling in the western Indian Ocean/Arabian Sea weakens. Therefore, positive-IOD events are hardly detectable in SST_{anom} and $\delta^{18}O_{sw-anom}$ after 1999.

The interpretation of instrumental data supports differences of the IOD signatures in our coral proxy data between before and after the regime shift. The Dipole mode index [Saji et al., 1999] and SST anomalies in the eastern and western IOD regions[4] are investigated and also show weak responses (particularly in the Western Indian Ocean) after the regime shift in 1999 (Fig. 3-7). After 1999, the Dipole mode index indicates weaker but longer-lasting positive IOD events (Fig. 4a and d). Positive SST anomalies continue well into post-IOD years (Fig. 3-7). The western Indian Ocean/Arabian Sea only shows weak IOD anomalies. We suggest, based on our proxy data, that intensified upwelling in the western Indian Ocean levels out the IOD-driven warming during positive-IOD years, which then appear much more similar to neutral years (Figs. 3-7 and 3-9). In the eastern Indian Ocean, anomalous cooling (t-value < 0.05) during positive-IOD years due to upwelling is also weaker after the regime shift in 1999 (Figs. 3-7 and 3-9).

Propagation mechanisms of IOD footprints under the global-warming trend/hiatus

The IMS propagates footprints of the IOD to the western equatorial Indian Ocean and the Arabian Sea (where it is recorded by our coral proxy data) [Izumo et al., 2008]. The primary driver of upwelling in the Arabian

Sea is the IMS. A strong IMS intensifies upwelling, enhances cooling (recorded by a decrease in SST_{anom}) and upwelling of seawater less depleted in $\delta^{18}O$ during boreal summer (recorded by a decrease in $\delta^{18}O_{sw-anom}$) [Tudhope et al., 1996]. Note that the latter should be a better indicator of upwelling-related changes, as $\delta^{18}O_{sw}$ does not adjust as quickly to the overlying atmosphere as SST. To further investigate the relationship between the coral data and the IMS, we compare the SST_{anom} ($\delta^{18}O_{sw-anom}$) record with the monthly maximum precipitation rate in northwestern India (Fig. 3-8: precipitation rate data provided from the India Meteorological Department). The Arabian Sea provides the moisture source for IMS summer precipitation in northwestern India. Strong upwelling in the Arabian Sea suppresses evaporation [Izumo et al., 2008]. 3-year moving averages of June to August SST_{anom} and $\delta^{18}O_{sw-anom}$ (Fig. 3-8) show a positive correlation with the 3-year moving averages of maximum precipitation rate in northwestern India (SST_{anom} vs. precipitation rate in the northwestern India: $r = 0.53$, $P < 0.01$, $\delta^{18}O_{sw-anom}$ vs. precipitation rate in the northwestern India: $r = 0.71$, $P < 0.01$). This confirms that the IMS affects the upwelling intensity in the Arabian Sea during boreal summer.

Under the global-warming trend, the intensity of IMS would be changed by SST variations in the western Indian Ocean in response to phase-changes of the IOD. Before the regime shift, significant differences observed between neutral and positive-IOD years in the summer values of SST_{anom} ($\delta^{18}O_{sw-anom}$) are consistent with previous work, which suggests that the IOD becomes stronger during 20th century warming [Abram et al., 2008, Nakamura et al., 2011]. High SST_{anom} and $\delta^{18}O_{sw-anom}$ anomalies in the summer of the positive-IOD years would be a result of weak upwelling in the Arabian Sea in response to a weak IMS (Fig. 3-4). The strength and intensity of the IMS are controlled by the temperature gradient between the Eurasian continent and the Indian Ocean [Bamzai and Shukla, 1999, Goes et al., 2005]. Positive IOD events increase SSTs in the western equatorial Indian Ocean [Fig. 3-9] and thereby reduce the temperature gradient between the Eurasia and the Indian Ocean. This weakens the IMS during positive-IOD years.

Whereas, under the global-warming hiatus, the intensified IMS would not change in response to the IOD because the western Indian Ocean uncouples from the IOD. After the regime shift, no differences are observed in the boreal summer SST_{anom} ($\delta^{18}O_{sw-anom}$) during neutral and positive-IOD years (Fig.3-6), suggesting that the impact of the IOD in the western Indian Ocean/Arabian Sea weakens significantly during the global-warming hiatus. This suggests that the large-scale ocean-atmosphere teleconnections of the IOD are much weaker during that time. This could be caused by the enhanced Walker circulation [England et al., 2014]. Similar SST_{anom} and $\delta^{18}O_{sw-anom}$ values during the boreal summer of positive-IOD years and neutral years suggest that upwelling in the Arabian Sea induced via the IMS has the same strength during positive-IOD and neutral years (Fig. 3-9). Reduced warming in the western

Indian Ocean/Arabian Sea during positive-IOD years following the regime shift in 1999 is probably contributing to the strong IMS observed in this period. The intensified upwelling reduces SST in the western Indian Ocean/Arabian Sea, and this in turn increases the temperature gradient between the Eurasian continent and the western Indian Ocean during the global-warming hiatus (Fig. 3-9). This further strengthens the IMS, which in turn causes even stronger upwelling in the Arabian Sea in a positive feedback loop.

3-4. Conclusions

In summary, we find evidence for a regime shift in the Gulf of Oman in 1999, which is coincident with a phase change of the IPO and the onset of the global-warming hiatus. The western Indian Ocean/Arabian Sea uncouples from the IOD after the regime shift. We believe this is caused by an intensified Walker circulation and a stronger IMS during the period of the so-called global-warming hiatus. Upwelling is a mechanism to increase the heat exchange from the ocean to the atmosphere [Chen and Tung, 2014]. An inactive IOD might also contribute to a slowdown of global-warming during the hiatus period. Upwelling in the western Indian Ocean/Arabian Sea appears to be modulated by decadal IOD fluctuations and should be a subject of further studies to better understand the mechanisms of global-warming.

References

1. Hashizume, M., Chaves, L. F. & Minakawa, N. Indian Ocean Dipole drives malaria resurgence in East African highlands. *Scientific Reports* **2,** 1–6 (2012).

2. Ummenhofer, C. C. *et al.* What causes southeast Australia's worst droughts? *Geophysical Research Letters* **36,** 1–5 (2009).

3. Abram, N. J., Gagan, M. K., McCulloch, M. T., Chappell, J. & Hantoro, W. S. Coral reef death during the 1997 Indian Ocean Dipole linked to Indonesian wildfires. *Science (New York, N.Y.)* **301,** 952–955 (2003).

4. Saji, N. H., Goswami, B. N., Vinayachandran, P. N. & Yamagata, T. A dipole mode in the tropical Indian Ocean. *Nature* **401,** 360–363 (1999).

5. Abram, N. J., Gagan, M. K., Cole, J. E., Hantoro, W. S. & Mudelsee, M. Recent intensification of tropical climate variability in the Indian Ocean. *Nature Geoscience* **1,** 849–853 (2008).

6. Nakamura, N. *et al.* Mode shift in the Indian Ocean climate under global warming stress. *Geophysical Research Letters* **36,** 3–7 (2009).

7. Kosaka, Y. & Xie, S. Recent global-warming hiatus tied to equatorial Pacific surface cooling. *Nature* **501,** 403–407 (2013).

8.   Power, S., Casey, T., Folland, C., Colman, A. & Mehta, V. Inter-decadal modulation of the impact of ENSO on Australia. *Climate Dynamics* **15,** 319–324 (1999).

9.   Lyon, B., Barnston, A. G. & DeWitt, D. G. Tropical pacific forcing of a 1998-1999 climate shift: Observational analysis and climate model results for the boreal spring season. *Climate Dynamics* **43,** 893–909 (2014).

10.   Hong, C. C., Wu, Y. K., Li, T. & Chang, C. C. The climate regime shift over the Pacific during 1996/1997. *Climate Dynamics* **43,** 435–446 (2014).

11.   England, M. H. *et al.* Recent intensification of wind-driven circulation in the Pacific and the ongoing warming hiatus. *Nature Clim. Change* **4,** 222–227 (2014).

12.   Han, W. *et al.* Indian ocean decadal variability: A review. *Bulletin of the American Meteorological Society* **95,** 1679–1703 (2014).

13.   Beck, J. W. *et al.* Sea-surface temperature from coral skeletal strontium/calcium ratios. *Science (New York, N.Y.)* **257,** 644–647 (1992).

14.   Shen, C.-C. *et al.* The calibration of D[Sr/Ca]versus sea surface temperature relationship for Porites corals. *Geochimica et Cosmochimica Acta* **60,** 3849–3858 (1996).

15.   Gagan, M. K. *et al.* Temperature and Surface-Ocean Water Balance of the Mid-Holocene Tropical Western Pacific. *Science* **279,** 1014–1018 (1998).

16.   Watanabe, T. K., Watanabe, T., Yamazaki, A., Pfeiffer, M. & Claereboudt, M. R. Past summer upwelling events in the Gulf of Oman derived from a coral geochemical record. 1–7 (2017). doi:10.1038/s41598-017-04865-5

17.   Rodionov, S. N. A sequential algorithm for testing climate regime shifts. *Geophysical Research Letters* **31,** 9 (2004).

18.   Liu, Y., Wu, G. & Zhao, X. Recent declines in China's largest freshwater lake: Trend or regime shift? *Environmental Research Letters* **8,** (2013).

19.   Cahyarini, S. Y., Pfeiffer, M., and Dullo, W. Improving SST reconstructions from coral Sr / Ca records : multiple corals from Tahiti (French Polynesia). 31–40 (2009). doi:10.1007/s00531-008-0323-2

20.   Li, T., Wang, B., Chang, C.-P. & Zhang, Y. A Theory for the Indian Ocean Dipole–Zonal Mode*. *Journal of the Atmospheric Sciences* **60,** 2119–2135 (2003).

21. McCulloch, M. T., Gagan, M. K., Mortimer, G. E., Chivas, A. R. & Isdale, P. A high-resolution Sr/Ca and δ18O coral record from the Great Barrier Reef , Australia , and the 1982-1983 El Niño. *Geochimica et Cosmochimica Acta* **58,** 2747–2754 (1994).

22. Schmidt, G. a. Forward Modeling of Carbonate Proxy Data from Planktonic Foraminifera using Oxygen Isotope Tracers in a Global Ocean Model. **14,** 482–497 (1999).

23. Pfeiffer, M., Timm, O., Dullo, W. C. & Podlech, S. Oceanic forcing of interannual and multidecadal climate variability in the southwestern Indian Ocean: Evidence from a 160 year coral isotopic record (La Réunion, 55ºE, 21ºS). *Paleoceanography* **19,** 1–14 (2004).

24. Sengupta, S., Parekh, A., Chakraborty, S., Ravi Kumar, K. & Bose, T. Vertical variation of oxygen isotope in bay of Bengal and its relationships with water masses. *Journal of Geophysical Research: Oceans* **118,** 6411–6424 (2013).

25. Schott, F. a. & McCreary, J. P. The monsoon circulation of the Indian Ocean. *Progress in Oceanography* **51,** 1–123 (2001).

26. Al-Azri, A. R., Piontkovski, S. a., Al-Hashmi, K. a., Goes, J. I. & do Gomes, H. R. Chlorophyll a as a measure of seasonal coupling between phytoplankton and the monsoon periods in the Gulf of Oman. *Aquatic Ecology* **44,** 449–461 (2010).

27. Wyrtki, K. An Equatorial Jet in the Indian Ocean. *Science* **181,** 262–264 (1973).

28. Vecchi, G. a *et al.* Weakening of tropical Pacific atmospheric circulation due to anthropogenic forcing. *Nature* **441,** 73–76 (2006).

29. Izumo, T. *et al.* The role of the Western Arabian Sea upwelling in Indian monsoon rainfall variability. *Journal of Climate* **21,** 5603–5623 (2008).

30. Tudhope, A. W., Lea, D. W., Shimmield, G. B., Chilcott, C. P. & Head, S. Monsoon Climate and Arabian Sea Coastal Upwelling Recorded in Massive Corals from Southern Oman. *PALAIOS* 347 (1996). doi:10.2307/3515245

31. Nakamura, N. *et al.* Footprints of IOD and ENSO in the Kenyan coral record. *Geophysical Research Letters* **38,** 3–7 (2011).

32. Bamzai, A. S. & Shukla, J. Relation between Eurasian Snow Cover , Snow Depth , and the Indian Summer Monsoon : An Observational Study. *Journal of Climate* **12,** 3117–3132 (1999).

33. Goes, J. I., Thoppil, P. G., Gomes, H. D. R. & Fasullo, J. T. Warming of the Eurasian landmass is making the Arabian Sea more productive. *Science (New York, N.Y.)* **308,** 545–547 (2005).

34. Chen, X. & Tung, K. Varying planetary heat sink led to global-warming slowdown and acceleration. **20,** 74–80 (2014).

Table 3-1

Data Set	SST regresion eqution	r
Sr/Ca ratio		
Seasonal maxmia/minima	**Sr/Ca = -0.043 x (SST) + 10.457**	-0.949 (P < 0.01)
Winter peaks	Sr/Ca = -0.041 x (SST) + 10.400	-0.296 (P = 0.14)
Summer peaks	Sr/Ca = -0.003 x (SST) + 9.173	-0.034 (n.s.)
$\delta^{18}O_{coral}$		
Seasonal maxmia/minima	**$\delta^{18}O_{coral}$ = -0.104 x (SST) -1.278**	-0.944 (P < 0.01)
Winter peaks	$\delta^{18}O_{coral}$ = -0.101 x (SST) -1.348	-0.347 (P = 0.08)
Summer peaks	$\delta^{18}O_{coral}$ = 0.043 x (SST) -5.946	0.185 (n.s.)

The SST dependency of the Sr/Ca and $\delta^{18}O_{coral}$ in coral skeletons using summer, winter peaks or both peaks. The Sr/Ca ($\delta^{18}O_{coral}$) - SST regression line applied for this study is showed with bold letter.

Table 3-2

Reference	Slope (mmol×mol^{-1}/°C)	Species	LocaLity
This study	-0.044	*Porites.sp*	The Gulf of Oman
Gagan et al. (1998)[8]	-0.064	*Porites lutea*	Great Barrier Reef
Marshall and MuCulloch (2001)[9]	-0.059	*Porites.sp*	Xmas Island
Zinke et al. (2004)[10]	-0.05	*Porites lobata*	Myotte
Felis et al. (2004)[11]	-0.06	*Porites.sp*	Red Sea
Cahyarini et al. (2009)[5]	-0.04	*Porites.sp*	Timor
Sagar et al. (2016)[12]	-0.073	*Porites lutea*	Arabian Sea

Temperature dependency of the Sr/Ca ratio in coral skeletons.

Table 3-3

Reference	Slope (‰/°C)	Species	LocaLity
This study	-0.10	*Porites.sp*	The Gulf of Oman
Quinn et al. (1996)[13]	-0.19	*Porites lutea*	New Caledonia
Felis et al. (2000)[14]	-0.16	*Porites.sp*	Red Sea
Pfeiffer et al. (2004)[15]	-0.21	*Porites.sp*	La Reunion
Zinke et al. (2004)[10]	-0.19	*Porites lobata*	Myotte
Cahyarini et al. (2009)[5]	-0.10	*Porites.sp*	Timor

Temperature dependency of $\delta^{18}O$ in coral skeletons.
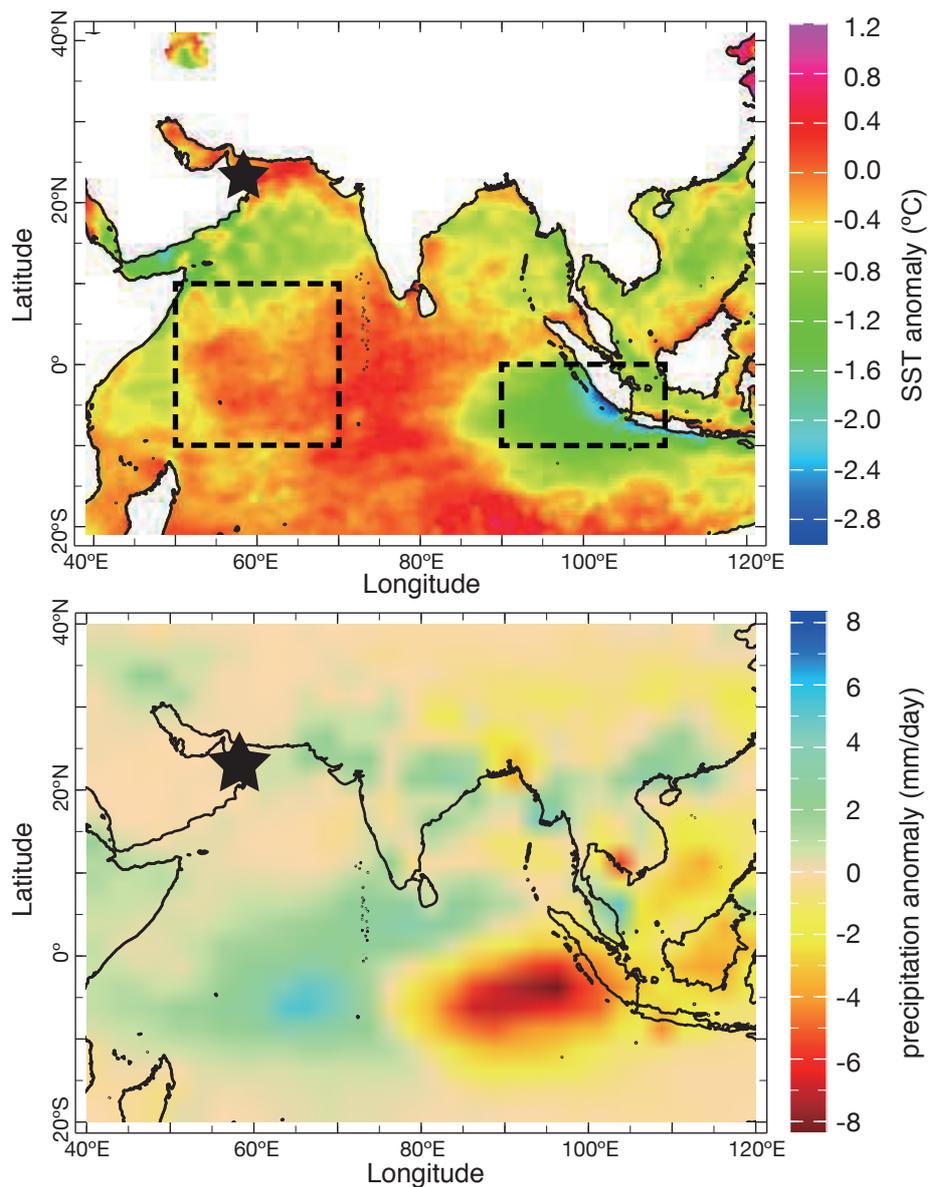
Fig.3-1

Contour maps showed SST and rainfall anomalies in July-November of the IOD event (1994). Boxes mark the eastern and western regions used for calculation the Dipole mode index. Our coral sampling site (star) were shown. SST and precipitation anomalies data were obtained from AVHRR (Advanced Very High Resolution Radiometer) and CAMS_OPI (Climate Anomaly Monitoring System and OLR Precipitation Index), respectively. Contour maps were provided from IRI data library (http://iridl.ldeo.columbia.edu).
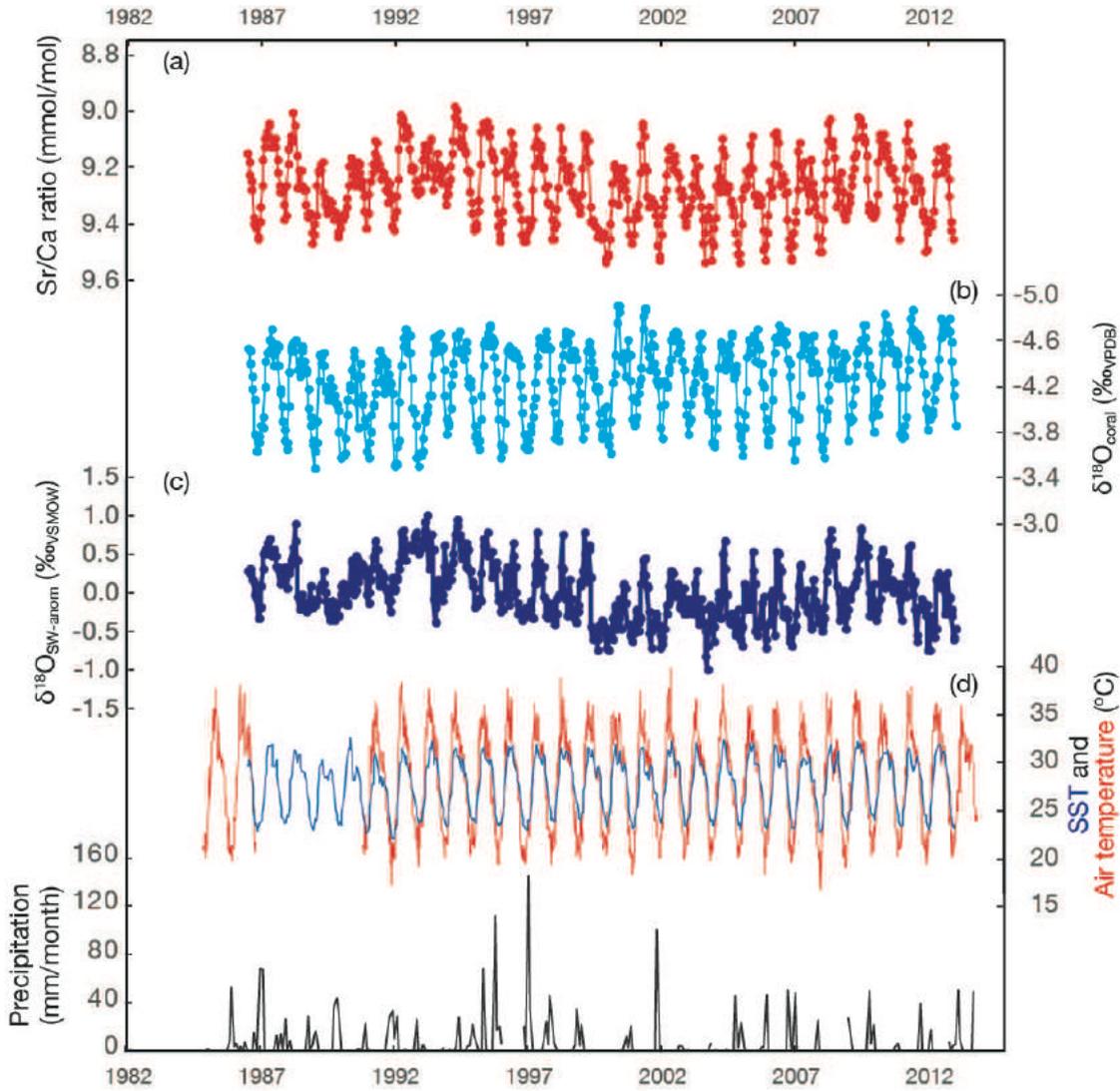
Fig.3-2

Biweekly records of the Sr/Ca ratios (a), $\delta^{18}O_{coral}$ (b) and $\delta^{18}O_{SW\text{-}anom}$ (c), AVHRR-SST in the Gulf of Oman (blue line)[1] and observational air-temperature at Seeb airport (red line: dataset from World Meteological Organization station: https://www7.ncdc.noaa.gov/CDO/cdo) (d) and observational precipitation at Seeb airport (GHCN-Monthly ver. 2[18]).
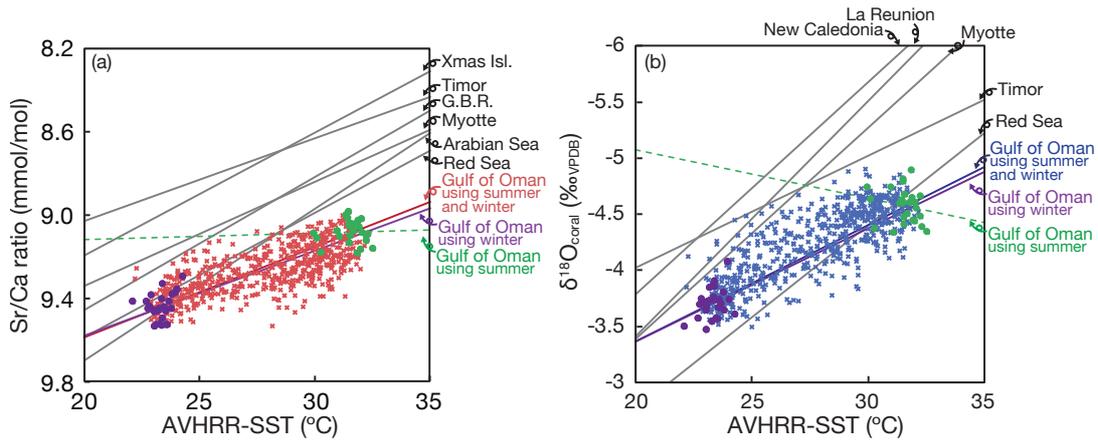
Fig.3-3

Calibration of the Sr/Ca ratio and δ¹⁸O$_{coral}$ thermometer (a and b). Circle-dots indicate the seasonal maxima and minima of the Sr/Ca (δ¹⁸O$_{coral}$), which are tied with the maxima and minima of SST, respectively (purple dots: minima of SST; green dots: maxima of SST). Cross-dots show the data points between all data points of Sr/Ca ratio (δ¹⁸O$_{coral}$).

(a) The red line shows our Sr/Ca-SST calibration line using both summer and winter peaks record in the *Porites* coral from the Gulf of Oman. The purple line (green dotted line) indicates our Sr/Ca-SST calibration line using summer (winter) peaks recorded in the Porites coral from the Gulf of Oman. The gray lines indicate the previous published Sr/Ca-SST calibration lines (TableS1).

(b) The blue line shows our δ¹⁸O$_{coral}$-SST calibration line using both summer and winter peaks recorded in the *Porites* coral from the Gulf of Oman. The purple line (green dotted line) indicates our δ¹⁸O$_{coral}$-SST calibration line using summer (winter) peaks recorded in the Porites coral from the Gulf of Oman. The gray lines indicate the previous published δ¹⁸O$_{coral}$-SST calibration line (TableS2). The slope of δ¹⁸O$_{coral}$-SST calibration line using both summer and winter peaks in our Omani coral is similar to the Timor δ¹⁸O$_{coral}$-SST slope.
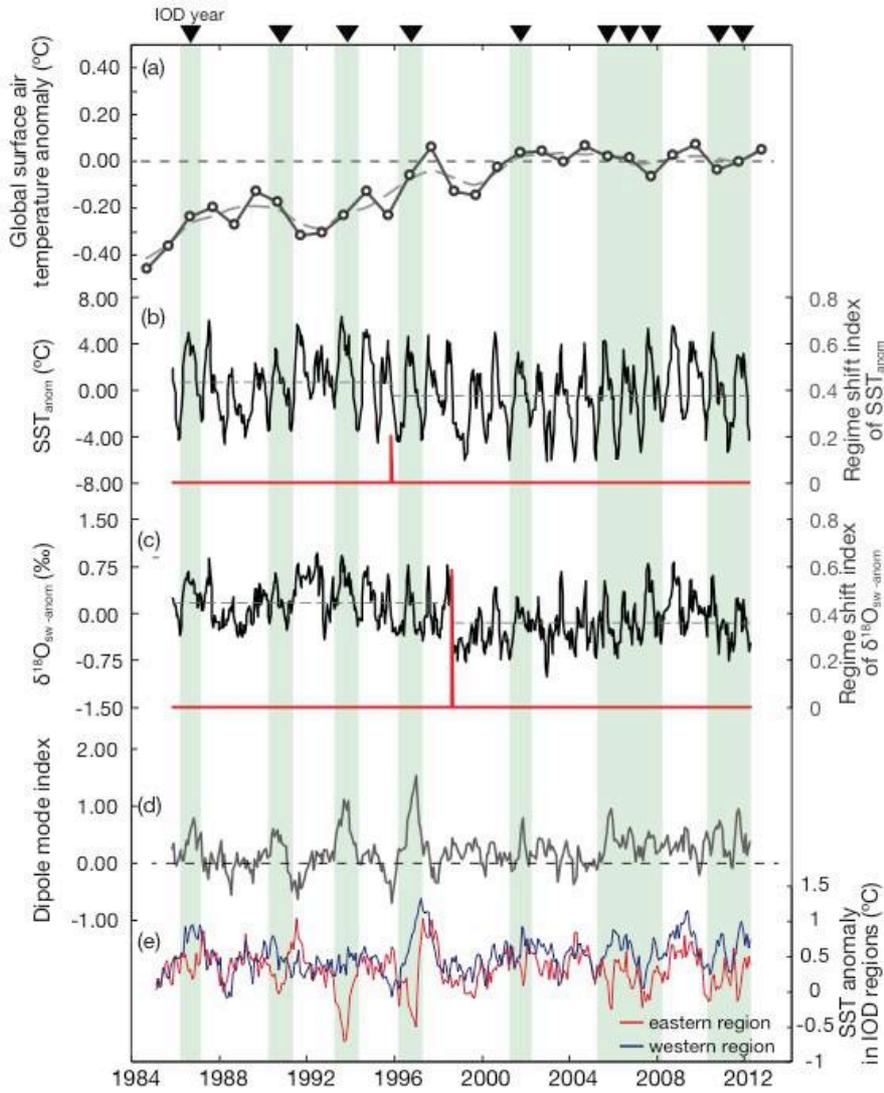
Fig.3-4

(a) Global surface air-temperature anomaly (relative to the period of 1998-2013), the. grey line is a 3-years moving average. Data are from the GISS surface temperature analysis (GISTEMP[41]). Thin dotted line: average global surface air-temperature anomaly during 1998-2013. (b) and (c) show the biweekly SST_{anom} and $\delta^{18}O_{sw\text{-}anom}$ in the Gulf of Oman (Black line). The dotted lines show the average values during the pre- and post the regime shift. The error bars indicate the uncertainties of biweekly SST_{anom} and $\delta^{18}O_{sw\text{-}anom}$. The regime shift index (red line) for both series was generated from Sequential t-test [37]. (d) Dipole mode index. The green patches and triangles show the timing of the IOD years[1]. (e) SST anomalies in western and eastern regions of IOD.
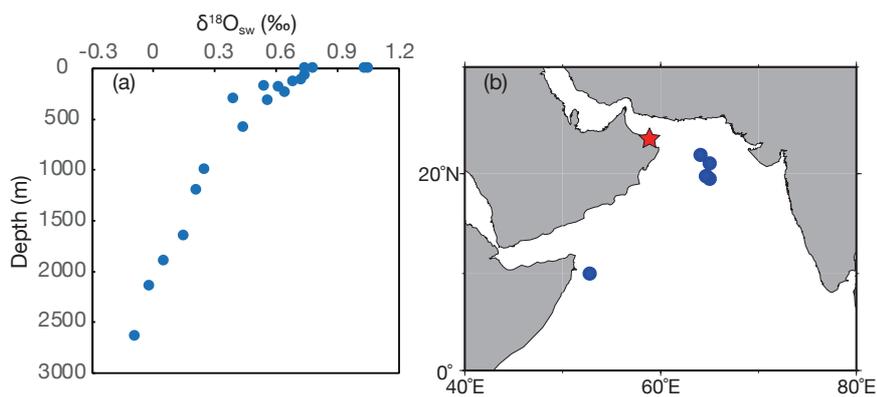
Fig.3-5

Depth profile of $\delta^{18}O_{sw}$ data from the Arabian Sea (a). Data from Schmidt *et al*., 1999[16] (https://data.giss.nasa.gov/cgi-bin/o18data/geto18.cgi). The circle dots on the map indicate water sampling sites (b). The star dot shows our coral sample site. The maps were generated using Generic Mapping Tools (GMT ver. 4.5.12)
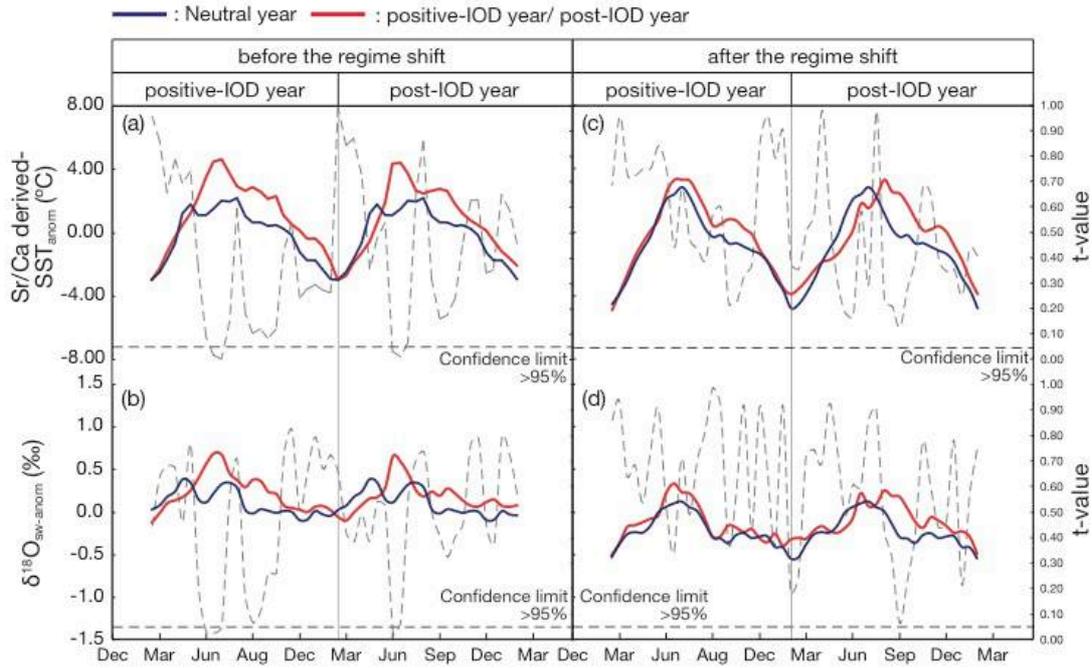
Fig.3-6

Seasonal SST anomalies (a) and $\delta^{18}O_{sw}$ anomalies (b) during neutral years (blue line) and IOD years or post-IOD years (red line) before the regime shift. Dotted line: t-test results (neutral years vs. IOD years and neutral years vs. the post-IOD years, respectively). During boreal summer of positive and post IOD years, SST anomalies and $\delta^{18}O_{sw}$ anomalies are higher than in neutral years.

Seasonal SST anomalies (c) and $\delta^{18}O_{sw}$ anomalies (d) during neutral years (blue line) and IOD years or post-IOD years (red line) after the regime shift. Dotted line: t-test results (neutral years vs. IOD years and neutral years vs. the post-IOD years, respectively). SST anomalies and $\delta^{18}O_{sw}$ anomalies during neutral, positive-IOD and post IOD years are not significantly different.
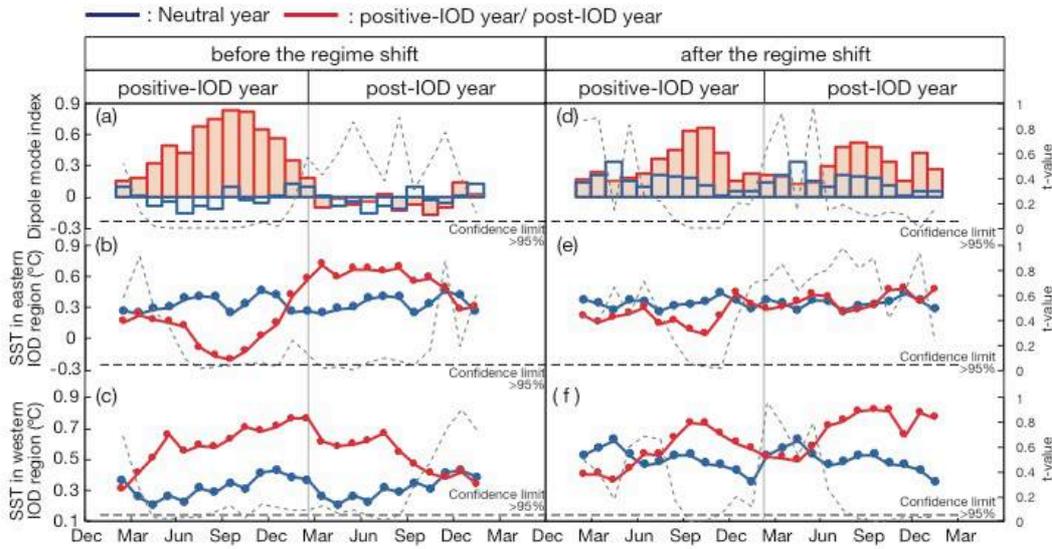
Fig.3-7

Seasonal Dipole mode index[1] (a) and SST anomalies[1] in western and eastern regions (b and c) during neutral years (blue line) and positive-IOD or post-IOD years (red line) before the regime shift. Dotted line: t-test results (neutral years vs. positive-IOD years and neutral years vs. the post-IOD years, respectively). Seasonal Dipole mode index (d) and SST anomalies in western and eastern regions (e and f) during neutral years (blue line) and positive-IOD or post-IOD years (red line) after the regime shift. Dotted line: t-test results (neutral years vs. positive-IOD years and neutral years vs. the post-IOD years, respectively).
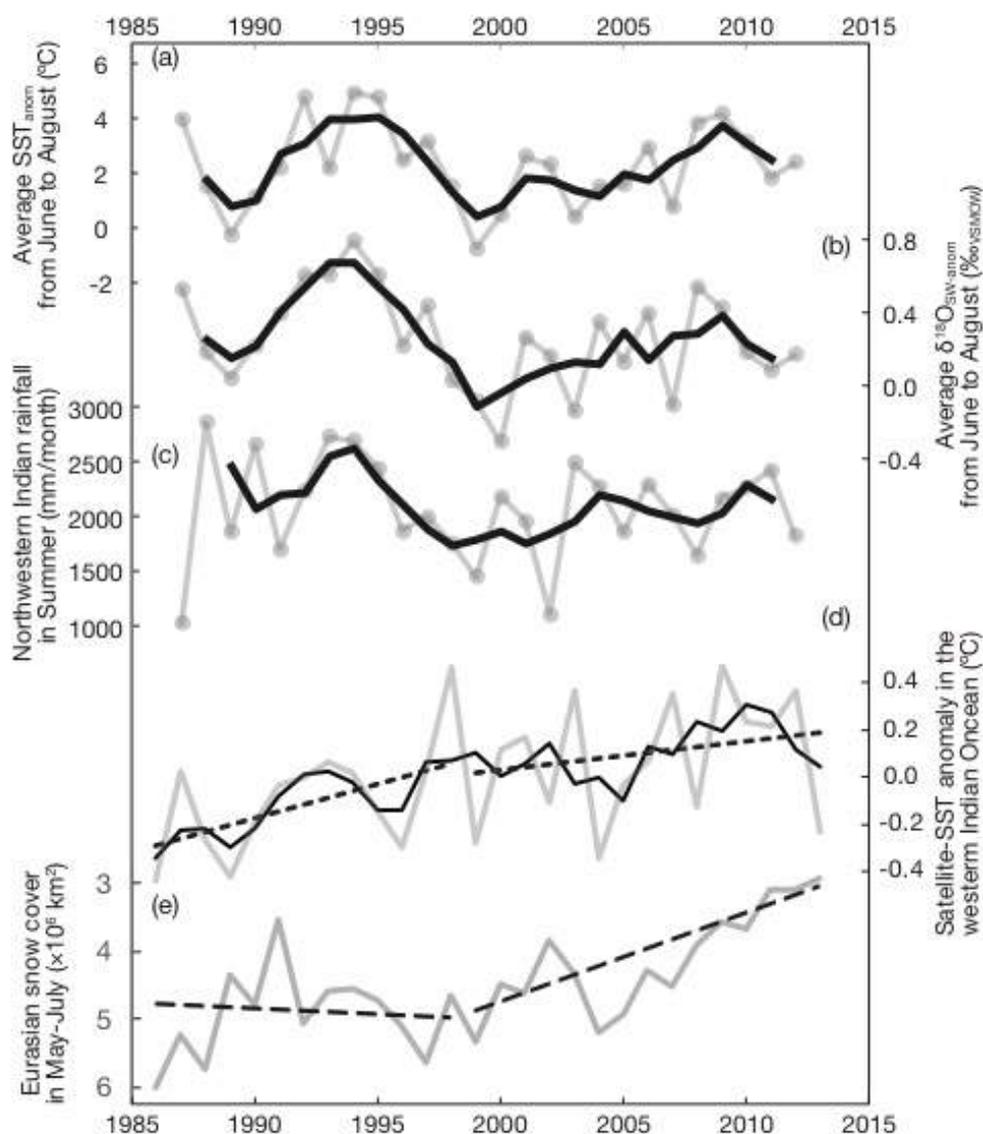
Fig.3-8

Coral, satellite and in situ records related to the SWM (gray line: seasonal average values, thick black line: 3-year moving averages and dotted line: trend line estimated by linear regression before and after the regime shift in 1999).

(a) Average SST_{anom} from June to August. (b) Average $\delta^{18}O_{sw-anom}$ from June to August. (c) Maximum rainfall from June to August in northwestern Indian. (d) Satellite derived SST anomaly in the late-spring (May-June) in the western equatorial Indian Ocean (5°S-5°N, 55-65E°). (e) The Eurasian snow cover in late-spring (May-June).

SST anomalies from the western Indian Ocean and Eurasian snow cover suggested the temperature gradient between the Eurasian and Indian Ocean increase.
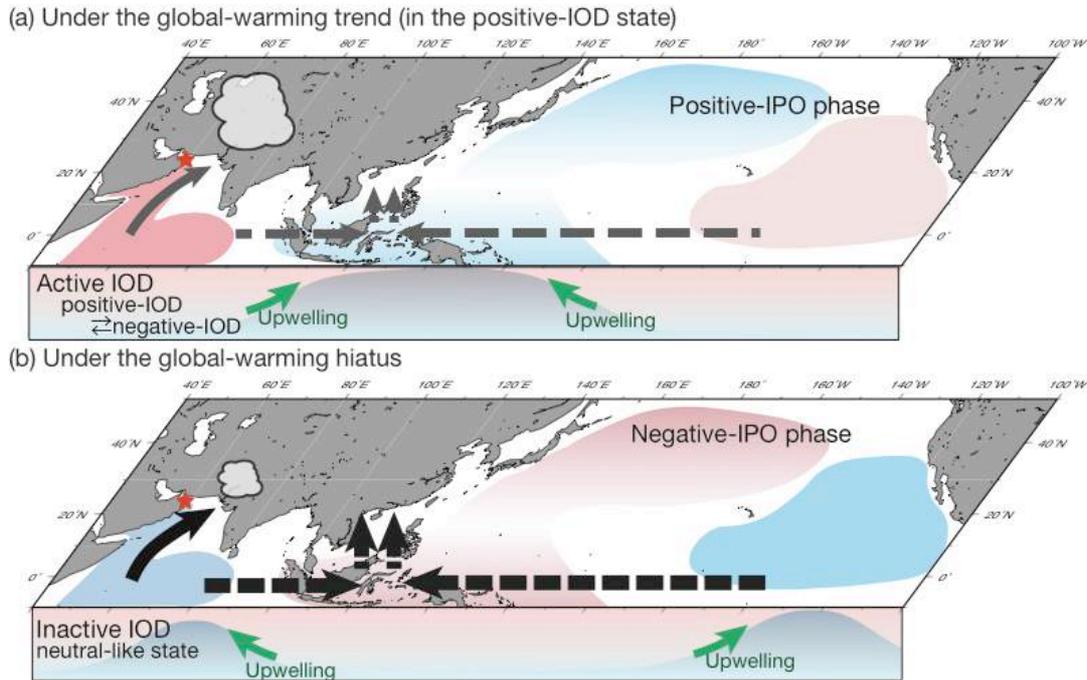
Fig.3-9

Schematic figures of the climate patterns in the Indian Ocean and the Pacific. The maps were generated using Generic Mapping Tools (GMT ver. 4.5.12[42]). (a) in the positive-IOD state during 20th century global-warming and (b) in the positive-IOD state during the global-warming hiatus. Map view: color shading indicates the SST gradient (warm: red, cold: blue) in each period. Vertical profiles: color shading indicates the thermocline depth along the equator (warm: red, cold: blue). Black (grey) arrows indicate the stronger (weaker) Walker circulation. Black (grey) solid allows indicate the strong (weak) Indian/Arabian summer monsoon. During the global-warming hiatus, the western Indian Ocean uncouples from the IOD.

4. Past summer upwelling events in the Gulf of Oman derived from a coral geochemical record

Abstract

On this chapter, we discussed revealing upwelling events in the Gulf of Oman using $\delta^{13}C_{coral}$. We used a high-resolution $\delta^{18}O_{coral}$, $\delta^{13}C_{coral}$ and Sr/Ca ratios. Our $\delta^{13}C_{coral}$ record shows the sharp negative peaks in the summer, indicating that 17 summer upwelling events occurred in the last 26 years. These anomalous negative peaks of $\delta^{13}C_{coral}$ result from upwelled water with depleted ^{13}C in dissolved inorganic carbon and decreased water-column transparency. We reconstructed the variations in the biweekly Sr/Ca ratio (SST proxy) and the oxygen isotope in seawater ($\delta^{18}O_{SW}$) based on the $\delta^{18}O_{coral}$ and Sr/Ca ratios and detected significant $\delta^{18}O_{SW}$ anomalies during the major upwelling events. Our results suggest that seasonal upwelling in the Gulf of Oman, which is driven by the Indian/Arabian Summer Monsoon, is subject to interannual variability.

4-1 Introduction

The Gulf of Oman is located on the northeastern coast of the Arabian Peninsula and both the Arabian Sea and the Gulf of Oman are located in arid environments. The climate is dominated by the seasonal reversal of the Indian/Arabian Monsoon, which in turn governs the surface wind field of the Indian Ocean north of 10° S. The intensity and direction of the monsoon winds vary seasonally. During the southwest (SW) Monsoon develops during the boreal summer (from June to mid-September) and is characterized by strong airflow across the Arabian Sea that feeds moisture and rainfall to the Indian subcontinent.

The Indian/Arabian Summer Monsoon causes coastal upwelling bringing cooler temperatures, nitrified and saline water to the sea surface along the southern coast of the Arabian Peninsula. Upwelled water flows northward and affects the oceanic stratification of the Gulf of Oman through gyres and eddy systems that sweep into the Oman Sea [Al-Azri et al., 2010]. The Northern Arabian Sea is therefore one of the most productive areas in the world [Qasim, 1982]. The SW Monsoon is also the major climatic factor affecting the near-shore environment and areas of coral growth in Oman during the summer months [Burt et al., 2016].

The high nutrient content of this water induces phytoplankton blooms. Satellite-based ocean color measurements show the temporal and spatial variability of the surface chlorophyll-a distribution along the coast of the Southern Arabian Peninsula [Wiggert et al., 2005]. In the Gulf of Oman, upwelling does not necessarily occur every summer [Elliot et al., 1990, Coles, 1997, Al-zri et al., 2013] In addition, observational records that allow us to understand the dynamics of upwelling events in the Gulf of Oman are scarce. Satellite based sea surface temperature (SST) in the Gulf of Oman did not reflect low SST excursions in summer measured by CTDs. (Fig. 1-7). Long-term and *in situ* records of primary production, salinity and temperature are necessary in order to understand upwelling events [Al-zri et al., 2013]. In this chapter, we used paleo-climatic reconstructions from coral geochemical records to provide a history of summer monsoon-driven upwelling variability in the Gulf of Oman.

4-2 Results and discussions

The $\delta^{13}C_{coral}$ also showed clear seasonal variation (Fig. 4-2) and distinct short-term negative anomalies (Fig.4-2-d). The $\delta^{13}C_{coral}$ analysis was performed to avoid contamination from organic matter. We measured each CO_2 gas sample 6 times using a dual inlet system loaded on a MAT251. Analytical precision of the $\delta^{13}C_{coral}$ (standard deviations) were below 0.05‰. Growth rate disturbances and anomalous-colored annual band were not observed on X-ray photographs and coral cores. Therefore, the variations of $\delta^{13}C_{coral}$ were assumed to reflect environmental changes rather than the coral growth disturbances.

Controlling factor of $\delta^{13}C_{coral}$

The interpretations of $\delta^{13}C_{coral}$ has been debated about what the $\delta^{13}C_{coral}$ values are reflecting. [Felis et al.,1998, McConnaughey, 1989a, McConnaughey, 1989b, Swart et al., 1996, Abram et al., 2003, Nozaki et al., 1978, Al-Rousan and Felis, 2013]. The main factors influence that can influence $\delta^{13}C_{coral}$ include: (1) kinetic effect and vital effect, (2) solar radiation, (3) water-column transparency, (4) variation of $\delta^{13}C_{DIC-SW}$ and (5) autotroph/heterotroph ratios.

Kinetic effects have been recognized as simultaneous ^{18}O and ^{13}C enrichment in coral skeletons with low extension rates. Strong kinetic effects mask vital effects [McConnaughey, 1989a]. In our core, $\delta^{13}C_{coral}$ values showed a weak negative correlation with the $\delta^{18}O_{coral}$ record (r = -0.317, n=634, P < 0.001: Fig. 4-3). Summer $\delta^{13}C_{coral}$ did not correlate significantly with $\delta^{18}O_{coral}$ (r=0.140, n=181, P > 0.05: Fig. 4-3). Winter $\delta^{13}C_{coral}$ had no significant correlation with winter $\delta^{18}O_{coral}$ (r = 0.04, P > 0.05, n = 159: Fig. 4-3). The extension rates show that the Oman coral grew very quickly, on average 25.1 mm/year with a range between 19 to 31.5 mm. These values were considerably higher than the critical value estimated for kinetic isotopic fractionation effects (4 mm/year) (Fig. 4-2-e) [McConnaughey, 1989b]. Therefore, the coral growth history and the lack of correlation between $\delta^{13}C_{coral}$ and $\delta^{18}O_{coral}$ suggest that the kinetic isotopic effect did not significantly affect this coral record.

Previous studies reported $\delta^{13}C_{coral}$ on seasonal and inter-annual variations are attributable to solar radiation [Fairbanks and Dodge, 1979, Klein et al., 1992]. To investigate the processes driving these $\delta^{13}C_{coral}$ fluctuations, we compared $\delta^{13}C_{coral}$ with satellite-based outgoing longwave radiation (OLR) (Fig. 4-4a) which reflect cloud cover. For a comparison of $\delta^{13}C_{coral}$ with monthly-resolved OLR data, biweekly resolved $\delta^{13}C_{coral}$ data were resampled at a monthly resolution using the software AnalySeries (version 2.0.8) [Paillard et al., 1996]. The $\delta^{13}C_{coral}$ were compared with OLR, and we calculated the correlation coefficients between these time series. $\delta^{13}C_{coral}$ without anomalous $\delta^{13}C_{coral}$ excursions positively correlated with OLR at a significant level (r=0.411, P < 0.01, n = 302: Figs. 4-4-a and b). A significant correlation appeared between the mean seasonal cycle of $\delta^{13}C_{coral}$ and OLR averaged over the past 26 years (r = 0.702, P = 0.01, n = 12: Figs. 4-4-c and d). The positive correlations between $\delta^{13}C_{coral}$ and OLR (Figs. 4-4-b and 4-4-d) suggests that $\delta^{13}C_{coral}$ captured the variation of photosynthetic activity caused by the seasonal solar radiation cycle. At inter-annual resolution, the 15 month-moving average profile of $\delta^{13}C_{coral}$ positively correlate with that of OLR (r = 0.347, P < 0.01, n = 303: Figs. 4-5-a and b). The duration of low OLR and coeval $\delta^{13}C_{coral}$ decreased from 1992 to 1993. We propose that insolation and OLR had decreased in globally as a result of up-stirred

volcanic aerosol from the eruption of Mount Pinatubo, the Philippines in June 1991[28]. Low $\delta^{13}C_{coral}$ from 1992 to 1993 would be influenced by decreasing insolation which resulted from the volcanic eruption of Mount Pinatubo.

Comparing past upwelling with $\delta^{13}C_{coral}$

We calculated the $\delta^{13}C_{coral}$ anomaly ($\delta^{13}C_{anomaly}$) by removing the 15 month-moving average (31 bi-weekly data point) after subtracting the averaged seasonal cycle of $\delta^{13}C_{coral}$. The threshold for $\delta^{13}C_{coral}$ anomalous excursions was determined as a standard deviation of 1σ: ±0.343‰$_{VPDB}$. In summer, the anomalous negative excursions of the $\delta^{13}C_{anomaly}$ occurred 17 times in summer, while 1 anomalous negative excursion occurred in the spring of 1993 (Fig. 4-2). Anomalous positive $\delta^{13}C_{anomaly}$ excursions were also observed prior to summer negative $\delta^{13}C_{anomaly}$ excursions. The $\delta^{13}C_{anomaly}$ had no significant correlation with OLR anomaly calculated by same procedure (r = 0.05, P > 0.3 Figs. 4-5-c and 4-5-d), suggesting that anomalous negative excursions of $\delta^{13}C_{anomaly}$ in the summer (AN-$\delta^{13}C$) would not be generated from OLR variations.

We examined the timing of the AN-$\delta^{13}C$ with the compiled evidence of each past upwelling event documented from *in situ* and satellite observations (Figs.4-2). Abrupt SST decreasing events in summer were revealed in 1987-1989 and 2000 from satellite SST data, in 1992, 1994, 2001, 2002 (Fig. 4-6) and 1990 based on *in situ* SST data, and 2010 based on our vertical seawater temperature profile (Fig. 4-7) [Glynn, 1993, Claereboudt, 2006, Coles, 1997, Wiggert et al., 2005, Quinn and Johnson, 1996]. The vertical profile of seawater temperature deduced by temperature sensors attached to the diving gear of local volunteer divers in 2010, also suggest that the thermocline was closer to the surface during summer upwelling events (Fig. 4-7). In addition, Al-Azri *et al.* (2010) had measured chlorophyll-a concentrations, nutrients, phytoplankton density and SST in Fahal Island (23.67ºN, 58.5ºE) and Bandar Al Khayran (23.51ºN, 58.72ºE: near to our coral sample site). From July to September 2004, upwelling was observed as increasing chlorophyll-a concentrations and phytoplankton density as well as decreasing SST [Al-Azri *et al.*, 2010]. In August 2005, SST decreased for 1 month, while other parameters did not change [Al-Azri *et al.*, 2010]. Al-Azri *et al.* (2013) reported that *in situ* chlorophyll-a and satellite based SST suggested that upwelling also occurred in July, 2008 [Al-Azri *et al.*, 2013]. The satellite observations (SeaWiFS and MODIS at 24ºN, 58ºE from Asia-Pacific Data Research Center) from 1997 to 2013 suggested that chlorophyll-a concentrations in the Gulf of Oman increased in August 2000, September 2004 and August 2008 (Fig. 4-8). In other upwelling years, chlorophyll-a concentrations in satellite data were not available to compare with AN-$\delta^{13}C$ due to the lack of satellite data in summer.   Based on these *in situ* and satellite datasets, past upwelling events occurred in 1987, 1988, 1989, 1990, 1992, 1994, 2000-2002, 2004, 2008 and 2010 (Fig. 4-2) [Glynn, 1993, Quinn and Johnson, 1996, Coles, 1997,

Claereboudt, 2006, Al-Azri et al., 2010, Al-Azri et al., 2013]. The AN-δ^{13}C corresponds with these past upwelling events.

Controlling factor of negative peaks of $\delta^{13}C_{coral}$ with upwelling

The possible controlling factors of the AN-δ^{13}C with upwelling events are: (1) decreasing water-column transparency [Yamazaki et al., 2009], (2) variations of $\delta^{13}C_{DIC-SW}$ [Abram et al., 2003, Kroopnick, 1985], and (3) change to heterotroph feeding [Felis et al., 1996]. It is known that increasing chlorophyll-a concentrations correspond with upwelling events inducing phytoplankton blooms, thereby decreasing water-column transparency and depleting $^{13}C_{coral}$ with low photosynthetic activities of zooxanthellae [Al-Azri et al., 2010, Al-Azri et al., 2013, Yamazaki et al., 2009]. Moreover, lower $\delta^{13}C_{DIC-SW}$ supply from greater depths decreases $\delta^{13}C_{DIC-SW}$ at the sea surface [Nozaki et al., 1978, Al-Rousan and Felis, 2013, Kroopnick, 1985]. Upwelling events may produce an AN-δ^{13}C due to sudden decreases in water-column transparency and $\delta^{13}C_{DIC-SW}$. Heterotrophic feeding would also be the controlling factor of negative $\delta^{13}C_{coral}$ with upwelling events. A study reported that corals feeding ^{13}C-depleted zooplankton decreased their $\delta^{13}C_{coral}$ [Grottoli and Wellington, 1999]. The coral records from the Gulf of Aqaba, Red Sea suggested that increasing heterotrophy with upwelling decreased $\delta^{13}C_{coral}$ for an approximately half a year [Felis et al., 1998]. Afterwards, $\delta^{13}C_{coral}$ could be increased by the preferential uptake of ^{12}C by phytoplankton at the sea surface. In the western Indonesian coast, it was reported that $\delta^{13}C_{coral}$ increased by approximately 2.2‰$_{VPDB}$ after large phytoplankton blooms due to upwelling [Abram et al., 2003].

We propose the following mechanism to explain the short-term negative peaks in the $\delta^{13}C_{coral}$: 1. Upwelling events bring deep, cold and nutrient-rich water with low $\delta^{13}C_{DIC-SW}$ to the surface in summer. Upwelling events cause unusually high nutrient conditions in the Gulf of Oman. Photosynthesis activities in zooxanthella would be emphasized in eutrophic conditions and temporarily increased $\delta^{13}C_{coral}$. 2. Lower $\delta^{13}C_{DIC-SW}$ from the deep-sea decreases $\delta^{13}C_{coral}$. 3. Phytoplankton blooms arise from a nutrient supply to the sea surface. 4. Phytoplankton primarily depletes $^{12}CO_{2-SW}$. Active phytoplankton photosynthesis increases $^{13}CO_{2-SW}$. 5. $\delta^{13}C_{coral}$ increases with the restoration of $\delta^{13}C_{DIC-SW}$.

Reconstruction of unknown upwelling events

We compared the AN-δ^{13}C minima with the upwelling periods (number of the days) in summer (Figs. 4-6, 4-7 and 4-9). *In situ* daily to weekly SST data in 1992, 1994, 2001, 2002 and 2010 revealed that SST during upwelling events was as same as winter SST (23.5°C), and daily fluctuations of SST in upwelling periods ranged within 3°C. Therefore, the numbers of the days for upwelling periods were defined as the duration of SST lower than

26.5°C in summer. $\delta^{13}C_{anomaly}$ values of no upwelling years (0 days) was estimated from *in situ* $\delta^{13}C_{DIC-SW}$ in Arabian Sea (+1.325 ‰$_{VPDB}$ at 0-10 m depth in non-upwelling seasons: Peeters, 2002) and the value of δ^{13}C in isotopic equilibrium between coral carbonate and seawater [Romanek et al., 1992]. The AN-δ^{13}C minima were correlated to the upwelling periods as below.

$$\text{Upwelling periods (days)} = -87.16 \pm 16.40 \times \text{AN-}\delta^{13}\text{C minima (‰}_{VPDB}) - 4.92 \pm 9.45$$

$$(r = -0.937, P < 0.05; \text{Fig. 4-9}).$$

Then, past upwelling periods in the year with no *in situ* SST data were reconstructed from each AN-δ^{13}C using this equation (Fig. 4-9). The estimated uncertainty for reconstructed upwelling-periods was 12.66 days (1σ) including the analytical precisions of $\delta^{13}C_{coral}$, the intercept and the slope of this equation. In 1987, 2006, 2008, 2009, each upwelling period was extremely long, over 120 days (Fig. 4-9). In those years, coral extension rates decreased to 23 mm/year (Fig. 4-2). The long upwelling events would therefore have a negative effect on coral extension rate due to eutrophic conditions and decreased water-column transparency.

We compared the reconstructed upwelling events from AN-δ^{13}C (Fig. 4-9) with Sr/Ca ratios and $\delta^{18}O_{SW-anomaly}$ (Fig 4-2). Sr/Ca ratios showed 1-month increasing (cooling) in summer except in 1994, 2001, 2002, 2006, and 2009, however, these did not correspond to reconstructed upwelling events. In non-AN-δ^{13}C (upwelling) years (1989, 1991, 1997-1998, 2003, 2007, 2011-2012), the $\delta^{18}O_{SW-anomaly}$ was low in summer. Upwelling events in the Gulf of Oman are driven by the SW Monsoon, which causes strong seasonal winds parallel to the coast of Southern Oman in the Arabian Sea, while the associated Ekman transport creates strong upwelling along the coastal margins, bringing cold, nutrient-rich water to the surface [Al-Azri et al., 2010, Wiggert et al., 2005]. This upwelled water has indirect impacts on corals and reef areas farther north through gyres and eddy systems that sweep into the Oman Sea [Al-Azri et al., 2010, Wiggert et al., 2005]. In addition, upwelling may be influenced by vertical seawater density, depending on SST and SSS [Kumar and Prasad, 1999]. The $\delta^{18}O_{SW-anomaly}$ record suggested that deep seawater did not reach the sea surface as low-density water masses might form a cap on the sea surface in the Gulf of Oman.

4-3 Conclusions

Observations suggest that the primary productivity of the Gulf of Oman is subject to inter-annual variability [Al-Azri et al., 2010], but long-term observational records are lacking. Our new $\delta^{13}C_{coral}$ record captured past upwelling events and their periods in the Gulf of Oman for 26 years. Thus, coral skeletal archives fill an important gap in the observational record and have great potential for increasing our understanding of the upwelling mechanisms in the Gulf of Oman.

References

1. Al-Azri, A. R., Piontkovski, S. A., Al-Hashmi, K. A., Goes, J. I. & Do Gomes, H. R. Chlorophyll a as a measure of seasonal coupling between phytoplankton and the monsoon periods in the Gulf of Oman. *Aquat. Ecol.* **44,** 449–461 (2010).

2. Qasim, S. Z. Oceanography of the northern Arabian Sea. *Deep Sea Res. Part A. Oceanogr. Res. Pap.* **29,** 1041–1068 (1982).

3. Burt, J. A. *et al.* Oman's coral reefs: A unique ecosystem challenged by natural and man-related stresses and in need of conservation. *Mar. Pollut. Bull.* **105,** 498–506 (2016).

4. Wiggert, J. D., Hood, R. R., Banse, K. & Kindle, J. C. Monsoon-driven biogeochemical processes in the Arabian Sea. *Prog. Oceanogr.* **65,** 176–213 (2005).

5. Elliott, A. J. & Savidge, G. Some features of the upwelling off Oman. *J. Mar. Res.* **48,** 319–333 (1990).

6. Coles, S. L. Reef corals occurring in a highly fluctuating temperature environment at Fahal Island, Gulf of Oman (Indian Ocean). *Coral Reefs* **16,** 269–272 (1997).

7. Al-Azri, A. R. *et al.* Mesoscale and Nutrient Conditions Associated with the Massive 2008 *Cochlodinium polykrikoides* Bloom in the Sea of Oman/Arabian Gulf. *Estuaries and Coasts* **37,** 325–338 (2013).

8. Cobb, K. M., Charles, C. D., Cheng, H. & Edwards, R. L. El Niño/Southern Oscillation and tropical Pacific climate during the last millennium. *Nature* **424,** 271–276 (2003).

9. Watanabe, T. *et al.* Permanent El Niño during the Pliocene warm period not supported by coral evidence. *Nature* **471,** 209–211 (2011).

10. Felis, T., Pätzold, J., Loya, Y. & Wefer, G. Vertical water mass mixing and plankton blooms recorded in skeletal stable carbon isotopes of a Red Sea coral. *J. Geophys. Res.* **103,** 30731 (1998).

11. Tudhope, A. W., Lea, D. W., Shimmield, G. B., Chilcott, C. P. & Head, S. Monsoon Climate and Arabian Sea Coastal Upwelling Recorded in Massive Corals from Southern Oman. *Palaios* **11,** 347 (1996).

12. Gagan, M. K. *et al.* Temperature and Surface-Ocean Water Balance of the Mid-Holocene Tropical Western Pacific. *Science* **279,** 1014–1018 (1998).

13. McConnaughey, T. ^{13}C and ^{18}O isotopic disequilibrium in biological carbonates : I. Patterns. *Geochim. Cosmochim. Acta* **53,** 151–162 (1988).

14. McConnaughey, T. ^{13}C and ^{18}O isotopic disequilibrium in biological carbonates: II. In vitro simulation of kinetic isotope effects. *Geochim. Cosmochim. Acta* **53,** 163–171 (1989).

15. Swart, P. K., Leder, J. J., Szmant, a. M. & Dodge, R. E. The origin of variations in the isotopic record of

scleractinian corals: II. Carbon. *Geochim. Cosmochim. Acta* **60,** 2871–2885 (1996).

16. Abram, N. J., Gagan, M. K., McCulloch, M. T., Chappell, J. & Hantoro, W. S. Coral reef death during the 1997 Indian Ocean Dipole linked to Indonesian wildfires. *Science* **301,** 952–955 (2003).

17. Fairbanks, R. G. & Dodge, R. E. Annual periodicity of the $^{18}O/^{16}O$ and $^{13}C/^{12}C$ ratios in the coral Montastrea annularis. *Geochim. Cosmochim. Acta* **43,** 1009–1020 (1979).

18. Nozaki, Y., Rye, D. M., Turekian, K. K. & Dodge, R. E. A 200 year record of carbon-13 and carbon-14 variations in a Bermuda coral. *Geophys. Res. Lett.* **5,** 825–828 (1978).

19. Al-Rousan, S. & Felis, T. Long-term variability in the stable carbon isotopic composition of *Porites* corals at the northern Gulf of Aqaba, Red Sea. *Palaeogeogr. Palaeoclimatol. Palaeoecol.* **381–382,** 1–14 (2013).

20. Klein, R., Pätzold, J., Wefer, G. & Loya, Y. Seasonal variations in the stable isotopic composition and the skeletal density pattern of the coral *Porites lobata* (Gulf of Eilat, Red Sea). *Mar. Biol.* **112**, 259–263 (1992).

21. Paillard, D., Labeyrie, L. & Yiou, P. Macintosh Program performs time-series analysis. *Eos, Trans. Am. Geophys. Union* **77,** 379 (1996).

22. Trenberth, K. E. & Dai, A. Effects of Mount Pinatubo volcanic eruption on the hydrological cycle as an analog of geoengineering. *Geophys. Res. Lett.* **34**, 1–5 (2007).

23. Glynn, Peter W. Monsoonal upwelling and episodic Acanthaster predation as probable controls of coral reef distribution and community structure in Oman, Indian Ocean. *Atoll Research Bulletin* 379.379 (1993).

24. Quinn, N. J., and D. W. Johnson. Cold water upwellings cover Gulf of Oman coral reefs. *Coral Reefs-Journal of the International Society for Reef Studies* **15.4**, 214-214 (1996).

25. Claereboudt, M. R. Reef corals and coral reefs of the Gulf of Oman. *Historical Association of Oman*, 322 (2006).

26. Yamazaki, A. et al. Reconstructing palaeoenvironments of temperate regions based on high latitude corals at Tatsukushi Bay in Japan. *J. Japanese Coral Reef Soc.* **11**, 91–107 (2009).

27. Kroopnick, P. M. The distribution of ^{13}C of ΣCO_2 in the world oceans. Deep Sea Res. Part A. *Oceanogr. Res. Pap.* **32**, 57–84 (1985).

28. Grottoli, a. G. & Wellington, G. M. Effect of light and zooplankton on skeletal $\delta^{13}C$ values in the eastern Pacific corals *Pavona clavus* and *Pavona gigantea*. *Coral Reefs* **18**, 29–41 (1999).

29. Peeters, F. The effect of upwelling on the distribution and stable isotope composition of *Globigerina bulloides* and *Globigerinoides ruber* (planktic foraminifera) in modern surface waters of the NW Arabian Sea. *Glob. Planet. Change* **34,** 269–291 (2002).

30. Romanek, C. S., Grossman, E. L. & Morse, J. W. Carbon isotopic fractionation in synthetic aragonite and calcite: Effects of temperature and precipitation rate. *Geochim. Cosmochim. Acta* **56,** 419–430 (1992).

31. Kumar, S. P. & Prasad, T. G. Formation and spreading of Arabian Sea high-salinity water mass. *J. Geophys. Res.* **104,** 1455 (1999).

Figure. 4-1 Scatterplot of SST measured by CTD vs. SST based on satellite in the Gulf of Oman for 10
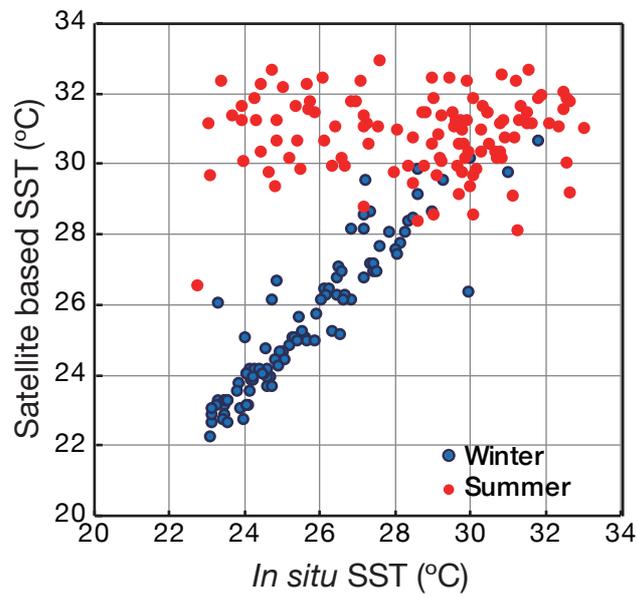
years. Winter SST had a high correlation between *in situ* SST and satellite-based. Whereas for summer temperature, the correlation between *in situ* SST and satellite was nearly 0.
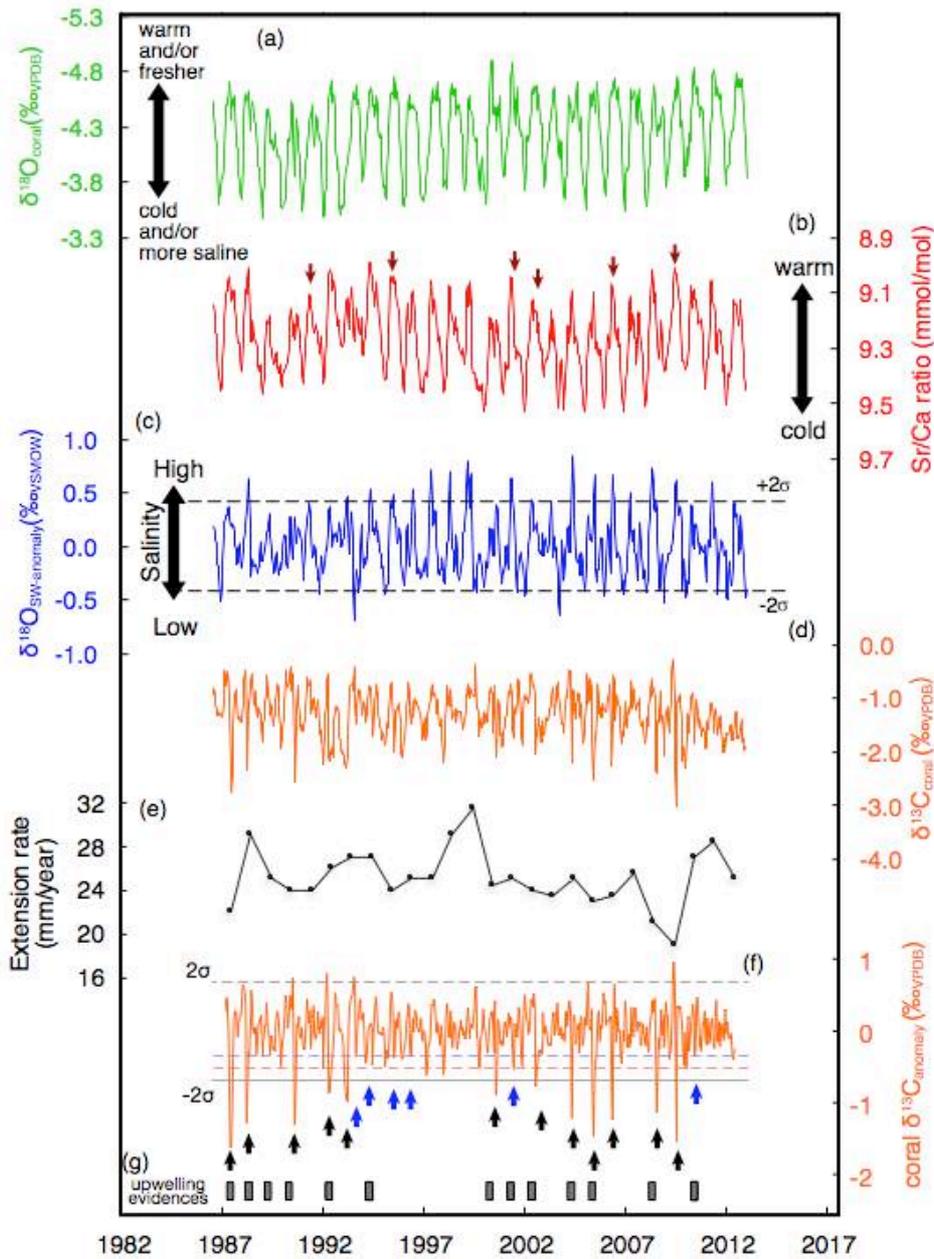
Figure 4-2 Oman coral proxy records and extension rate. (a) Coral skeletal $\delta^{18}O_{VPDB}$ record, (b) Coral skeletal Sr/Ca ratio record. Grey arrows indicate the years of non-increasing Sr/Ca ratios in summer. (c) $\delta^{18}O_{SW\text{-}anomaly}$, (d) Coral skeletal $\delta^{13}C_{VPDB}$ record, (e) Extension rate calculated from distances between the anchor points in winter of each year. (f) Oman coral skeletal $\delta^{13}C_{VPDB}$ anomaly. The timing of anomalous negative excursions of AN-$\delta^{13}C$ in the summer are shown as black arrows. (g) *In situ* data showing low-SST and high chlorophyll-a (square symbols).
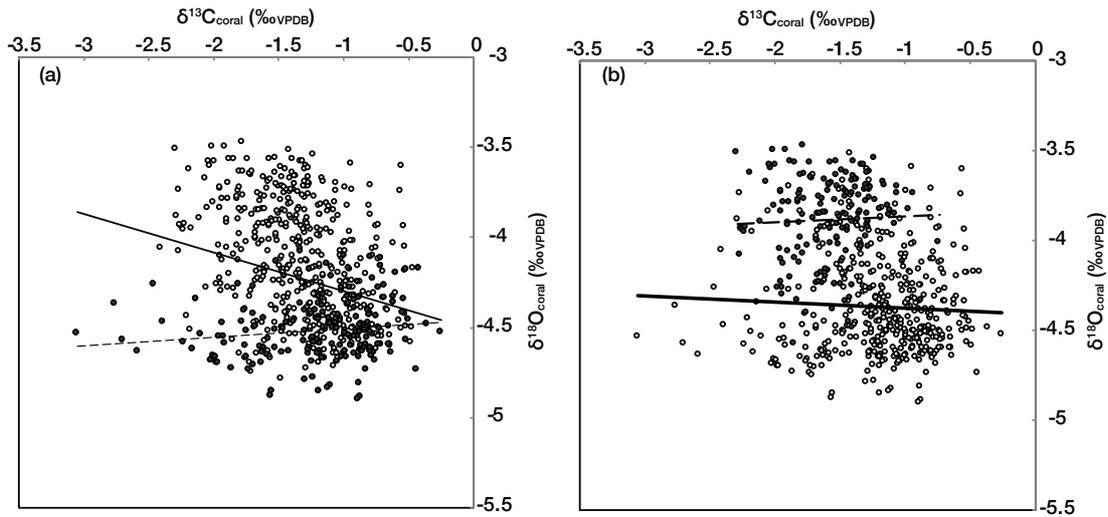
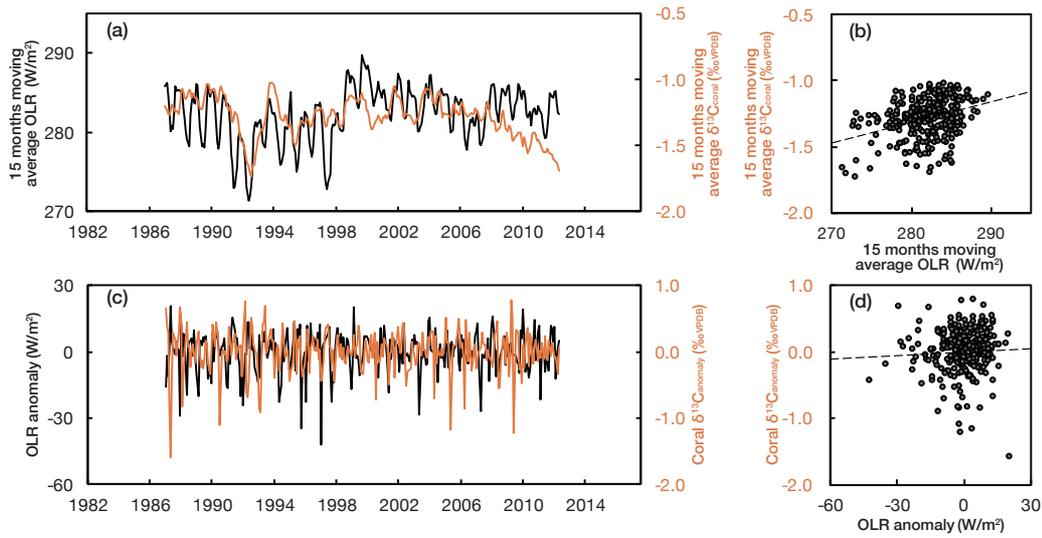**Figure 4-3**. (a)Scatterplots of $\delta^{13}C_{coral}$ vs. $\delta^{18}O_{coral}$ with all data (white dots) and summer values only (black dots). A significant positive correlation is not observed in either scatterplot.

(b) Scatterplots of $\delta^{13}C_{coral}$ vs. $\delta^{18}O_{coral}$ without winter (open circle) and winter values (filled dots). Significant correlation was not confirmed.

**Figure 4-4**. (a) OLR[41](orange line) and δ^{13}C$_{coral}$(black line). (b) Scatterplot of δ^{13}C$_{coral}$ and OLR data[41]. Solid circles: δ^{13}C$_{coral}$ vs. OLR for the monthly time series from 1986 to 2013 without anomalous δ^{13}C$_{coral}$ peaks (r = 0.411, P < 0.01). (c) The climatologies of OLR (orange line) and δ^{13}C$_{coral}$(black line) from 1986 to 2013. (d) Monthly mean data of δ^{13}C$_{coral}$ vs. OLR. The error bar indicates the standard deviation (1σ) of the monthly mean values (r = 0.702, P < 0.01) This averaged seasonal variations of δ^{13}C$_{coral}$ and OLR were calculated from these dataset during 1986-2013.   Regression lines were shown in each diagram.

Figure 4-5. (a) The 15 months moving average profile of OLR[41] (orange line) and $\delta^{13}C_{coral}$ (black line). (b) The scatter diagrams between moving averaged OLR[41] and $\delta^{13}C_{coral}$. (c) $\delta^{13}C_{anomaly}$ (orange line) and OLR anomaly (black line). (d) Scatterplots of $\delta^{13}C_{anomaly}$ vs. OLR anomaly. Anomaly dataset showed no correlations (r = 0.09, P > 0.05).
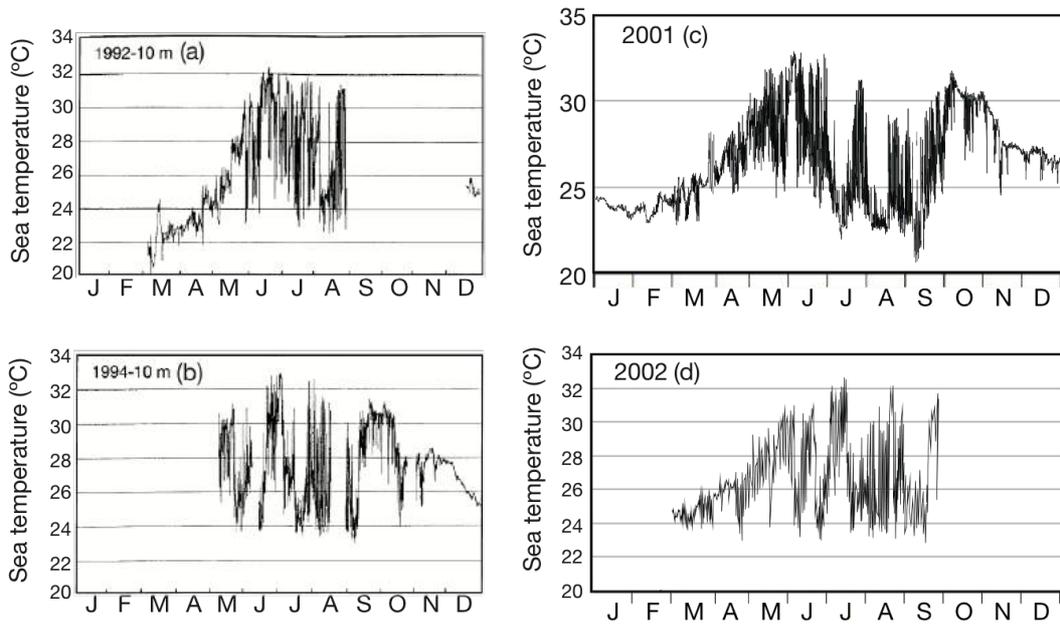
Figure 4-6 *In situ* seawater temperature profile at Fahal Island (23.67°N, 58.5°E) in 1992 at 10m depth (a) and 1994 at 10m depth (temperature data from Coles, 1997[6]) (b).

In situ SST at Qalhat, Oman in 2001 at 6m depth (c) and 2002 at 6m depth (unpublished data, Claereboudt) (d). Seawater temperature profiles in 1992 ,1994 ,2001, and 2002 recorded upwelling-deduced abrupt decreases in summer.
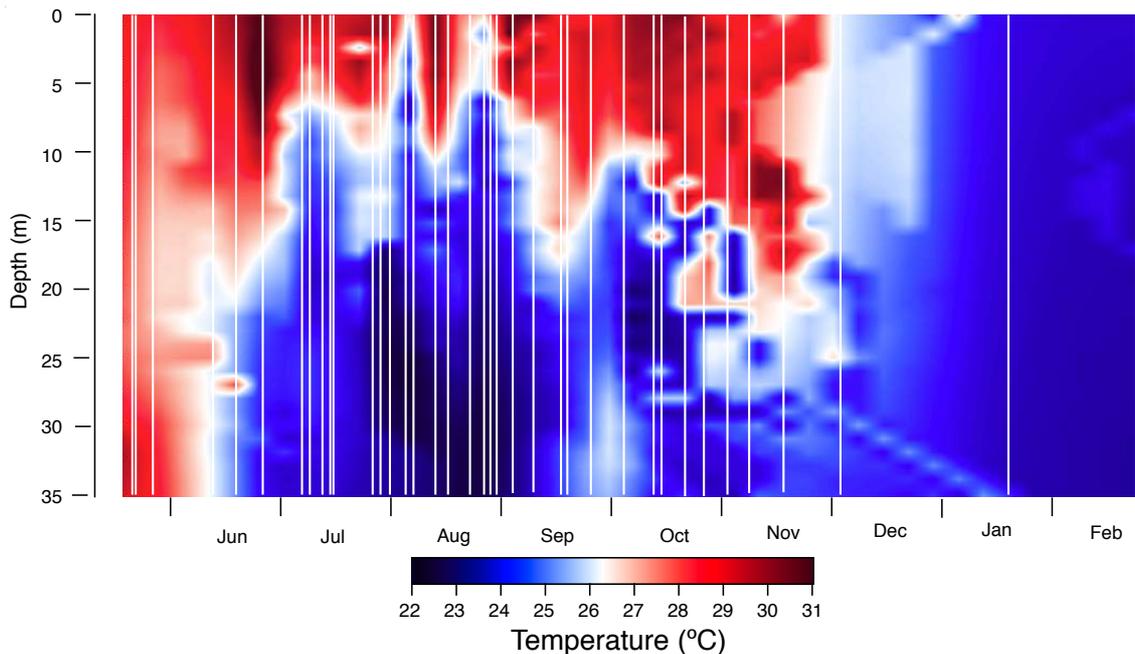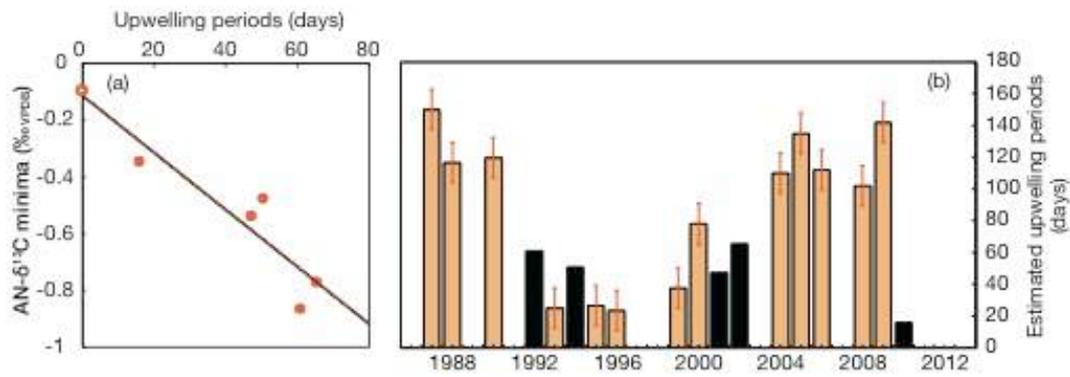

Figure 4-7 The vertical profiles of seawater temperature nearby coral sampling site in 2010. The depth

85

profiles of temperatusing gear of local volunteer divers.
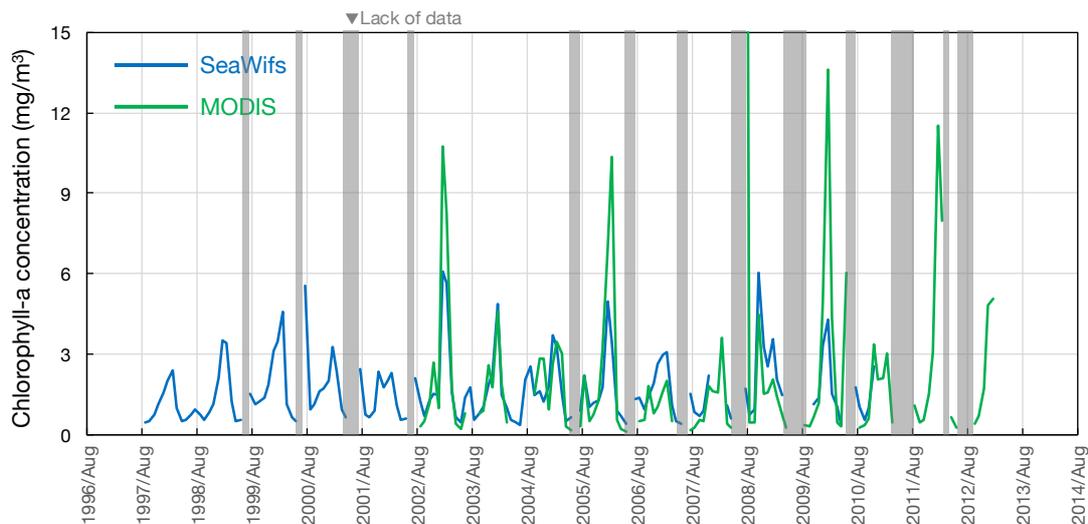
Figure 4-8 Chlorophyll-a concentrations from 1997 to 2013 based on satellite observations[32] (Blue line: SeaWiFS, Green line: MODIS at 24N, 58E). Grey bars indicated the periods of a lack of data.

Figure 4-9 (a) Cross-plot of *in situ* low-SST periods and AN-$\delta^{13}C$ minima. The dotted line indicates the regression between *in situ* low-SST periods and AN-$\delta^{13}C$ minima (filled circles) and estimated $\delta^{13}C_{anomaly}$ value for no upwelling periods (r = - 0.937, P < 0.05, n = 6). The $\delta^{13}C_{anomaly}$ value for no upwelling (open circle) was estimated from *in situ* $\delta^{13}C_{DIC-SW}$ from the Arabian Sea and the value of $\delta^{13}C$ in isotopic equilibrium between coral carbonate and seawater (b) Estimated upwelling periods from AN-$\delta^{13}C$ minima. Black bars indicate the years which were used for the regression between *in situ* low-SST periods and $\delta^{13}C_{anomaly}$ minima.

88

5. Indian monsoon reconstruction in the last millennium using fossil corals from the Arabian Sea

Abstract

Summer Indian monsoon generates upwelling in the Arabian Sea and provides wet seasons in India during summer. We showed the relationships between upwelling and Indian precipitations using modern and fossil Porites corals from the Mashirah Island, the Arabian Sea. 6 years records of Sr/Ca, $\delta^{18}O_{sw}$, $\delta^{13}C_{coral}$ were generated from the modern Arabian coral. SST proxies (Sr/Ca and $\delta^{18}O_c$) reflected SST variations of winter and summer cooling. $\delta^{18}O_{sw}$ decreased in summer. This negative excursion of $\delta^{18}O_{sw}$ reflected inflow of seawater with enriched $^{16}O_{sw}$ from deep sea. SST deduced from Sr/Ca correlated with northwestern Indian precipitations. Variations of $\delta^{18}O_{sw}$ were similar trend with precipitations in the northwestern India. Active evaporation in weak upwelling would transport much precipitations to India and increase Indian precipitations. SST records from fossil corals in Medieval warm period to little ice age (LIA) were not different from the present. However, $\delta^{18}O_{sw}$ in summer of LIA was much lower than the present and period of decreasing excursions of $\delta^{18}O_{sw}$ in 1964 was shorter than the present. These suggest that upwelling in LIA would be shorter and stronger than the present. This shorter upwelling period would increase precipitation in northwestern India and made prosperity empire in India.

5-1. Introduction

Indian monsoon in summer

Indian monsoon is one of the principle climatic factor in the Indian Ocean. Directions and intensities of Indian monsoon was seasonally changed [Fig. 1-5, Schott, and McCreary, 2001]. Indian monsoon controls precipitation in circum-Indian Ocean region [Fig. 1-5]. Summer Indian monsoon supplies precipitation in wet season in India. The maximum precipitation per one-month reach 2012 ± 388 mm/month in wet season (May-Oct. in last 15years) at the northwestern India. In Dry seasons, the maximum precipitation per month was only 160±96 mm/month in last 15years. This much precipitation in the northwestern India is source of Indus river and utilized for agriculture [Kumar et al., 2004].

Indian monsoon in summer affects atmosphere-ocean interaction, because this wind generates coastal upwelling in summer along the southern coast of Arabian Peninsula [Brock et al., 1991, Fig.1-6]. On an influence of this upwelling, the Arabian sea in summer is cooling similar with winter SST and the highest productive area in the tropic oceans [Fig.5-1]. Due to two reductions of SST for one year (summer and winter), SST in the Arabian Sea has a half year cycle [Tudhope et al., 1996]. High temporal resolution (monthly-seasonally) records are necessary to reconstruct Indian monsoon and upwelling using oceanic proxy. Because lower $\delta^{18}O_{sw}$ from deeper sea would decrease positive excursions of $\delta^{18}O_{coral}$ (low SST in upwelling seasons), Indian monsoon reconstruction via upwelling is required Sr/Ca (for only SST proxy) [Tudhope et al., 1996].

Background of Last millennium

After the recent industrialization (ca. CE1850), obvious global-warming trend is confirmed by both observations of surface air-temperature and reconstructions of SST using coral skeleton [Abram et al., 2016]. Ocean-atmospheric interaction phenomena become strong as an impact of the global-warming trend [Abram et al., 2008, Nakamura et al., 2009, England et al., 2014]. However, there are still debate about whether the global-warming trend affects ocean-atmospheric interaction phenomena.

The little ice age (LIA) was believed as the most recent cold era (ca. CE1400 to 1800). In LIA, radiation became weaker than the recent years and the periods before CE1400 [Lean et al., 1995,

Bard et al., 2006]. The influence of weaker insolation decreased air-temperature and SST in LIA. Air temperature and SST became *ca.* 0.5-1℃ colder in the northern hemisphere than the global warming period (abbreviated as GWT-era).

In particular, the era in 1645-1715 was called as "Maunder minimum" [Lean et al., 1995]. In the Maunder minimum, sunspot number became near to zero based on observations of sunspot [Bard et al., 2006]. air-temperature and SST decreased in this era. In Maunder minimum, due to air temperature decreasing, social incidents occurred in Europe. Medieval warming period (MWP) was mainly defined as period when stated from CE900-1000 and ended in CE1300-1400 (Mann et al., Graham 2011). In the last millennium, air temperature in the recent years was similar with the MWP.

During the Little Ice age, the empire in the India (Mughal Empire) developed. The Mughal Empire started in the northern India (capital: Delhi) from 1526. The Mughal Empire in 17th century was the most prosperous in this empire's history. The Mughal Empire succeeded to rule the entire India from the early 18th century. However, after success of unification of India, the Mughal Empire started to decline. Finally, this empire was collapsed in the middle 18th century (%%). History of the Mughal Empire was complexed because it is unknown that the relationships among agriculture, industrialization and climate changes. A previous work reconstructed amounts of precipitation in the northern India using the speleothems, they concluded that climatic changes were affected on the more northern Indian region (Tibet region). They suggested decreasing rend of precipitation in northern India would contribute to collapse of Guge kingdom in 1630.

Monsoon and rainfall variations through the last millennium

Monsoon was generated by temperature-gradient based on insolation-gradient between northern and southern region [Schott, and McCreary, 2001]. Indian monsoon was generated by temperature gradient between the Eurasian continent and Indian Ocean. This temperature gradient became emphasis in boreal summer. Due to intensified temperature gradient in summer, Indian monsoon was also intensified and induced precipitation at India.

Indian monsoon reconstructions through the Holocene using speleothems and sediment cores revealed Indian monsoon weakened due to the weakened insolations [Gupta et al., 2003, Fleitmann et al., 2003, Wang et al., 2005]. By cause of weak monsoon, northern latitudinal limit of intertropical convergence

zone (rainfall belt) would retreated to south [Yan et al., 2015]. As a result, previous study believed northern region could become arid and southern region in northern hemisphere became humid [Lechleitner et al., 2017].

On this chapter, at first, we calibrate influences of Indian monsoon and upwelling on the modern coral records from the Arabian Sea and the Gulf of Oman. By using calibration results, we reconstruct differences of the Indian monsoon intensity and Indian precipitations in MWP, LIA and GWT-era. It is still under debate whether long-term variations of air-temperature and SST affect on variations of radiation equatorial ocean-atmosphere circulations in the last millennium [Cobb et al., 2003, Abram et al., 2016]. Indian monsoon variations were also unknown in these era..

5-2 Materials of the Arabian corals

On March 25, 2015, *Porites sp.* Colonies (10 cm height) were collected from the Mashirah island, the southern coast of Arabian Peninsula. We used one Porites coral for geochemical analysis. We found fossil corals as high energy deposit at Mashira Island. For screening diagenetic samples, X-ray diffractions and SEM observations were conducted. U-Th age determinations were revealed one sample in MWP, two in LIA and one in CE1960 (shown on Table5-1). Sr/Ca and $\delta^{18}O_{coral}$ in the Arabian modern and fossil corals were measured (see Chapter 2 general methods section).

5-3 Calibration using the Arabian modern coral

Results of the Arabian corals

Sr/Ca and $\delta^{18}O_{coral}$ showed 6 distinct annual cycles with positive excursions of Sr/Ca and $\delta^{18}O_{coral}$ in summer (Fig.5-1). The average of the Sr/Ca ratios was 9.33 (mmol/mol), with values ranging from 9.05 to 9.68 (mmol/mol). The $\delta^{18}O_{coral}$ averaged -4.35 (‰$_{VPDB}$) and ranged from -4.84 to -3.70 (‰$_{VPDB}$). The average of $\delta^{13}C_{coral}$ was -1.62 (‰$_{VPDB}$) and ranged from -3.28 to +0.29 (‰$_{VPDB}$).

We calculated the regression line between IGOSS-SST and Oman coral Sr/Ca using seasonal winter minima, summer minima and two summer maxima to avoid potential biases due to intra-seasonal age model uncertainties. as follows [Fig.5-2, Table 5-1]:

Sr/Ca (mmol/mol) = -0.073 ± 0.006 SST + 11.09 ± 0.158. (r = -0.93: P < 0.01)

We established a regression line between IGOSS-SST and $\delta^{18}O_{coral}$, assuming that $\delta^{18}O_{coral}$ reflect only SST variations, with the same $\delta^{18}O_{coral}$ samples with Sr/Ca ratios, as follows:

$$\delta^{18}O_{coral} (‰_{VPDB}) = -0.108 \pm 0.014 \, SST – 1.486 \pm 0.36. \, (r = -0.86: P < 0.01)$$

The correlation coefficient between $\delta^{18}O_{coral}$ and Sr/Ca ratios was 0.84 (P < 0.01). The slope of the $\delta^{18}O_{coral}$ -SST regression (-0.108 $\pm$ 0.014 ‰$_{VPDB}$ /°C) was similar with that from the Gulf of Oman (-0.104 ‰$_{VPDB}$ /°C: Watanabe et al., 2017), which are too high to be consistent with published estimates. This suggests a significant contribution of $\delta^{18}O_{SW}$ to $\delta^{18}O_{coral}$.

$\delta^{18}O_{sw}$ were calculated by subtracting SST components (estimated from coral Sr/Ca ratios) from $\delta^{18}O_{coral}$ (Fig. 5-1), following the method proposed by Nurhati *et al.*,2011. The published regression slope of -0.18 $\pm$ 0.03 (‰/°C) [Gagan et al., 1998] was used to convert SST components of $\delta^{18}O_{coral}$ from Sr/Ca, and our slope of -0.044 mmol/mol/°C for estimation of SST components. Propagated error of $\delta^{18}O_{sw}$ was 0.08‰ following Nurhati et al., 2011. $\delta^{18}O_{sw}$ also showed seasonal-like cycle. The ranges of $\delta^{18}O_{sw}$ was from -0.53 to 0.42 (‰). For evaluations of the Arabian coral proxy, we comapared IGOSS-SST, mixed layer depth measured by Argo-float, cloudiness cover near the sample site and precipitations in northwestern India.

Coastal upwelling recorded in the Arabian Sea

To confirm general variations of the Arabian coral proxy, we calculated seasonal averaged variations of each proxy and in situ data (IGOSS-SST, mixed layer depth and cloudiness) [Fig.5-3]. Sr/Ca and $\delta^{18}O_{coral}$ increased (low SST) in summer. Although increase of Sr/Ca in summer was higher (cooler) than that in winter, $\delta^{18}O_{coral}$ in summer was similar with that in winter. $\delta^{18}O_{sw}$ decreased in summer in the same timing with increase of Sr/Ca and $\delta^{18}O_{coral}$ in summer. The lowest $\delta^{13}C_{coral}$ were confirmed after 2 months of $\delta^{18}O_{sw}$ reduction.

Reductions of $\delta^{18}O_{sw}$ in summer could record inflow of upwelled water with enriched $^{16}O_{sw}$ from deep sea (Fig.3-5). Reductions of $\delta^{18}O_{sw}$ in summer had two following possible mechanisms (1) inflow of low $\delta^{18}O_{sw}$ due to upwelling and/or (2) suppressed evaporation/much precipitations.

Depth profile of $\delta^{18}O_{sw}$ suggested that $^{16}O_{sw}$ were depleted (high $\delta^{18}O_{sw}$) on the sea surface in the Arabian sea [Fig.3-5]. Conversely, $^{16}O_{sw}$ were enriched in the deeper sea [Fig3-#: Sengupta et al., 2013]. $\delta^{18}O_{sw}$ could be reduced by active upwelling. We compared mixed layer depth at the

Arabian Sea (N18.5°, E59.5°) and $\delta^{18}O_{sw}$ to confirm the relationships of upwelling and $\delta^{18}O_{sw}$ (SST anomaly and $\delta^{18}O_{coral}$). $\delta^{18}O_{sw}$ were negatively correlated with mixed layer depth in summer Indian monsoon seasons (R = -0.51, p < 0.01: Fig.5-4). In addition, SST anomaly ($\delta^{18}O_{coral}$) were also negatively (positively) correlated with mixed layer depth in summer Indian monsoon seasons (vs. SST anomaly: R = -0.70, p < 0.01, $\delta^{18}O_{coral}$: R = 0.60, p < 0.01: Fig.5-4).

Reductions of $\delta^{18}O_{sw}$ in summer would cause upwelling driven by the summer Indian monsoon. Ekman transport off the Arabian Peninsula due to the strong summer Indian monsoon contributes to deepen a mixed-layer in summer [Prasad, 2004]. This Ekman transport causes upwelling in the Arabian Sea which brings enriched-$^{16}O_{sw}$ from deep sea.

$\delta^{18}O_{sw}$ were not correlated with mixed layer depth in entire seasons (R = -0.09, ns.: Fig.5-4). However, SST anomaly ($\delta^{18}O_{coral}$) were negatively (positively) correlated with mixed layer depth during the entire seasons (vs. SST anomaly: R = -0.55, p < 0.01 , $\delta^{18}O_{coral}$: R = 0.56, p < 0.01: Fig.5-4). SST proxies were correlated with mixed layer depth during whole seasons because mixed layer depth in the Arabian Sea deepen in both summer and winter [Goes et al., 2005]. Strong surface-heat loss due to winter monsoon also would deepen mixed layer in winter. Our coral SST proxy reflected deepen mixing driven by winter Indian monsoon. Our $\delta^{18}O_{sw}$ showed the characteristic differences of mixed-layer depth between in summer and in winter.

Cooling due to upwelling would suppress evaporation on the upwelling site. High (low) $\delta^{18}O_{sw}$ was resulted from active (less) evaporation [Delaygue et al., 2001]. Active upwelling with low $\delta^{18}O_{sw}$ seawater from deep sea decreased SST and suppressed evaporation (decrease $\delta^{18}O_{sw}$). Because $\delta^{18}O_{sw}$ was decreased by both less evaporation and active upwelling, upwelling reduced $\delta^{18}O_{sw}$ in summer.

Upwelling has a possibility to decrease $\delta^{13}C_{coral}$ (Felis et al., 1999, Watanabe et al., 2017). $\delta^{13}C_{coral}$ decreased 2 months later (October) than reduction of $\delta^{18}O_{sw}$ (August). This later reduction of $\delta^{13}C_{coral}$ would reflect (1) lower insolation (2) input lower $\delta^{13}C_{DIC-sw}$ (3) changes of autotrophy – heterotrophy.

In the Arabian Sea, cloudiness increased in summer (low insolation in summer, lowest peak: August). This reduction of insolation would contribute to negative excursions of $\delta^{13}C_{coral}$ in summer. The duration of negative $\delta^{13}C_{coral}$ excursion was longer than that of high cloudiness and negative peak of

$\delta^{13}C_{coral}$ was confirmed in October [fig.5-3]. This prolonged peak of $\delta^{13}C_{coral}$ might reflect upwelling in the Arabian Sea.

Upwelling in summer brings deep sea water with depleted $^{13}C_{DIC-sw}$ and high-nutrient. High nutrient is exhausted by the phytoplankton and this phytoplankton blooms decreased water column transparency. Supplying deep seawater with depleted $^{13}C_{DIC-sw}$ decreased $\delta^{13}C_{coral}$ [Kroopnick,1985]. Reduction of water-column transparency and heterotrophic feeding would continue reduction of $\delta^{13}C_{coral}$ [Watanabe et al., 2017, Felis et al., 1999,]. Reductions of $\delta^{18}O_{sw}$ and $\delta^{13}C_{coral}$ in summer suggested that summer records from the Arabian coral reflected coastal upwelling driven by summer Indian monsoon.

Comparison with previous $\delta^{18}O_{coral}$ profiles from the Arabian Sea.

We compared our $\delta^{18}O_{coral}$ with previous $\delta^{18}O_{coral}$ data from the southern coast of the Arabian Peninsula [Tudhope et al., 1996]. Our mean seasonal cycle of $\delta^{18}O_{coral}$ suggested that positive excursion of $\delta^{18}O_{coral}$ was same value with that in winter. However, previous mean seasonal cycle of $\delta^{18}O_{coral}$ in the Arabian Sea [Tudhope et al., 1996] suggested that positive excursion of $\delta^{18}O_{coral}$ in summer was much higher (cooler/more saline) than that in winter. Tudhope et al. (1996) concluded that winter $\delta^{18}O_{coral}$ variations were different from ship-based SST (IGOSS-SST on offshore) and reflected local SST in their coral habitat, not $\delta^{18}O_{sw}$. Tudhope et al., 1996 suggested that SST along the southern coast of the Arabian Peninsula would not decrease in winter by some coastal effect (less mixing and less evaporative cooling). Our coral collected from the Mashirah island where is located away from the Arabian Peninsula) would reflect mixing and winter SST decreasing which was driven by the winter Indian monsoon.

Seasonal variations of precipitation at northwestern India

Upwelling in the Arabian Sea driven by Indian monsoon could affect the amounts of precipitation in India [Izumo et al., 2008, Watanabe et al. in review, Chapter3]. We compared the coral records ($\delta^{18}O_{coral}$, Sr/Ca and $\delta^{18}O_{sw}$) in summer from the Arabian Sea with precipitations in the northwestern India (Fig.5-1: precipitation rate data provided from the India Meteorological Department) to know relationships of upwelling on variations of Indian precipitation. Precipitations in the northwestern India during wet seasons in India (May-Oct.) correlated with coral records (vs. Sr/Ca: -0.72, p < 0.01,

vs. $\delta^{18}O_{coral}$: 0.61, p < 0.01 and $\delta^{18}O_{sw}$: -0.57, p < 0.01: Fig.5-5) from the Mashira island.

The cycles of low SST an $\delta^{18}O_{sw}$ due to upwelling were coincide with wet seasons in the northwestern India, because summer Indian monsoon was drivers of both upwelling and precipitation in northwestern India [Goes et al., 2005]. Because coastal upwelling in summer directly influenced on the Arabian Sea (Mashirah island), seasonal variations of Indian monsoon would be reflected on coral records from the Arabian Sea.

Low-frequential variations of Arabian corals corals

SST_{anom} record in summer showed decreasing trend. $\delta^{18}O_{sw-anom}$ record in summer did not showed a trend-change. This suggested intensity of upwelling would change through the past 5 years. Intensity of upwelling in the Arabian Sea driven by summer Indian monsoon would be modulated by temperature gradient between Eurasian continent and Indian Ocean [Goes et al.,2005]. To investigate the relationship between upwelling in the Arabian Sea and temperature gradient, we compared the SST_{anom} ($\delta^{18}O_{sw-anom}$) record from the Arabian corals with the Eurasian snow cover and SST anomaly in the IOD index. SST anomaly positively correlated with minimum Eurasian snow cover in a year. This result suggested that warmer temperature on the Eurasian continent contribute higher SST (weak upwelling) in summer. However, $\delta^{18}O_{sw-anom}$ did not correlate with the minimum snow cover on the Eurasia. $\delta^{18}O_{sw-anom}$ in 2011 showed weakened signal of upwelling. $\delta^{18}O_{sw-anom}$ in 2010 and 2012 showed intensified upwelling. IOD index in western pole showed continuous cooling from 2010 to 2012, although SST in eastern IOD pole also decreasing and posi-IOD occurred in 2011. This cooling in western pole in 2010 and 2012 decoupling from IOD would induce intensified upwelling. Upwelling weakened in the posi-IOD year (2011). This suggested $\delta^{18}O_{sw-anom}$ and upwelling intensity would be more sensitive to SST variations in Indian Ocean than SST_{anom} in the Arabian Sea.

Changes of upwelling-intensities would affect on the Indian precipitation [Izumo et al., 2008]. SST_{anom} in summer from the Arabian coral correlated with the maximum precipitation in northwestern India (SST_{anom} vs. precipitation rate in the northwestern India: r = 0.72, P < 0.1, $\delta^{18}O_{sw-anom}$ vs. precipitation rate in the northwestern India: r = 0.59, P = 0.21, Fig. 5-6).

The correlation analysis between the Arabian coral record in summer and precipitation in the northwestern India suggested that the amounts of precipitation in the northwestern India would be

controlled by activity of evaporation in the Arabian Sea. The Arabian Sea is a source of the moisture for summer precipitation in northwestern India via summer Indian monsoon [Izumo et al., 2008]. Evaporation was suppressed by the strong upwelling and less moisture transported to the northwestern India, even if the summer Indian monsoon intensified. Intensified Indian monsoon would decrease precipitations in summer on the northwestern India [Izumo et al., 2008].

We evaluated influence of upwelling in the Arabian Sea on the precipitation in the northwestern India using longer coral records (26 years) from the Gulf of Oman. The Gulf of Oman would be less sensitive to the Arabian upwelling than the Arabian Sea, because the upwelling signals in the Gulf of Oman were weaker than the Arabian Sea [Chapter 3]. In the Omani coral, 3-year moving averages of June to August SST_{anom} and $\delta^{18}O_{sw-anom}$ (Fig. 3-6) also show a positive correlation with the 3-year moving averages of maximum precipitation rate in northwestern India (SST_{anom} vs. precipitation rate in the northwestern India: r = 0.53, P < 0.01, $\delta^{18}O_{sw-anom}$ vs. precipitation rate in the northwestern India: r = 0.71, P < 0.01: see chapter 3, Fig. 3-6). These were similar results with the Arabian coral.

Statistical analysis of seasonal variations in Arabian coral suggested that the summer Indian monsoon was the transported way of moisture to the northwestern India. Summer records from both Arabian and Omani corals suggested that amounts of transported moisture were controlled precipitations in the northwestern India. Intensified upwelling which was induced by strong summer Indian monsoon suppressed evaporation in the Arabian Sea and decreased precipitations the northwestern India.

5-4 Reconstruction of summer Indian monsoon and upwelling using the Arabian fossil corals

SST reconstruction in the Arabian Sea during the last millennium

10-5 years annual cycles were confirmed in Sr/Ca and $\delta^{18}O_{coral}$ from the Arabian corals. Averaged values and seasonal range of Sr/Ca, $\delta^{18}O_{coral}$ and $\delta^{18}O_{sw}$ were shown on table5-2. Based on averaged Sr/Ca in fossil corals and slopes of SST-Sr/Ca regression in the modern Arabian coral, we estimated SST variations relative to the present (present: CE2014-2009) through the last millennium. SST in late-LIA was -2.66 cooler than the present and SST in mid-LIA was -3.24 cooler than the present. SST in the global warming trend was 0.72 cooler than the present. Warming trend in the Arabian sea from 1960 to 2014 was 0.15°C/decade. Extended reconstruct SST (ERSST) dataset revealed warming trend

from 1960 to 2014 was 0.20 ± 0.02 ℃/decade in the Arabian Sea. This ERSST data was consistent with the modern and fossil coral records.

These absolute SST reconstructions based on Sr/Ca from the Arabian Sea suggested that our fossil corals from the Arabian Sea experienced the MWP, LIA and recent global warming. However absolute SST in the LIA in the Arabian Sea was much cooler than reconstructed SST based on continuous coral cores from other sample sites (SST difference between 2000-1950 and 1850-1750 in the Pacific: 0.3℃, in the Indian Ocean: 0.7℃: Tierny et al., 2015). Because it has a possibility that intercept of Sr/Ca-SST regression was different among coral colonies [Correge, 2006], we need to improve accurate estimations of absolute-SST using fossil corals. We used anomalies of coral proxies relative to the averaged value in each fossil corals to overcome possibility of differences in intercepts among coral colonies. Anomalies of SST and $\delta^{18}O_{sw}$ in the Arabian fossil and modern corals were calculated relative to winter value in each fossil coral (SST anomaly and $\delta^{18}O_{sw\text{-anom}}$).

Upwelling and summer Indian monsoon intensities in the Arabian Sea during the last millennium

According to a calibration work using the modern coral from the Arabian Sea, summer Indian monsoon and coastal upwelling in the Arabian Sea affected on summer SST proxies and $\delta^{18}O_{sw}$ from the Arabian corals. To show the intensity of upwelling in each age, mean seasonal cycles were estimated from SST anomaly and $\delta^{18}O_{sw\text{-anom}}$ in each ages. We applied a *t*-test to detect statistically significant differences of the biweekly mean values of SST anomaly and $\delta^{18}O_{sw\text{-anom}}$ between the modern and each fossil coral.

Lowest SST in summer of mid- and late- LIA were -2.91±0.23 and -1.91±0.21 ℃. Lowest SST in summer of present was -2.05±0.40 ℃. Summer SST anomaly in of mid- and late-LIA were not significantly differences from the present. Lowest $\delta^{18}O_{sw\text{-anom}}$ in summer of mid- and late- LIA were -0.29±0.13 (early June) and -0.41±0.07 ℃ (early August). Lowest $\delta^{18}O_{sw\text{-anom}}$ in summer of present was -0.28±0.06 ℃ (late August). Summer $\delta^{18}O_{sw\text{-anom}}$ in mid- and late- LIA were lower than the present. In addition, the timing of the lowest of $\delta^{18}O_{sw\text{-anom}}$ in mid-LIA was earlier than the present. Significantly lower $\delta^{18}O_{sw}$ in summer of LIA than the present suggested that intensified upwelling and/or less evaporation due to cooling in the LIA on the Arabian Sea.

Influence of upwelling in the Arabian Sea on the Indian precipitations

Less evaporation in the LIA would decrease precipitations in the northwestern India. Less evaporation due to the weaken upwelling transported less moisture to the northwestern India via summer Indian monsoon. Precipitation at the northwestern India decreased by less humid transportations from the Arabian Sea in the LIA. Less evaporation in the Arabian sea would contribute the retreat of intertropical convergence zone in the LIA. Previous studies suggested weak monsoon (eg. Asian and Caribbean monsoon) contributed to retreat the northern limit of intertropical convergence zone in the LIA [Hon et al., 2015, Fleitmann et al., 2007]. Our results suggested in the northern Indian Ocean, the northern limit of intertropical convergence zone would retreat due to less evaporation in the Arabian Sea, not weaken summer Indian monsoon in LIA.

Durations of upwelling in the Arabian Sea and wet seasons in the northwestern India

The duration of $\delta^{18}O_{sw}$ reduction in mid-LIA was shorter than the present and timing of lowest $\delta^{18}O_{sw}$ came earlier than that of the present. This suggested that strong upwelling driven by summer Indian monsoon became shorter in the mid-LIA than the present. This shorter with less evaporation in the Arabian Sea in the mid-LIA would induce the shorter and weaker wet season in northwest India than the present. The shorter wet seasons should have an impact on the society and agriculture in the India in the mid-LIA.

Comparisons of histories of Indian empire and the Arabian coral records.

In the last 500 years, humans recorded past climate events and social incidents on their historical documents [Air temp]. Coral records could be compared with these documents, for revealing causes of their historical climate changes and incidents. The Mughal Empire documented that 11 severe droughts occurred per 25 years from 1625 to 1649. After frequent severe drought from 1625 to 1649, drought in India occurred 10 drought years per 50 years until 1700. This period of stable drought occurrences in India corresponded with the prosperity of Mughal Empire. After stable period, the Mughal Empire start to decline.

We compared our Arabian coral records in LIAs with historical documents. Pre-prosperity era (1625-1649) when frequent drought occurred corresponded era with shorter-term of upwelling than the present. This short-term upwelling seasons in mid LIA could contribute to drought in India and prevent

prosperity in the Mughal Empire. However, it is still un

Our Arabian coral records concluded that evaporations in summer of the LIA would weaken relative to the present. However, in the mid LIA, durations of this upwelling were shorter than other-era. This shorter upwelling in LIA would make wet-seasons shorter.

References

1. Schott, F. A. & McCreary, J. P. The monsoon circulation of the Indian Ocean. *Prog. Oceanogr.* **51,** 1–123 (2001).

2. Krishna Kumar, K., Rupa Kumar, K., Ashrit, R. G., Deshpande, N. R. & Hansen, J. W. Climate impacts on Indian agriculture. *Int. J. Climatol.* **24,** 1375–1393 (2004).

3. Brock, J. C., McClain, C. R., Luther, M. E. & Hay, W. W. The phytoplankton bloom in the northwestern Arabian Sea during the southwest monsoon of 1979. *J. Geophys. Res.* **96,** 20623 (1991).

4. Qasim, S. Z. Oceanography of the northern Arabian Sea. *Deep Sea Res. Part A. Oceanogr. Res. Pap.* **29,** 1041–1068 (1982).

5. Tudhope, A. W., Lea, D. W., Shimmield, G. B., Chilcott, C. P. & Head, S. Monsoon Climate and Arabian Sea Coastal Upwelling Recorded in Massive Corals from Southern Oman. *Palaios* **11,** 347 (1996).

6. Fleitmann, D. *et al.* Holocene ITCZ and Indian monsoon dynamics recorded in stalagmites from Oman and Yemen (Socotra). *Quat. Sci. Rev.* **26,** 170–188 (2007).

7. Abram, N. J., Gagan, M. K., Cole, J. E., Hantoro, W. S. & Mudelsee, M. Recent intensification of tropical climate variability in the Indian Ocean. **1,** 849–853 (2008).

8. Nakamura, N. *et al.* Mode shift in the Indian Ocean climate under global warming stress. **36,** 3–7 (2009).

9. England, M. H. *et al.* Recent intensification of wind-driven circulation in the Pacific and the ongoing warming hiatus. *Nat. Clim. Chang.* **4,** 222–227 (2014).

10. Abram, N. J. *et al.* Early onset of industrial-era warming across the oceans and continents. *Nature* **536,** 411–418 (2016).

11. Lean, J., Beer, J. & Bradley, R. Reconstruction of solar irradiance since 1610: Implications for climate change. *Geophys. Res. Lett.* **22,** 3195–3198 (1995).

12. Mann, M. E. *et al.* Global Signatures and Dynamical Origins of the Little Ice Age and Medieval Climate Anomaly. *Science (80-.).* **326,** 1256–1260 (2009).

13. Graham, N. E., Ammann, C. M., Fleitmann, D., Cobb, K. M. & Luterbacher, J. Support for global climate reorganization during the "Medieval Climate Anomaly". *Clim. Dyn.* **37,** 1217–1245 (2011).

14. Gupta, A. K., Anderson, D. M. & Overpeck, J. T. Abrupt changes in the Asian southwest monsoon during the Holocene and their links to the North Atlantic Ocean. **421,** 4–7 (2003).

15. Fleitmann, D. Holocene Forcing of the Indian Monsoon Recorded in a Stalagmite from Southern Oman. *Science (80-.).* **300,** 1737–1739 (2003).

16. Wang, Y. *et al.* The Holocene Asian Monsoon : Links to Solar Changes and North Atlantic Climate. **2002,** 854–858 (2005).

17. Lechleitner, F. A. *et al.* Tropical rainfall over the last two millennia: evidence for a low-latitude hydrologic seesaw. *Sci. Rep.* **7,** 45809 (2017).

18. Gagan, M. K. Temperature and Surface-Ocean Water Balance of the Mid-Holocene Tropical Western Pacific. *Science (80-.).* **279,** 1014–1018 (1998).

19. Nurhati, I. S., Cobb, K. M. & Di Lorenzo, E. Decadal-Scale SST and Salinity Variations in the Central Tropical Pacific: Signatures of Natural and Anthropogenic Climate Change. *J. Clim.* **24,** 3294–3308 (2011).

20. Sengupta, S., Parekh, A., Chakraborty, S., Kumar, K. R. & Bose, T. Vertical variation of oxygen isotope in Bay of Bengal and its relationships with water masses. **118,** 6411–6424 (2013).

21. Goes, J. I., Thoppil, P. G., Gomes, H. R. & Fasullo, J. T. Warming of the Eurasian Landmass Is Making the Arabian Sea More Productive. *Science (80-.).* **308,** 545–547 (2005).

22. Felis, T., Pätzold, J., Loya, Y. & Wefer, G. Vertical water mass mixing and plankton blooms recorded in skeletal stable carbon isotopes of a Red Sea coral. *J. Geophys. Res. Ocean.* **103,** 30731–30739 (1998).

23. Watanabe, T. K. *et al.* Past summer upwelling events in the Gulf of Oman derived from a coral geochemical record. *Sci. Rep.* **7,** 4568 (2017).

24. YAMAZAKI, A. *et al.* Reconstructing palaeoenvironments of temperate regions based on high latitude corals at Tatsukushi Bay in Japan. *J. Japanese Coral Reef Soc.* **11,** 91–107 (2009).

25. Corrège, T. Sea surface temperature and salinity reconstruction from coral geochemical tracers. *Palaeogeogr. Palaeoclimatol. Palaeoecol.* **232,** 408–428 (2006).

26. Izumo, T. *et al.* The Role of the Western Arabian Sea Upwelling in Indian Monsoon Rainfall Variability. *J. Clim.* **21,** 5603–5623 (2008).

27. Qasim, S. Z. Oceanography of the northern Arabian Sea. *Deep Sea Res. Part A. Oceanogr. Res. Pap.* **29,** 1041–1068 (1982).

28. Yan, H. *et al.* Dynamics of the intertropical convergence zone over the western Pacific during the Little Ice Age. *Nat. Geosci.* **8,** 315–320 (2015).

29. Kroopnick, P. M. The distribution of ^{13}C of ΣCO_2 in the world oceans. Deep Sea Res. Part A. *Oceanogr. Res. Pap.* **32**, 57–84 (1985).

30. Delaygue, G. *et al.* Oxygen isotope/salinity relationship in the northern Indian Ocean. *J. Geophys. Res. Ocean.*, *106*, 4565-4574 (2001).

Reference	Slope (‰/°C)	Species	Locality
This study	-0.10	*Porites.sp*	Arabian Sea
This study (Watanabe et al 2017)	-0.10	*Porites.sp*	The Gulf of Oman
Quinn et al. (1996)	-0.19	*Porites lutea*	New Caledonia
Watanabe et al. in print	-0.16	*Porites.sp*	Red Sea
Pfeiffer et al. (2004)	-0.21	*Porites.sp*	La Reunion
Zinke et al. (2004)	-0.19	*Porites lobata*	Myotte
Cahyarini et al. (2009)	-0.10	*Porites.sp*	Timor

Table 5-1

Temperature dependency of $\delta^{18}O$ in coral skeletons.

Reference	Slope (mmol×mol^{-1}/°C)	Species	Locality
This study	-0.067	*Porites.sp*	Arabian Sea
This study (Watanabe et al 2017)	-0.044	*Porites.sp*	The Gulf of Oman
Gagan et al. (1998)	-0.064	*Porites lutea*	Great Barrier Reef
Marshall and MuCulloch (2001)	-0.059	*Porites.sp*	Xmas Island
Zinke et al. (2004)	-0.05	*Porites lobata*	Myotte
Felis et al. (2004)	-0.06	*Porites.sp*	Red Sea
Cahyarini et al. (2009)	-0.04	*Porites.sp*	Timor
Sagar et al. (2016)	-0.073	*Porites lutea*	Arabian Sea

Table 5-2

Temperature dependency of the Sr/Ca ratio in coral skeletons.

Sample	U-Th age		Sr/Ca (yrs) *	$\delta^{18}O_{coral}$ (yrs) *
OMN2015	2015, March		6	6
S12C02	1965	±20	6	6
S12C03	1746	±5	10	5
S12C00	1624	±33	10	4
S12C01	1167	±3	10	10

Table 5-3

Sample nformation of modern and fossil corals from the Mashira island.

*Sr/Ca and $\delta^{18}O_{coral}$ show number of years which are measured

Sample	Sr/Ca			$\delta^{18}O_{coral}$			$\delta^{13}C_{corall}$		
	Ave.		Range	Ave.		Range	Ave.		Range
OMN2015	9.33	±0.11	0.50	-4.35	±0.27	1.14	-2.17	±0.47	2.14
S12C02	9.39	±0.10	0.48	-3.78	±0.33	1.76	-3.11	±0.85	3.90
S12C03	9.55	±0.09	0.50	-4.00	±0.29	1.52	-1.32	±0.49	2.58
S12C00	9.59	±0.12	0.63	-3.90	±0.38	1.71	-1.32	±0.53	3.01
S12C01	9.38	±0.14	0.63	-4.04	±0.33	1.54	-1.45	±0.89	4.74

Table 5-4

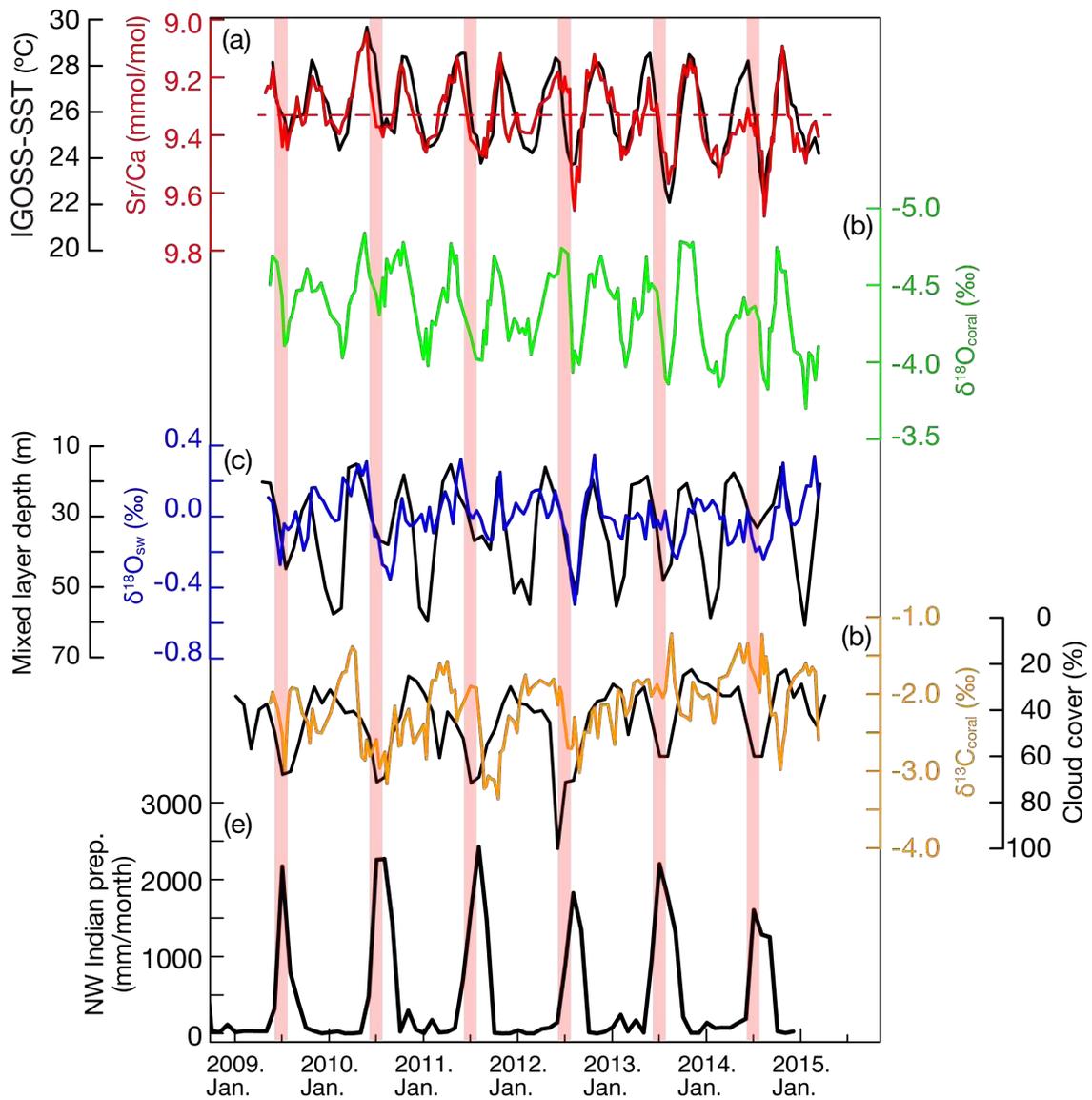Analytical results of modern and fossil corals from the Mashira island.

Fig.5-1

Analytical results of the Arabian coral and in-situ data.

(a) Red and Black lines: Sr/Ca and IGOSS-SST Dot line showed average value of Sr/Ca

(b) green line: $\delta^{18}O_{coral.}$

(c) Blue and black lines: $\delta^{18}O_{sw}$ and mixed layer depth based on Argo float.

(d) Orange and black lines: $\delta^{13}C_{coral}$ and cloud cover.
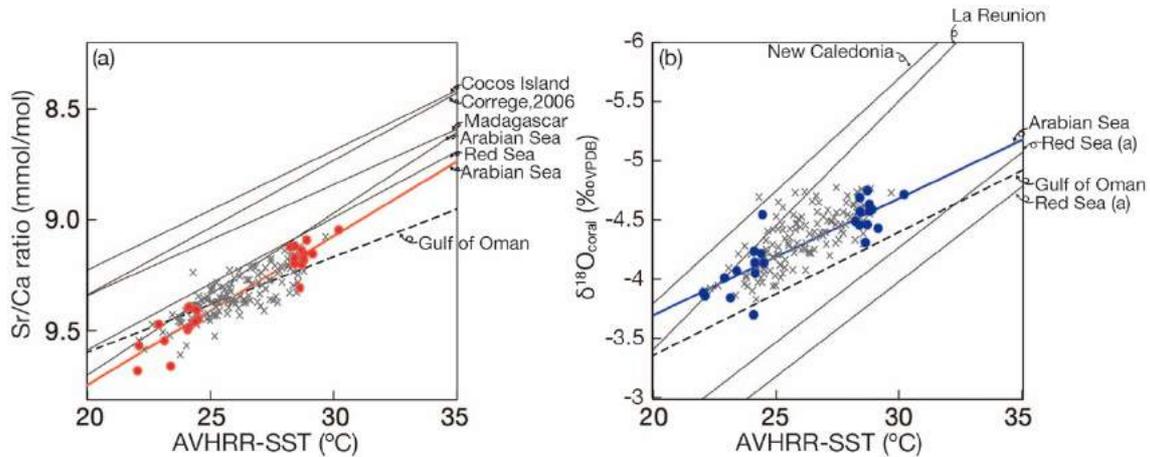
(e) Black line showed northwestern Indian precipitation.

Fig.5-2

Calibration of the Sr/Ca ratio and $\delta^{18}O_{coral}$ thermometer (a and b). Circle-dots indicate the seasonal maxima and minima of the Sr/Ca ($\delta^{18}O_{coral}$), which are tied with the maxima and minima of SST, respectively (purple dots: minima of SST; green dots: maxima of SST). Cross-dots show the data points between all data points of Sr/Ca ratio ($\delta^{18}O_{coral}$).

(a) Red line shows Sr/Ca-SST calibration line from the Arabian coral. The gray lines indicate the previous published Sr/Ca-SST calibration lines (TableS1). Dot line showed Sr/Ca-SST calibration line from our Omani coral [Watanabe et al., 2017]

(b) Red line shows $\delta^{18}O_{coral}$-SST calibration line from the Arabian coral. The gray lines indicate the previous published $\delta^{18}O_{coral}$-SST calibration line (TableS2). Dot line showed $\delta^{18}O_{coral}$ -SST calibration line from our Omani coral [Watanabe et al., 2017] The slope of $\delta^{18}O_{coral}$-SST calibration line using both summer and winter peaks in our Omani coral is similar to $\delta^{18}O_{coral}$ -SST slope from and the Oman.
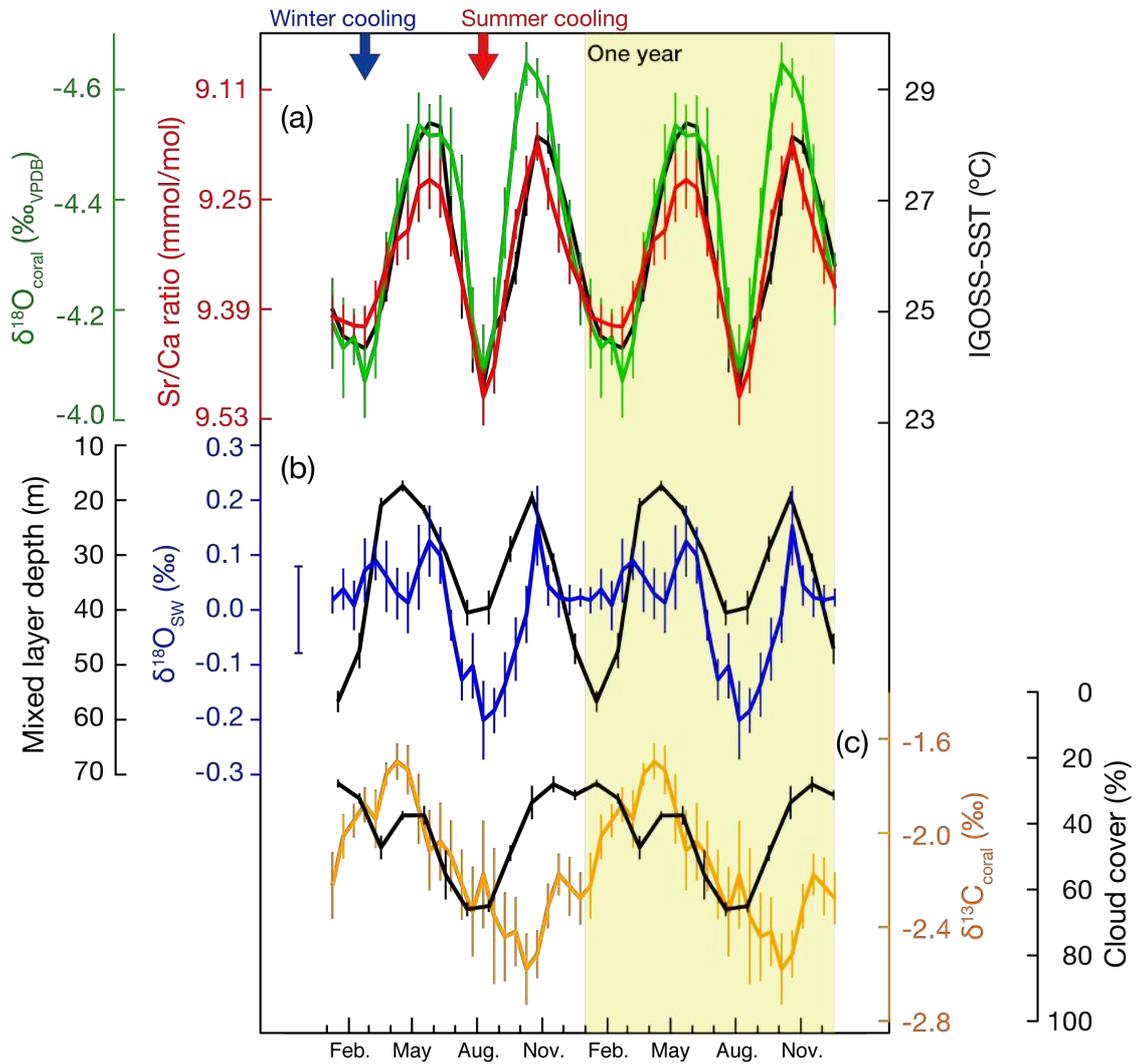
Fig.5-3

Mean seasonal cycle of the Arabian coral records and in-situ records (Seasonal cycle from January to December is repeated: highlighted in yellow).

Red, green and Black lines: Sr/Ca, $\delta^{18}O_{coral.}$ and IGOSS-SST

Blue and black lines: $\delta^{18}O_{sw}$ and mixed layer depth based on Argo float. The error bar showed estimation error of $\delta^{18}O_{sw}$.

Orange and black lines: $\delta^{13}C_{coral}$ and cloud cover.
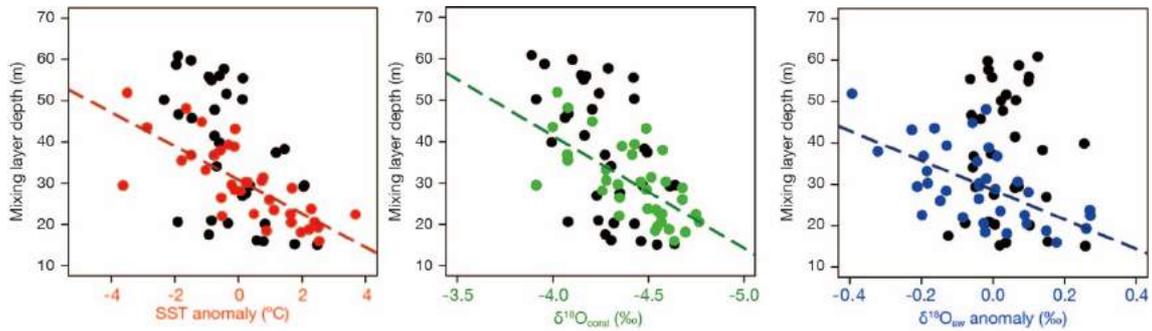
Figure5-4

Scatterplot of the Arabian coral records vs. mixed-layer depth based on Argo float in the Arabian Sea. Color and black dots showed data during summer (summer Indian monsoon) seasons and another season, respectively. The Arabian coral data and mixed layer depth showed significant correlations in summer.
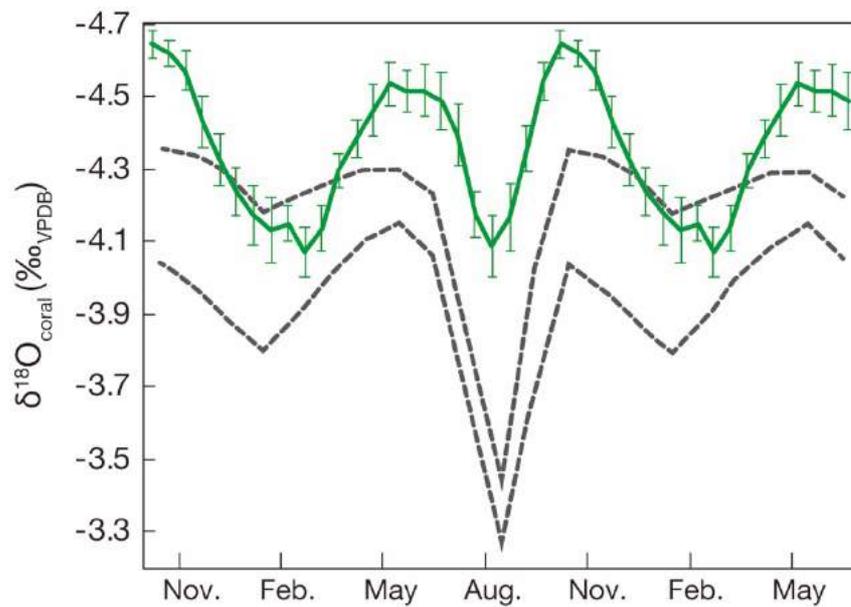

Figure5-5

Comparison of mean seasonal $\delta^{18}O_{coral}$ cycles between our Arabian coral (green line) and profiles published in Tudhope et al., 1996 (gray dot lines).
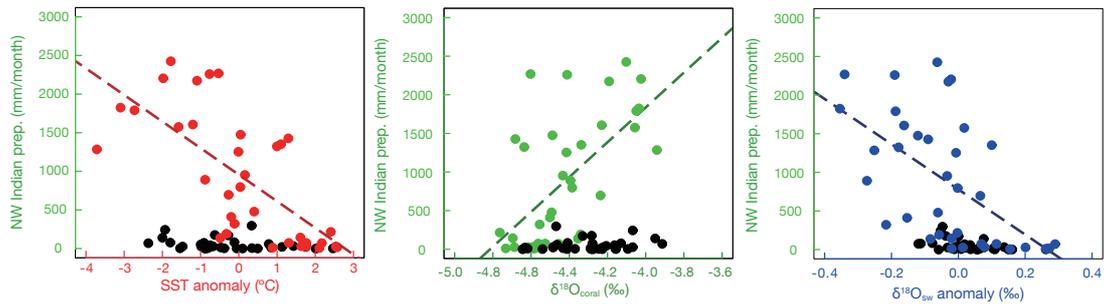
Figure 5-6

Scatterplot of the Arabian coral records vs. precipitations in the northwestern India. Color and black dots showed data during summer (summer Indian monsoon) seasons and another season, respectively. The Arabian coral data and precipitations showed significant correlations in summer.
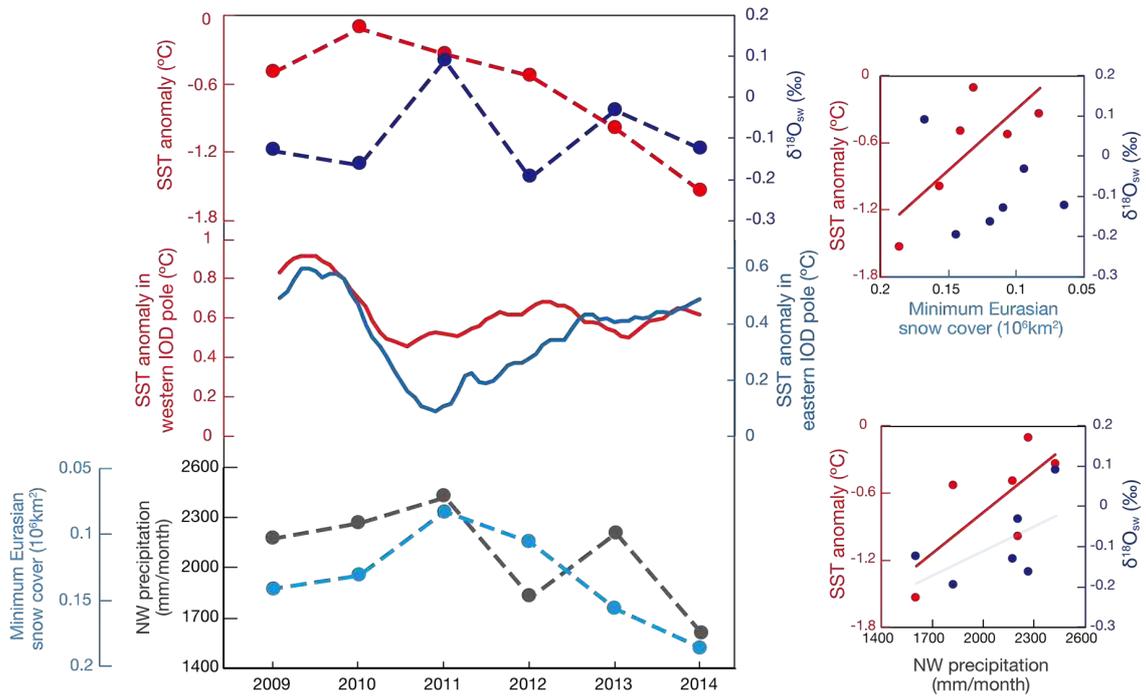
Figure 5-7

Left panel: Comparison among the Arabian coral in summer (red: SST anomaly, blue: d18Osw), SST anomaly in the western IOD region (black), minimum Eurasian snow cover (blue) and maximum precipitations in northwestern India.

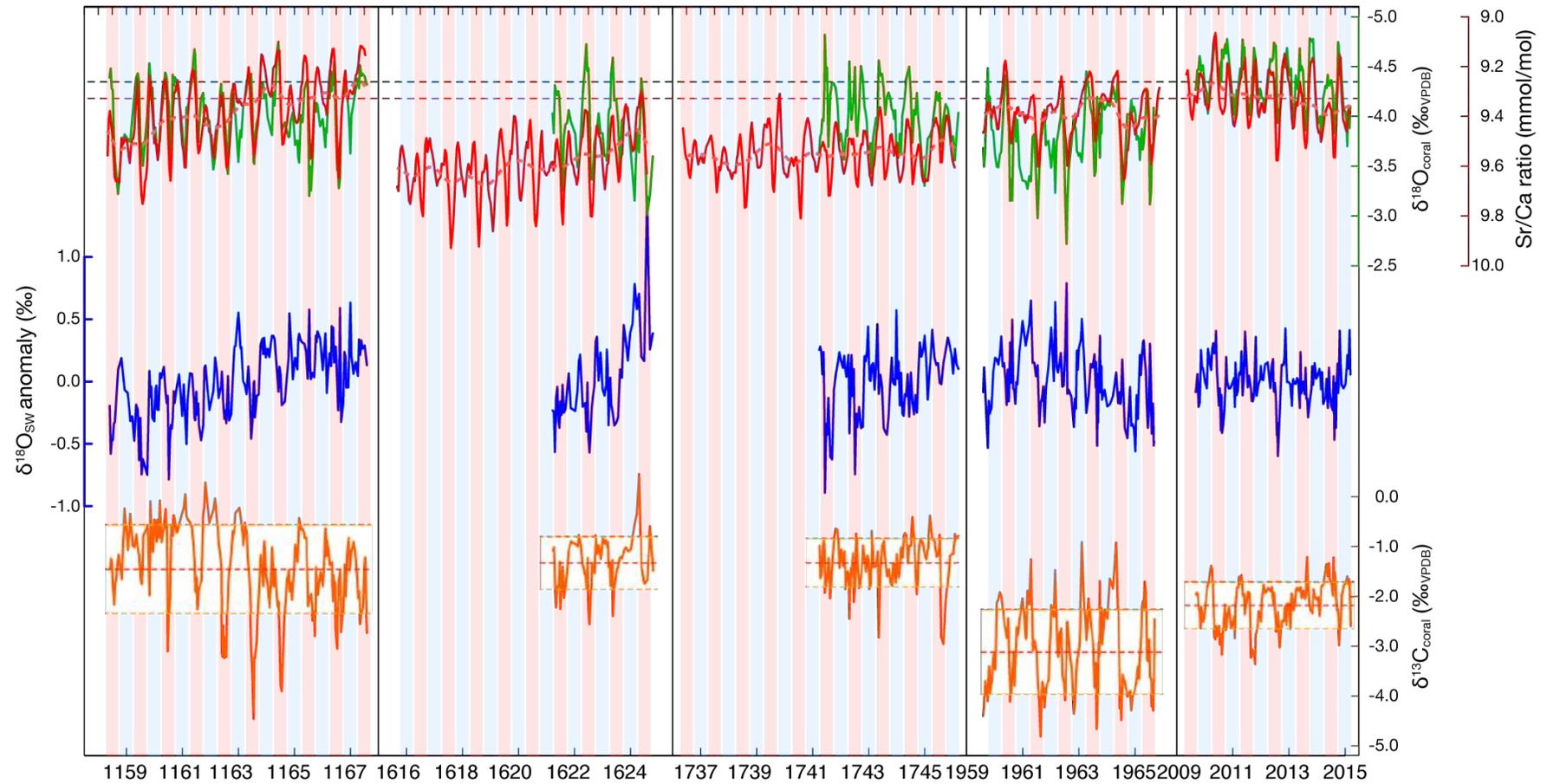Right panel: Scatterplot of summer coral records vs. Eurasian snow cover and vs. northwestern Indian precipitations.

Fig.5-9

Results of geochemical analysis from modern and fossil Arabian corals.

Sr/Ca (red color), $\delta^{18}O_{coral}$ (green color), $\delta^{18}O_{sw-anom}$ (blue color) and $\delta^{13}C_{coral}$ (orange color). Dot line indicated averaged values of each proxies from the modern coral. Red and blue bar showed summer and winter seasons, respectively.
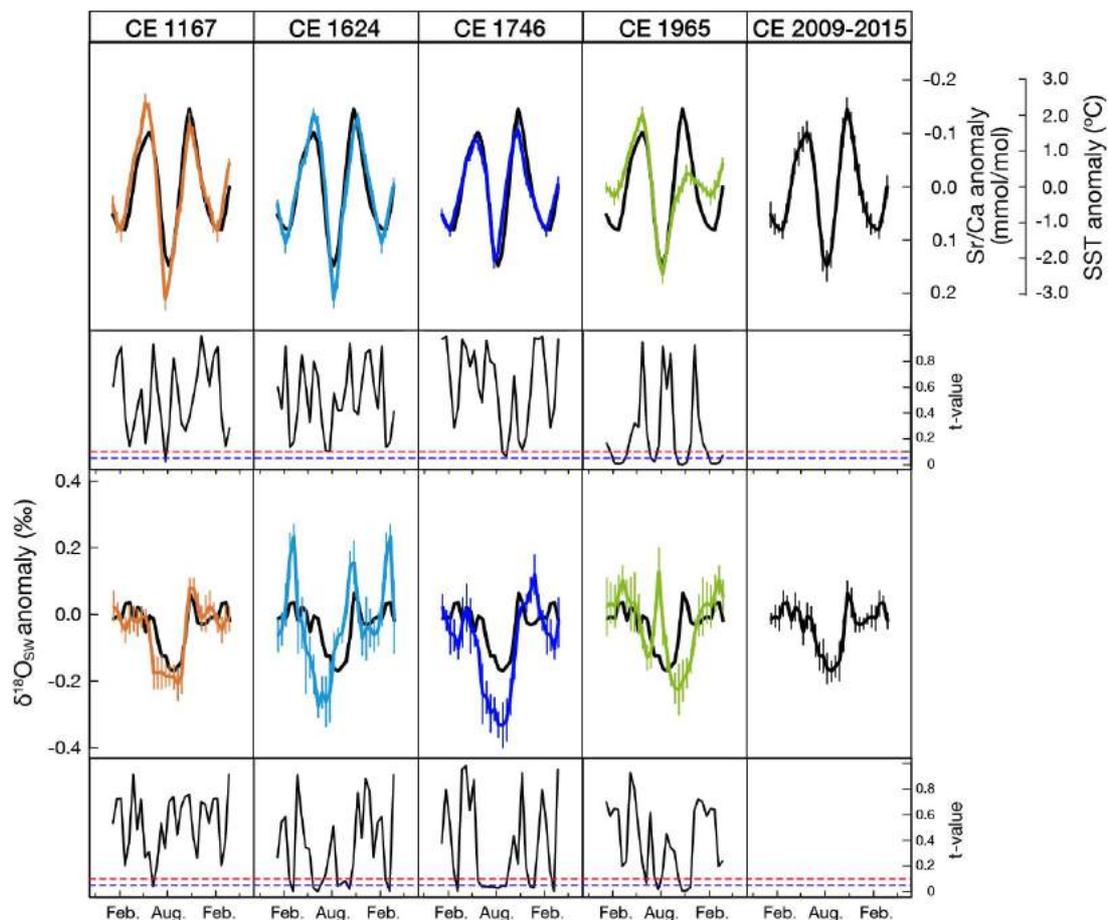
Fig.5-10

Mean seasonal variations of Sr/Ca (SST anomaly) and $\delta^{18}O_{sw-anom}$ from modern (black lines) and fossil (colored lines) Arabian corals. Anomalies were calculated based from winter value of Sr/Ca and $\delta^{18}O_{sw-anom}$ in each sample. We showed t-value of Sr/Ca ($\delta^{18}O_{sw-anom}$) between the modern and each fossil corals to confirm significances of seasonal variations between in the modern and fossil corals. 95% and 90% confidence interval were shown using blue and red dot line, respectively.
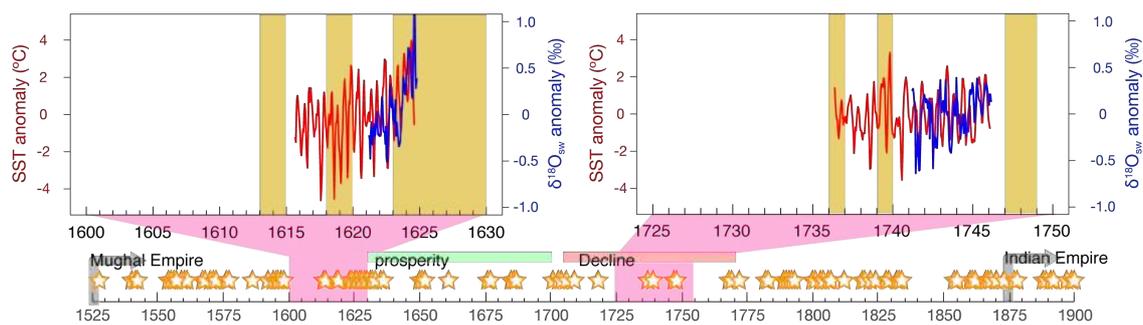
Comparison of historical drought and the Arabian coral records in the LIAs.

Orange colored year and orange stars indicate historical drought years.

6. Fossil coral records revealed the relationships between monsoon variability and ancient civilizations

Abstract

India and Mesopotamia civilization occurred with the agricultural development utilizing the winter rainfall and river water in the fertile crescent between the Indus and Tigris-Euphrates Rivers. Indus civilizations matured in 4.6 thousand years before the present (kyrBP, present day: 1950) and start to decline around 4.2 kyrBP. The Akkad empire was established in the Mesopotamia regions around 4.6 kyrBP, but abruptly collapsed in 4.2±0.2kyrBP. There was not revealed these climatic states in the era of transitions/collapse. Here, we present biweekly resolved coral records from 6 fossil corals of different time-windows from the present and 3.1 to 4.3 kyrBP using the Omani modern and fossil corals.

Summer SST and d18Osw gradually decreased from 4.3 to 3.5 kyrBP. This suggested summer Indian monsoon intensified. The gradual intensification of summer Indian monsoon would affect on Indian civilization. Indian civilization could move their center of civilization as a response of gradual climate changes in wet seasons.

Winter SST and d18Osw abruptly decreased in 4.2kyrBP. At the present, strong winter monsoon transporting cold and dry air with dust cause agricultural failures and social unrests in Syria and Iraq. This result suggested that decreasing of SST and d18Osw in winter was generated by frequent Shamal in winter. This frequent winter Shamal made difficult to keep their agricultural systems and increased the social unrest in the Mesopotamia region. Our result suggested that the Akkad empire collapse would have been triggered by the agricultural failure and the social unrest in the Mesopotamia region caused by the prolonged duration of intensified winter monsoon.

6-1 Introduction

Indus civilization

Indus civilization was developed at the Indus valley along the Indus river from 4.6kyBP. Indus valley were located on northwestern India where summer Indian monsoon affected [Chapter 3]. Indus civilians engaged in agriculture utilizing river water with flood and rainwater. However, civilization in the Indus valley started to well development from 5.5 kyrBP, this civilization disappeared in 3.9kyrBP. In 4.6-5.3 kyrBP, civilization in the Indus valley were in "regionalization era" (early Harappan phase). From 4.6yBP, "integration era" (mature Harappan phase) started until 3.9 yrBP. The integration era was so called Indus civilization. In integration era, Indus civilization had highly developed cites around the Mohenjo-Daro in Indus valley (Fig. 6-1). From 3.9 kyrBP, mature Indus civilization transformed to "post-urbanization era" (late Harappan) accompanied by a migration from the Indus valley (northwestern India) to northcentral site (in the present: near to New Delhi).

Mesopotamia civilization

The Mesopotamia civilization started in "the fertile crescent" and engaged in rainfed- and irrigated-agriculture utilizing water from winter rainfall and Tigris-Euphrates rivers [Wilkinson et al.,1994, Jacobsen and Adams, 1958]. Blessed from agricultural products, the first united empire in the Mesopotamia region, named as "Akkad empire", was established around the metropolis "Tell-Lilan" under the rule of Sargon of Akkad in *ca.* 4.6 kyrBP [Fig. 6-1: Weiss et al., 1993, Cullen et al., 2000]. Archeological ruins which were dated by radiocarbon isotopes revealed that the Akkad empire abruptly collapsed and citizens in this empire disappeared around 4.2 kyrBP. [Weiss et al., 1993, Weiss et al., 2004]. After 300 years of this collapse, other populations resettled in a region where Akkad empire settled.

Collapse of ancient civilizations

Abrupt transitions of ancient civilizations were remarked by both archeologists and paleo-climatologists, because the reason of these transitions was still unknown and might be related to the climate changes in 4.2 kyrBP. Soil morphology at Tell-Leilan and sediment core from the Gulf of Oman suggested that the collapse of Akkad empire might have been caused by the abrupt drought related to the strong wind from the western Asia in 4.2 kyrBP [Weiss et al., 1993, Cullen et al., 2000]. Sediment cores from the Arabian Sea suggested that the Indus and Mesopotamia civilizations transited to next phases due to weak Indian monsoon. However, the speleothem from the central India revealed the Indus civilization would be over due to intensified Indian monsoon. In the same timing with the collapse, the aridification/humid events were recorded in speleothems and sediment cores from Asia and Africa. However, these climatic signals in 4.2 kyrBP were deferent among proxies [Fig.1: Weiss et al., 1993, Cullen et al., 2000, Walker

et al., 2012, Staubwasser et al., 2003, Kathayat et al., 2017].

Seasonal variations of aridity should be known for revealing changes of civilian lifestyle in Mesopotamian and Indus valley regions, because they had been engaged in agriculture utilizing the seasonal-variable rainfall and river-discharge. An important climate factor to consider the seasonal aridity changes was the intensity of monsoon. Summer Indian monsoon and winter monsoon induce wet seasons (boreal summer) in India and western Asia respectively. To separately reconstruct precipitations in each wet season in Indus and Mesopotamia civilizations, we used 6 fossil corals around 4.2 kyrBP from the Holocene reef terrace in the northeastern coast of the Arabian Peninsula [Fig.1]. The northeastern coast of the Arabian Peninsula was under the influences of monsoon systems and the Mediterranean rainfall belt through the Holocene epoch [Cullen et al., 2000, Fleitmann et al., 2007].

6-2. Samples and statistical procedures.

Modern and fossil corals from the Oman

On this chapter, we used one modern and 6 fossil corals from the Gulf of Oman and the Holocene reef terrace in the northeastern coast of the Arabian Peninsula (Fig. 6-1). We screened diagenesis and selected well preserved fossil samples using scanning electron microscope (SEM) and X-ray diffractions (XRD) analysis. The XRD analysis and SEM observations were performed for all fossil samples to check alternation of the microstructure of coral skeletons. The ages of fossil corals were determined using radiocarbon dating at Accelerated Mass Spectrometry Center of Yamagata University. The ages were calculated using the Marine13 [Reimer et al., 2013]. The age results were corrected the local reservoir effect following the Cullen et al. (2000). We used Sr/Ca, $\delta^{18}O_{coral}$, $\delta^{18}O_{sw\text{-}anom}$ from the modern and fossil corals. The fossil coral records were converted to anomaly value relative to average of each sample. For comparison modern coral records in winter, we used in situ data in the Gulf of Oman (Port Sultan Qaboos), wheat cultivations in Syria and Iraq, and numbers of refugees in Iraq and Syria. We also used area of archeological sites around Tel-Leillan.

6-3. Impact of monsoon variations on the society in the present

Influence of summer monsoon variability on the Indian agriculture

Precipitations in India which are brought by summer Indian monsoon has an important hydrological source for maintaining agriculture and society in India [Kumar et al., 2004]. Interannual variability of precipitations in India would affect the amount of crop yields in India (main products in northwestern India: wheat).

To show the influence of Indian monsoon on the agriculture in India, we compared the variations of wheat-yielding with averaged coral records during summer in the Gulf of Oman. 3yearrs moving averaged SSTa and $\delta^{18}O_{sw\text{-}anom}$ were positively correlated with variations of wheat-yielding in India with 3 years lag (Fig. 6-2: vs. SSTanom, R =

0.67, $P < 0.05$, vs. $\delta^{18}O_{sw-anom}$ $R = 0.68$, $P < 0.05$). This result suggested less precipitation decreased amounts of wheat in India.

Influence of winter Shamal on the western Asian society

Local climate events dominate on the Arabian Peninsula and the western Asia because winter monsoon was weaker on this region than summer monsoon. Winter Shamal (local and short term event) is key climate event to consider the seasonal aridity changes in the western Asia (Fig.6-3, Perrone, 1979). Shamal also occur during both summer and winter with different characteristics between these two seasons like monsoon [Perrone, 1979]. Durations of winter Shamal have shorter (within 5 days) than summer Shamal [Fig.6-3: Rao et al., 2003]. Because winter Shamal disturb weather conditions and transports cold and dry air with dust, winter Shamal have more impact on both society and weathers in the western Asia than summer Shamal [Notaro et al., 2015, Rao et al., 2003].

We evaluated an effect of a winter Shamal frequency on variations of Omani coral records in winter and the social incidents in Syria and Iraq by comparing coral records with *in situ* wind speed dataset.

Comparing Shamal frequencies with the modern coral records in winter revealed that frequent occurrences of winter Shamal decreased SST (increase of $\delta^{18}O_{coral}$ and Sr/Ca) and increased $\delta^{18}O_{sw}$ (Fig.6-4) in the Gulf of Oman. The positive correlations between SST proxies ($\delta^{18}O_{coral}$ and Sr/Ca) and winter Shamal frequencies suggested that accumulations of cold air by frequent occurrences of winter Shamal would increase $\delta^{18}O_{coral}$ and Sr/Ca (SST decreasing) in winter (Fig.6-4: Shamal frequencies vs. $\delta^{18}O_{coral}$; $r = 0.76$, $P < 0.01$, Fig.2-c: Shamal frequencies vs. Sr/Ca; $r = 0.82$, $P < 0.01$). The negative correlation between $\delta^{18}O_{sw}$ in winter and winter Shamal frequencies ($r = -0.58$, $P < 0.05$) would reflect storms and southward migrations of cold front due to Shamal.

Controlling factor of winter Shamal

Frequency of winter Shamal from 2000s would be increased under the less dominance of winter monsoon state in response to La Nina like state under the negative IPO which cause onset of the global-warming hiatus. Previous studies suggested that Saudi-Arabian dust transportation were enhanced by La-Nina state [Yan et al., 2015]. Recent negative-IPO from 1999 were under La-Nina-like state which could cause the global-warming hiatus (Fig.3-9). Recent IPO-state could induce the recent frequent Shamal. We examined controlling factor of Shamal frequency by comparing with IPO index.

Coral records (Sr/Ca, $\delta^{18}O_{coral}$ and $\delta^{18}O_{sw}$) were correlated with IPO index (Fig. 6-5: vs. Sr/Ca: $R = -0.51$, $p < 0.01$, vs. $\delta^{18}O_{sw}$: $R = 0.67$, $p < 0.01$, vs. $\delta^{18}O_{coral}$: $R = 0.32$, $p < 0.1$). This result suggested that frequency of winter Shamal would be controlled by teleconnections of IPO. Recent negative-IPO state decreased global-warming trend

and induced the global-warming hiatus [Fig. 3-4, Kosaka and Xie, 2014]. The global-warming hiatus might induce low frequency of Shamal. This recent IPO state would propagate as the recent frequent occurrences of Shamal to the Arabian Peninsula.

Wang et al., 2014 and Nazemosadat and Ghasemi, 2004 suggested that the propagation mechanisms of El-Nino (La-Nino) state to the western Asia would be interaction between ENSO state and Siberian high. El-Nino (La-Nina) like state intensified (weakened) Siberian high and easterly wind. In El-Nino like state, intensified Siberian high and easterly wind would contribute much vapor transportations to the western Asia. In the La-Nina like state (under the global-warming hiatus) this mechanisms were conversely affected on the western Asia and induced dominance of winter Shamal in the the western Asia.

SST variations in western pole of IOD in response to phase shift of IOD would not modulate both Sr/Ca and $\delta^{18}O_{sw}$ from Oman in winter [Fig.3-6]. Although SST anomaly in the western IOD region were significantly different between neutral and posi-IOD year under the global-warming trend [Fig3-6], SST_{anom} and $\delta^{18}O_{sw\text{-}anom}$ from Oman in winter of the posi-IOD year were similar with the neutral year. This result suggested winter climate in the Arabian Peninsula would be controlled by climate changes on the Eurasian continente.

6-4. Relationships between Summer Indian monsoon and Indian civilization

Summer monsoon reconstructions in the Holocene epoch.

Based on our calibration work using modern Omani coral, we could know the influence of Indian monsoon intensity and upwelling in the Arabian sea on both precipitation at the Indus valley and the Indian agriculture (Fig.6-2). By applying calibration work using modern Omani coral, we reconstructed variations of precipitations in the Indus valley (northwestern region) based on anomalies of Sr/Ca and $\delta^{18}O_{sw}$ in summer from Omai fossil corals (Fig.6-6). The fossil and modern coral records converted to anomalies of coral proxies by reducing averaged value in each time-windows. Sr/Ca in summer showed increasing (cooling) trend from 4.3 to 3.1kyBP. Anomalies of $\delta^{18}O_{sw}$ in summer showed a negative peak in 4.1 kyrBP. These results suggested that Indian monsoon showed intensified trend, however evaporations in the Arabian Sea decreased in 4.1kyrBP. Precipitation in the Indus valley would decrease in 4.1kyrBP due to the strong Indian monsoon and less evaporations.

Collapse/migration of Indus civilization due to the intensifications of summer Indian monsoon.

Archeological survey inferred transitions of Indus civilization started and Indus civilizations were disappeared in 4.0kyrBP [Giosan et al., 2012, Uesugi, 2009, Fig. 6-6, 6-7]. We compared fossil coral records with number of archeological sites around northwestern India and Pakistan regions (Balochistan, Sindh and Gujarat:

northwestern region) and northcentral Indian and Nepal regions (Punjab, Ghaggar, Aravali and Ganga: northcentral region) [Uesugi, 2009]. Number of archeological sites in each age and region were divided by total archeological sites through the Holocene in each region. The archeological data suggested that settlement decreased in northwestern region after 4.0kyBP. In the same timing of reductions of settlement in northwestern region, northcentral of India was increased.

The condition in the Indus valley in summer of 4.1 known from our fossil coral would trigger migration of civilians due to reductions of agricultural products in the Indus valley [Giosan et al., 2012, Uesugi, 2009]. These archeological evidences suggested that the center of civilizations moved from northwestern to northcentral region. Our modern coral records inferred that intensified monsoon and weak evaporation induced difficultness of agriculture in northwestern India due to less precipitations (Fig.6-6, 6-7). Our results consistent with sediment core from mouth of Indus river. This record from mouth of Indus river suggested that precipitations in Indus valley decreased in 4.0yrBP (Fig.6-6, 6-7). However, our records were inconsistent with speleothems in northcentral India. Speleothems in northcentral India suggested that precipitation in northcentral India was intensified in 4.0kyrBP. Our records and sediment core from mouth of Indus river suggested that crops in the Indus valley decreased due to aridifications and strong summer monsoon [Staubwasser et al., 2003]. They could move to northcentral India where precipitation increased in 4.0kyrBP [Kathayat et al., 2017]. We did not know what climate factor varied δ^{18}O in speleothem from northcentral. We need to compare fossil corals collected from southern part of Arabian Sea or Bay of Bengal for further discussion of Indian precipitation variability in summer through the Holocene.

6-5. Influences of frequent Shamal on the Mesopotamia civilization
Winter Shamal reconstructions in the Holocene epoch.

We reconstructed occurrences of the Shamal through the Holocene epoch by applying calibration results with the modern coral records to the fossils. The fossil and modern coral records converted to anomalies of coral proxies by reducing averaged value in each time-windows. Anomalies of δ^{18}O$_{coral}$ and Sr/Ca (δ^{18}O$_{sw}$) in winter of 4.1 kyrBP were the highest (lowest) in our 6 fossil and modern corals (Fig.6-8). After 4.1 kyrBP, anomalies of δ^{18}O$_{coral}$ and Sr/Ca (δ^{18}O$_{sw}$) in winter were stably low (high). The anomalous coral values of winter in 4.1 kyrBP were lasted for 3 months/year beyond the standard deviations (2σ) of the modern coral records in winter (Fig.6-9). The prolonged anomalous-values of coral records in 4.1 kyrBP suggested that the Shamal in 4.1 kyrBP was lasted longer periods in one year than the present. After recover of the prolonged Shamal from 3.7 kyrBP, intensity of winter monsoon became stable until 3.1 kyrBP (Fig. 6-8). The results from the Omani fossil corals were consistent with the record of wind-intensity reconstructed from the sediment core in the Gulf of Oman (Fig. 6-8, Cullen et al., 2000). Sediment core

from the Gulf of Oman suggested that the wind from the western Asia was intensified in 4.2 kyrBP and recovered from intensified condition to stable since *ca.* 3.8 kyrBP.

The Akkad empire collapsed by the social unrest derived from frequent occurrences of winter Shamal

High occurrences of the Shamal during 3 months in winter would have an impact on the society in the Mesopotamian region in 4.1 kyrBP. Our fossil coral records suggested that the Akkad empire in 4.1 kyrBP had experienced the severe dry- and cold- climate with much dust transportations in winter due to the prolonged Shamal. The severe drought in winter of 4.1 kyrBP would have an impact on the rainfed- and irrigated- agriculture in the Akkad empire. The drought and the collapse of the agricultural systems would decrease crops production in the Mesopotamia region in 4.1 kyrBP. The drought with much dust transportation by the Shamal would cause the collapse of the agricultural systems, which was a condition to be easy to stagnate flows of the irrigation and to salinize the irrigated-field [Jacobsen,1958]. Dust transportation would also increase risks of health hazards in the Mesopotamian region [Khaniabadi et al., 2017].

The Akkad empire would collapse by the social unrest derived from long durations of the Shamal. The social unrest in the Akkad empire would be increased by famines and risks of health hazards due to long durations of the Shamal. The social unrest and the agricultural failures in the Akkad empire could trigger their migration and/or high mortality in the Akkad empire. High mortality and/or migration in the Akkad empire would not be consistent with decreasing footprints of cities and villages around the Tell-Leilan in 4.1-3.8 kyrBP (Fig. 6-9, 6-10). Finally, the Akkad empire would collapse by the social unrest which was derived from long durations of the Shamal under like a situation before the Syrian civil war. Other populations could resettle under the stable intensity of winter monsoon from 3.8 kyrBP after the termination of the social turbulence under the prolonged Shamal.

6-6 Conclusions

6-6-1Indian ocean climate from the Omani coral

Summer under the global warming trend

Summer Indian monsoon weakened under the global warming trend (Fig.6-11,12). SST in the western India varied associated with the active Indian Ocean dipole which was affected by the global warming and intensified Walker circulations. On the northern side of Indian ocean, warming trend was not confirmed on the Eurasian continent during spring. As these results, Indian monsoon was weakened by the decreasing temperature-gradient between the Western Indian Ocean and the Eurasian continent. Weak summer Indian monsoon increased moisture transportations from the Arabian Sea to northwestern India and precipitations in northwestern India.

Summer under the global warming hiatus

Summer Indian monsoon would intensify under the global warming-trend (Fig.6-11,12). Under the global warming-trend, the Walker circulation weakens, and the Indian Ocean dipole would become inactive. SST in the western Indian Ocean decreased by the inactive Indian Ocean dipole. On the northern side, warming trend is confirmed on the Eurasian continent during spring. Summer Indian monsoon and upwelling in the Arabian Sea are intensified by increased temperature-gradient between the Western Indian Ocean and the Eurasian continent. Precipitation in northwestern India decreased by less moisture transportations from the Arabian Sea to the India. This less precipitation reduced the agricultural efficiency in the India

Winter Indian monsoon and Shamal under the global warming hiatus

Frequency of Shamal would be controlled by teleconnection of IPO (Fig.6-11,12). La Nina-like state under the negative state started from end of 1990s in the same timing with onset of the global-warming hiatus. La-Nina like state would weaken Siberian high and easterlies wind. This interaction between La Nina-like state and Siberian high would induce frequent winter Shamal and less dominance of winter Indian monsoon on the western Asia from 20th century.

Climate event in 4.2kyrBP

Our results suggested intensified summer monsoon and frequent Shamal in 4.0 kyrBP. These climate event would be occurred the similar condition with in mid-2000s under the global-warming hiatus. Previous proxy result suggested that ca. 4.2kyrBP might be anomalous cooling-era after the warming period in the mid-Holocene (so called hypsithermal: Walker et al., 2012). This transition from hypsithermal to anomalous cooling-era (4.2kyBP) might be triggered by same mechanism with transitions from the global-warming trend to hiatus in the present.

6-6-2 historical incidents

Our comparisons of archaeological evidences with monthly resolution paleo-climate reconstructions from corals revealed different reasons of civilization collapses between the Indus and Mesopotamia civilizations. Indus civilization would collapsed by intensified monsoon and less transportation to India in 4.0kyrBP. On the Mesopotamia civilization, the Akkad empire was collapsed by frequent winter Shamal and less precipitations in 4.0kyrBP.

Differences in time spans and intensity of climate changes would be influences on civilians' reaction. While frequent Shamal abruptly increased, summer Indian monsoon was gradually changed and recoverd. Indians who experienced gradual changes of Indian monsoon could migrates to northern part of Indus river. However, Mesopotamians who experienced abrupt changes of Shamal could not migrate their habitat and sustain their empire.

For improving social and economic structures in the present and future, it is necessary to understand the roles of climate systems to the human society for the past using combining approach with archeological evidences and paleo-climate records near to the cycles of human activity.

Reference

Macklin, M. G. & Lewin, J. The rivers of civilization. *Quat. Sci. Rev.* **114**, 228–244 (2015).

Jacobsen, T. & Adams, R. M. Salt and Silt in Mesopotamian Agriculture. 128, 3334 (1958)

Weiss, H. *et al.* The Genesis and Collapse of Third Millennium North Mesopotamian Civilization. *Science (80-.).* **261,** 995–1004 (1993).

Cullen, H. M. et al. Climate change and the collapse of the Akkadian empire: Evidence from the deep sea. *Geology* **28**, 379 (2000).

Walker, M. J. C. *et al.* Formal subdivision of the Holocene Series/Epoch: a Discussion Paper by a Working Group of INTIMATE (Integration of ice-core, marine and terrestrial records) and the Subcommission on Quaternary Stratigraphy (International Commission on Stratigraphy). *J. Quat. Sci.* **27,** 649–659 (2012).

Staubwasser, M., Sirocko, F., Grootes, P. M. & Segl, M. Climate change at the 4.2 ka BP termination of the Indus valley civilization and Holocene south Asian monsoon variability. *Geophys. Res. Lett.* **30,** 3–6 (2003).

Yancheva, G. *et al.* Influence of the intertropical convergence zone on the East Asian monsoon. *Nature* **445,** 74–77 (2007).

Haug, G. H. *et al.* Climate and the Collapse of Maya Civilization. *Science (80-.).* **299,** 1731–1735 (2003).

Kathayat, G. *et al.* The Indian monsoon variability and civilization changes in the Indian subcontinent. *Sci. Adv.* **3,** e1701296 (2017).

Pernone, T. J. Winter shamd in the Persian Gulf. Technical Report TR-79-06 (1979)

Zinke, J. *et al.* Seychelles coral record of changes in sea surface temperature bimodality in the western Indian Ocean from the Mid-Holocene to the present. *Clim. Dyn.* **43,** 689–708 (2014).

Abram, N. J. *et al.* Seasonal characteristics of the Indian Ocean Dipole during the Holocene epoch. *Nature* **445,** 299–302 (2007).

Watanabe, T., Kawamura, T., Yamazaki, A., Murayama, M. & Yamano, H. A 106 year monthly coral record reveals that the East Asian summer monsoon modulates winter PDO variability. *Geophys. Res. Lett.* **41,** 3609–3614 (2014).

Watanabe, T. K. *et al.* Past summer upwelling events in the Gulf of Oman derived from a coral geochemical record. *Sci. Rep.* **7,** 4568 (2017).

Miri, A., Ahmadi, H., Ghanbari, A., & Moghaddamnia, A. Dust storms impacts on air pollution and public health under hot and dry climate. *Int. J. Energy Environ,* **2**, 101-105 (2007)

Kelley, C. P., Mohtadi, S., Cane, M. A., Seager, R. & Kushnir, Y. Climate change in the Fertile Crescent and implications of the recent Syrian drought. *Proc. Natl. Acad. Sci.* **112,** 3241–3246 (2015).

Khaniabadi, Y. O. *et al.* Hospital admissions in Iran for cardiovascular and respiratory diseases attributed to the Middle Eastern Dust storms. *Environ. Sci. Pollut. Res.* **24,** 16860–16868 (2017).

Abdi Vishkaee, F. et al. Dust transport over Iraq and northwest Iran associated with winter Shamal: A case study. *J. Geophys. Res. Atmos.* **117**, D3 (2012).

Notaro, M., Yu, Y. & Kalashnikova, O. V. Regime shift in Arabian dust activity, triggered by persistent Fertile Crescent drought. *J. Geophys. Res. Atmos.* **120,** 10,229-10,249 (2015).

Rao, P. G., Al-Sulaiti, M. & Al-Mulla, A. H. Winter shamals in Qatar, Arabian Gulf. *Weather* **56,** 444–451 (2001).

Wilkinson, T. J. *et al.* The Structure and Dynamics of Dry-Farming States in Upper Mesopotamia. *Curr. Anthropol.* **35,** 483–520 (1994).

Reimer, P. J. *et al.* IntCal13 and Marine13 Radiocarbon Age Calibration Curves 0–50,000 Years cal BP. *Radiocarbon* **55,** 1869–1887 (2013).

Ren, L., Linsley, B. K., Wellington, G. M., Schrag, D. P. & Hoegh-guldberg, O. Deconvolving the $\delta18O$ seawater component from subseasonal coral $\delta18O$ and Sr/Ca at Rarotonga in the southwestern subtropical Pacific for the period 1726 to 1997. *Geochim. Cosmochim. Acta* **67,** 1609–1621 (2003).

Gagan, M. K. *et al.* Temperature and Surface-Ocean Water Balance of the Mid-Holocene Tropical Western Pacific. *Science (80-.).* **279,** 1014–1018 (1998).

Nurhati, I. S., Cobb, K. M. & Di Lorenzo, E. Decadal-Scale SST and Salinity Variations in the Central Tropical Pacific: Signatures of Natural and Anthropogenic Climate Change. *J. Clim.* **24,** 3294–3308 (2011).

USGS website (https://www.ncdc.noaa.gov/data-access/land-based-station-data/land-based-datasets)

the United Nations High Commissioner for Refugees website: http://popstats.unhcr.org/en/time_series

United states department of Agriculture: https://www.usda.gov

Kathayat, G. *et al.* The Indian monsoon variability and civilization changes in the Indian subcontinent. *Sci. Adv.* **3,** e1701296 (2017).

Kripalani, R. H. & Kumar, P. Northeast monsoon rainfall variability over south peninsular India vis-à-vis the Indian Ocean dipole mode. *Int. J. Climatol.* **24,** 1267–1282 (2004)
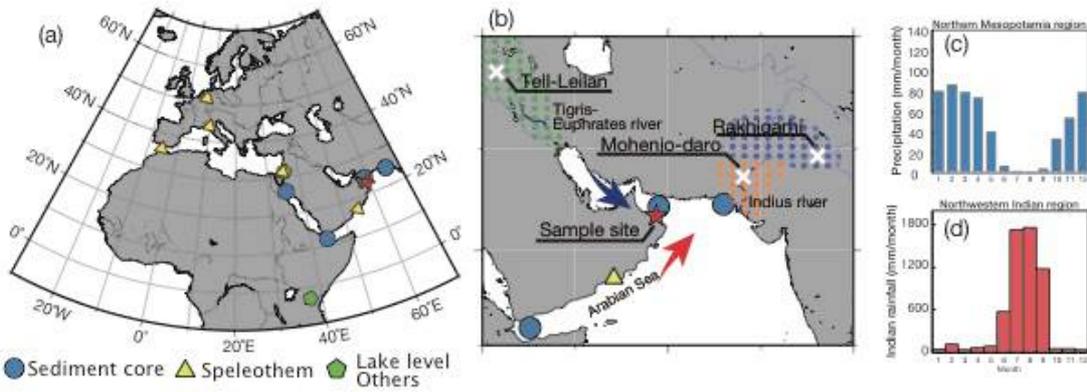
Figure 6-1

(a), (b): Maps of Europe, Africa and western Asia. Circle (sediment cores), triangle (speleothems) and pentagon (lake levels and others) showed the location of paleoclimate records which revealed the climate events in 4.2 kyrBP. White cross showed the archeological sites (Tell-Leiran, Mohenjo-Daro and Rakhi garhi). Area with green dots showed the fertile crescent, the Mesopotamia region. Area with orange and blue dot showed downstream and upper-stream of Indus river, respectively. Red stars showed our coral sample site (Sample site of fossil corals: 22°54'5" N, 59°13'22" E; the modern coral core: 23°30′ N, 58°45′ E) A gray star indicates measurement site for *in situ* wind speed respectively (c) and (d): In situ precipitation in the Mesopotamia region and Indus valley.
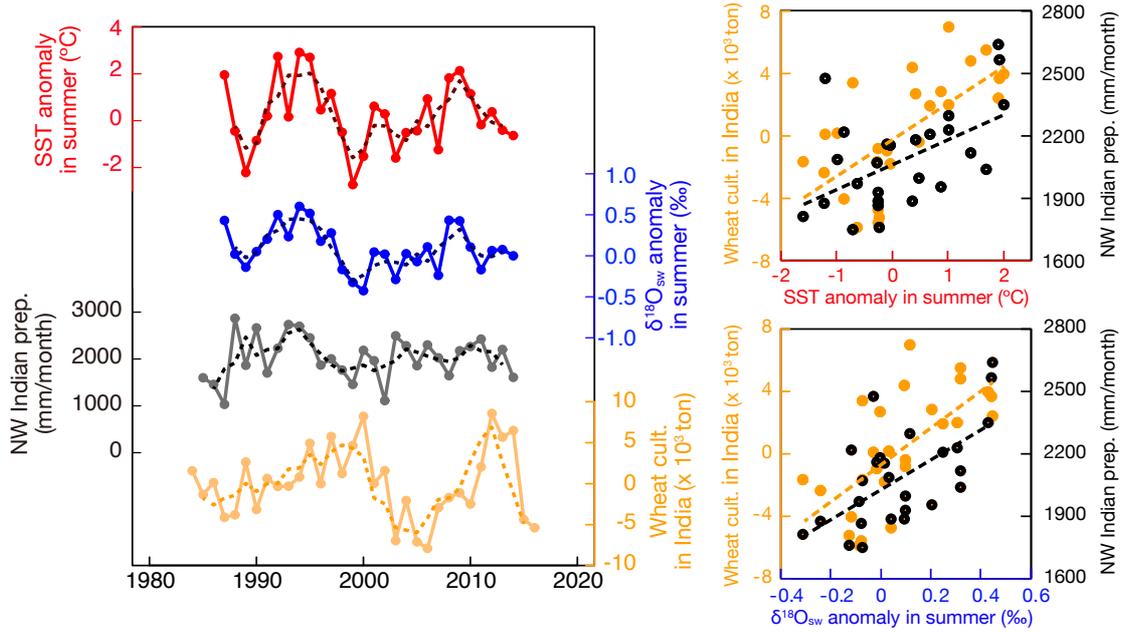
Figure 6-2

Left panel: Comparison among the Omani coral records (red: SST anomaly, blue: d18Osw), precipitation in the northwestern India (black) and wheat cultivation in the India (orange). Dot lines indicated 3 years moving average of each record.

Right panel: Scatterplot of summer coral records in summer (with 3 years lag) vs. maximum precipitations in the northwestern India (black dots) or wheat cultivations in India (orange dots).
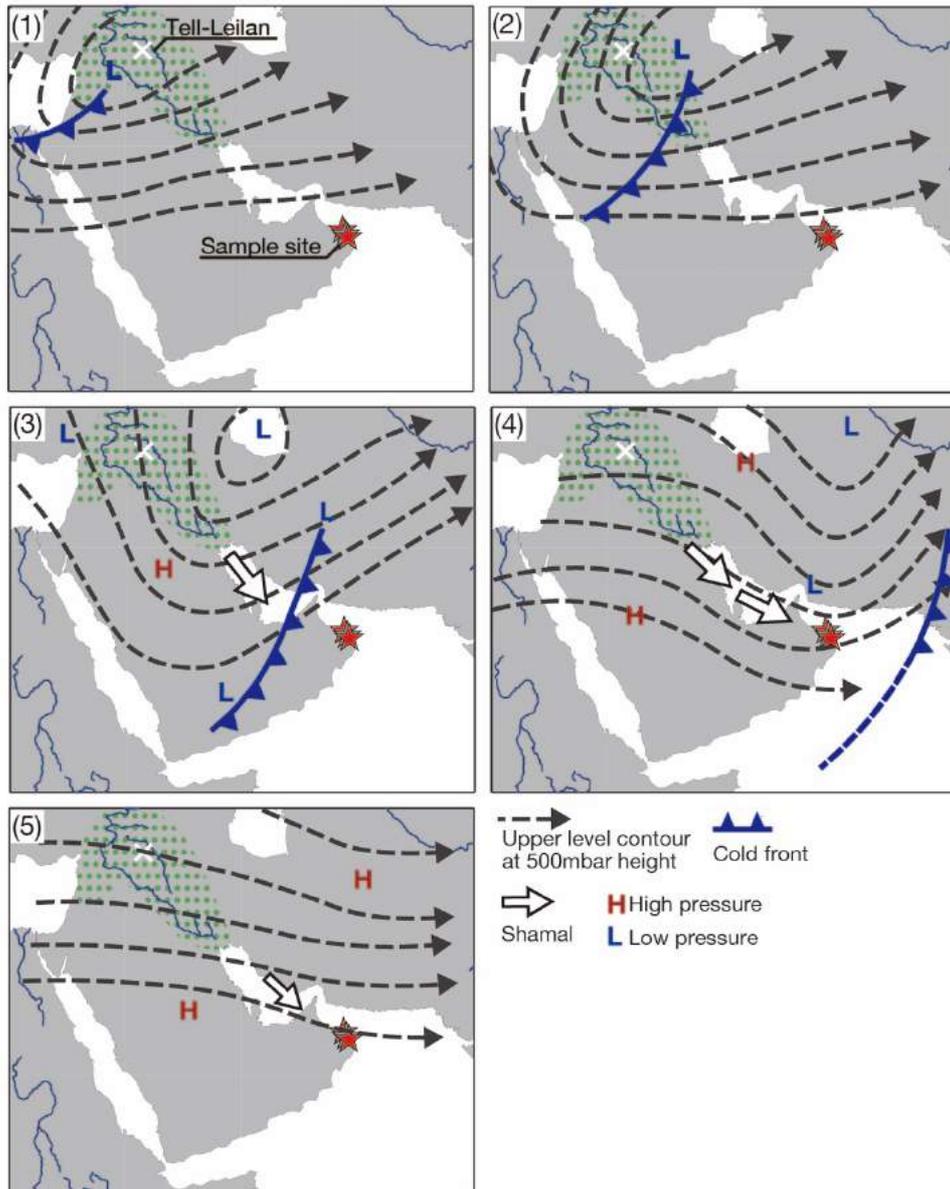
Figure6-3

Schematic diagrams of typical Shamal-climatrogy modified from Perrone, 1979 and Roa et al., 2001. Time intervals between each panel are 12hours-24hours and typical sequence of Shamal from (1) to (5) lasted for 3-5 days. (1)-(2): The upper trough and surface low move to eastward. A cold front extends south. (3)-(4): The upper trough moves eastward near to the Caspian Sea. New surface low formed at the Arabian Peninsula and Strong and shallow northwesterly wind set in the western new surface low. (5) The upper air trough moved away to eastward. The high cell over the Arabian Peninsula weakened. The Shamal weakened.
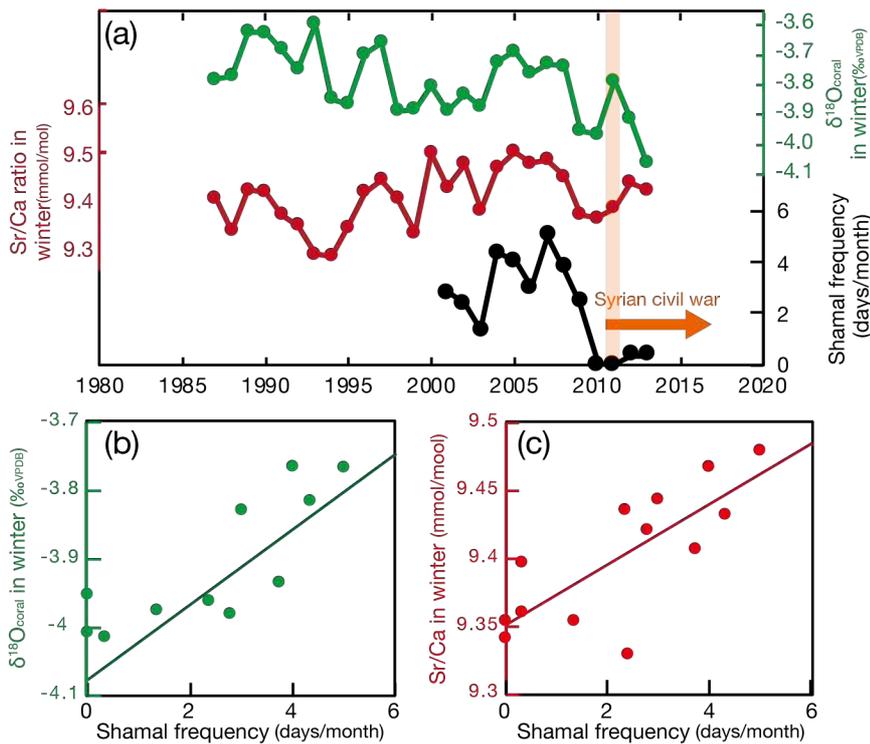
Fig.6-4

$\delta^{18}O_{coral}$ in winter (green) and Sr/Ca in winter (red) from the modern coral records.

The 3 years moving average records of them were shown using dot line (green- and red-dot line: $\delta^{18}O_{coral}$ and Sr/Ca). Black line showed Shamal days (wind data from the meterogical data at Port Sultan Qaboos N23°37', E58°34). Wind data was available from USGS website (https://www.ncdc.noaa.gov/data-access/land-based-station-data/land-based-datasets). Blue and orange line showed wheat production at Iraq and Syria respectively. The 3 years moving average records of wheat productions were shown using dot line. Wheat production dataset were available from United states department of Agriculture: (https://www.usda.gov). Bars showed refugees in Iraq (blue) and Syria (orange). Dataset of refugees was available from Office of the United Nations High Commissioner for Refugees (UNHCR: http://popstats.unhcr.org/en/time_series). The arrows and color hatches showed the social events in Iraq (blue) or Syria (orange).
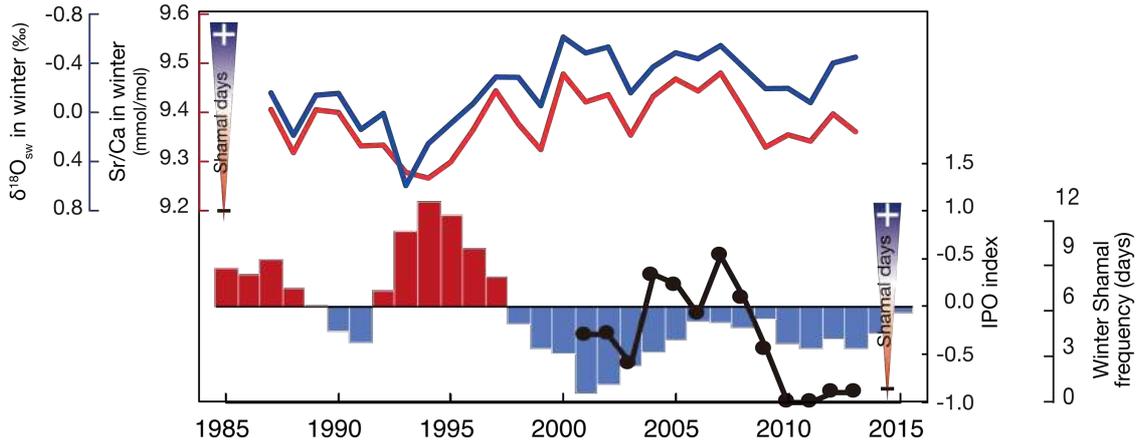
Figure 6-5

Comparison among coral records in winter and climatic index.

Red (blue) line showed Sr/Ca ($\delta^{18}O_{sw}$) in winter. Black line showed frequency of Shamal. Purple line showed Eurasian snow cover in Autumn
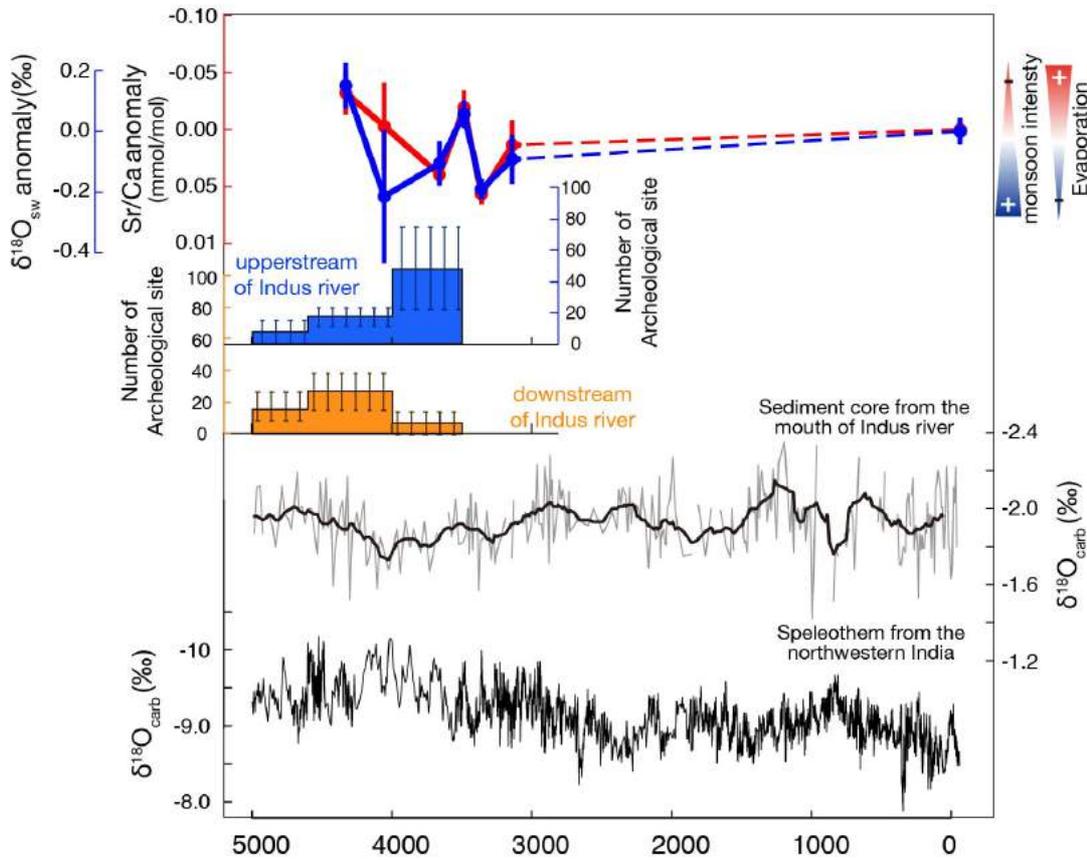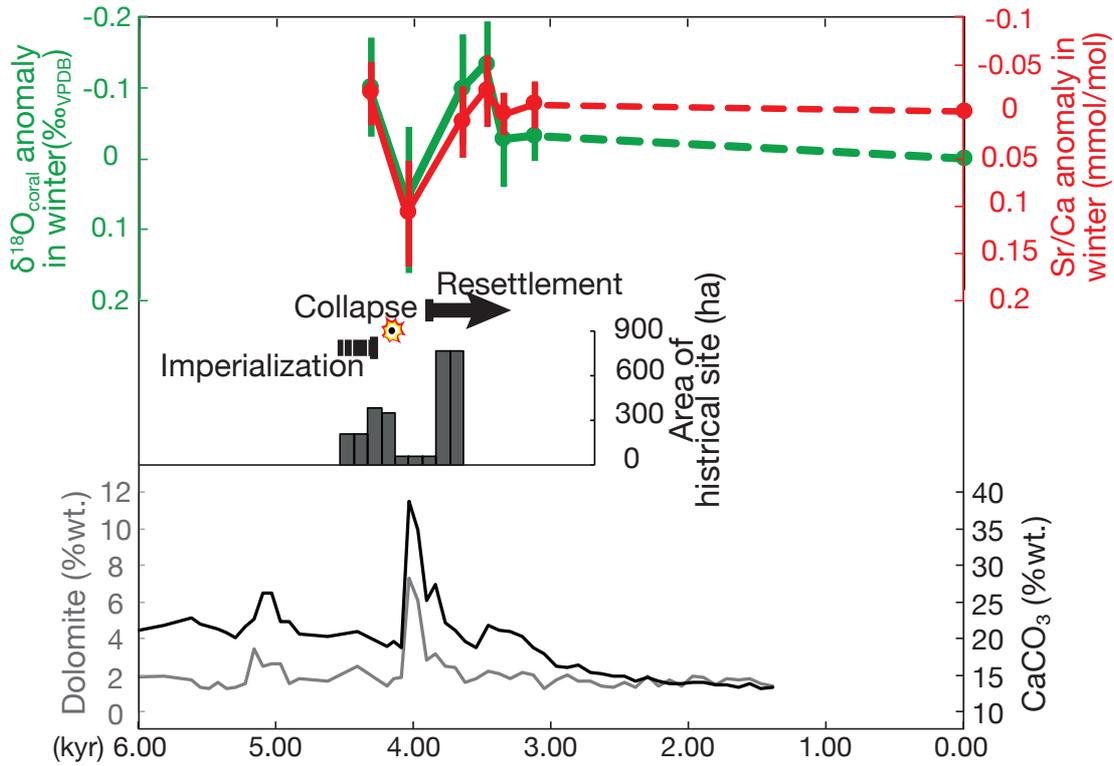
Figure 6-6

Sr/Ca anomaly (red) and $\delta^{18}O_{coral}$ anomaly (green) in summer from 4.3 ka to modern. Error bars indicate standard error of each proxy in each age.

Civilized data around the downstream (orange) and upper-stream (blue) of Indus river. Age of area at historical sites were determined with morphology of ceramics.

$\delta^{18}O_{carb}$ in the sediment core from mouth of the Indus river suggested that Indian monsoon weakened. Speleothems in the northern-central India suggested that precipitations in northcentral India were Increased in 4.0kyrBP.

mid 4.0s kyBP   mid and late 4.0s kyBP   early 3.0s kyBP
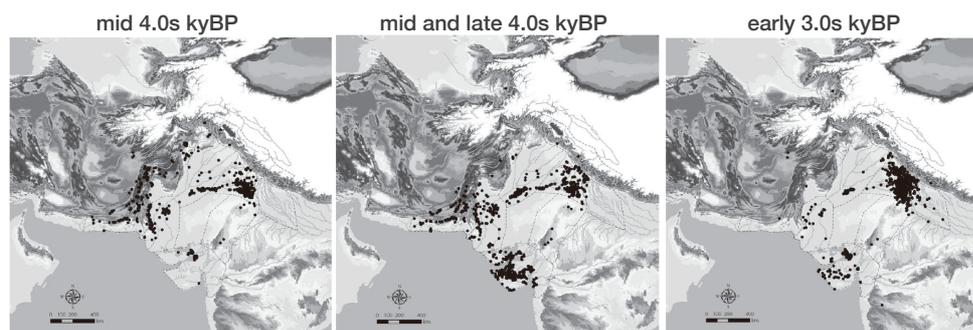
Figure 6-7

Archeological survey in the Indus Valley [modified from Uesugi et al., 2009].

Figure 6-8

Sr/Ca anomaly (red) and $\delta^{18}O_{coral}$ anomaly (green) in winter from 4.3 ka to modern. Error bars indicate standard error of each proxy in each age.

Civilized data around the Akkad empire. Age of area at historical sites were determined with ^{14}C age. This record suggested that Akkad empire collapse from 4.2 to 3.8 ka and after that, the Mesopotamian region was resettled by other civilians.

Mineral composition records in the sediment core from the Gulf of Oman. They suggested that wind from western Asia was abruptly intensified in 4.2ka.
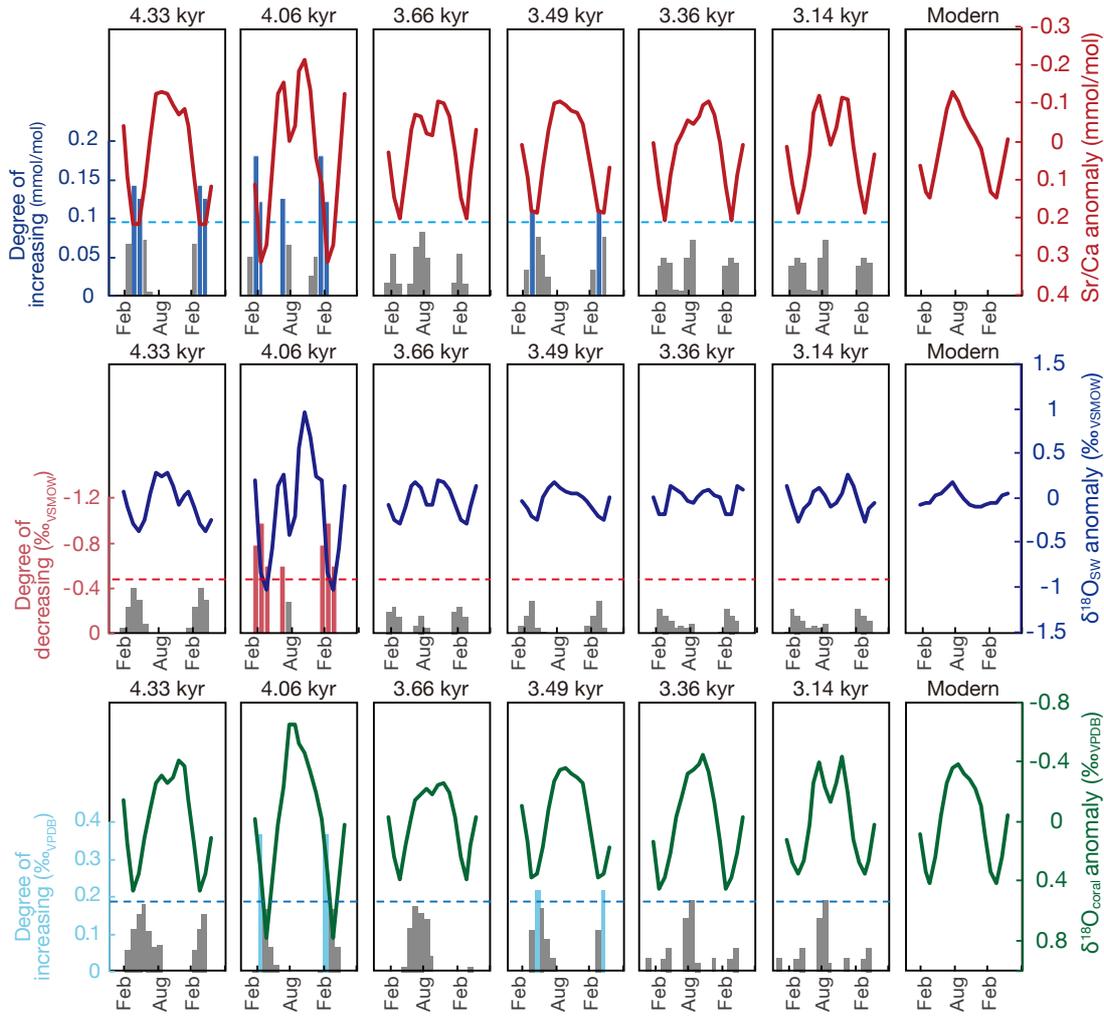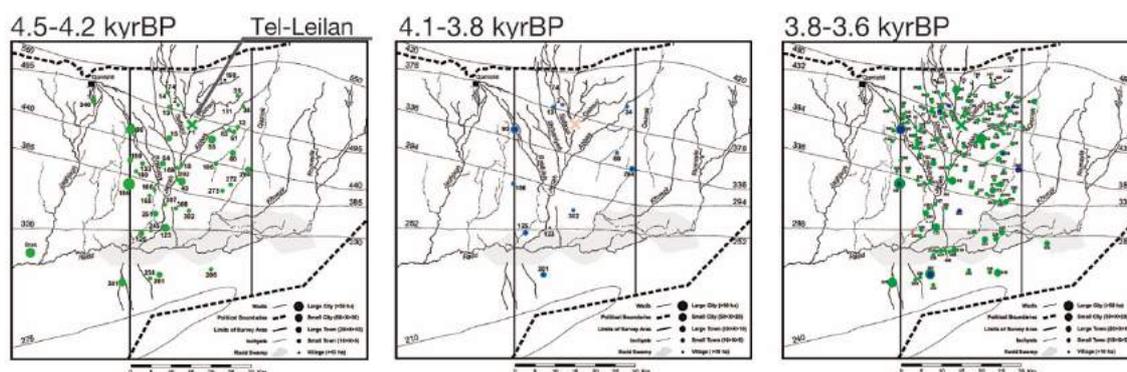
Figure 6-9

Mean seasonal cycles of coral records (red: Sr/Ca, blue: $\delta^{18}O_{sw}$, green: $\delta^{18}O_{coral}$) and degree of anomaly index relative to modern (colored/gray bar). The thresholds of anomalously increasing (decreasing) of coral records were defined that degree of anomaly was over standard deviation of modern $\delta^{18}O_{coral}$ record (dot line). Months with anomalous climate relative to the present were indicated using colored bar.

131

Result of archeological survey. panels showed distributions of archeological sites around metropolis of Akkad empire (cross mark) in 4.5-4.2, 4.1-3.8 and 3.8-3.6 kyrBP (modified from Weiss et al., 2004).
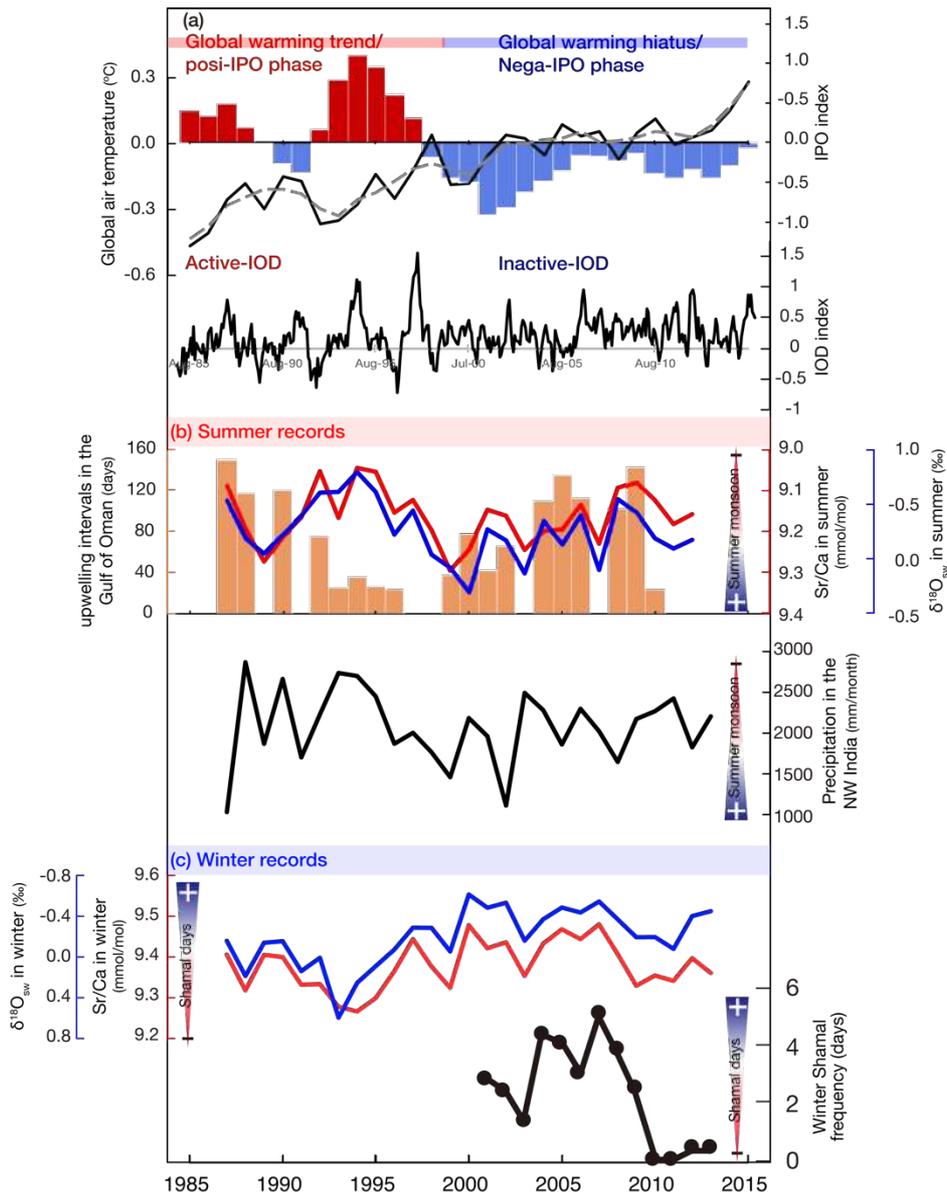
Figure 6-11

Comparison among coral records in summer and winter, and climatic index.

(a) Global air temperature (black dot). gray dot line shows 3 years moving average lines. IPO index showed red (positive) and blue (negative) bars. Black line showed IOD index.

(b) summer records. Red (blue) line showed Sr/Ca ($\delta^{18}O_{sw}$) in summer. Black line showed precipitation in northwestern India. Purple line showed Eurasian snow cover in spring.

(c) winter records. Red (blue) line showed Sr/Ca ($\delta^{18}O_{sw}$) in winter. Black line showed frequency of Shamal. Purple line showed Eurasian snow cover in Autumn.
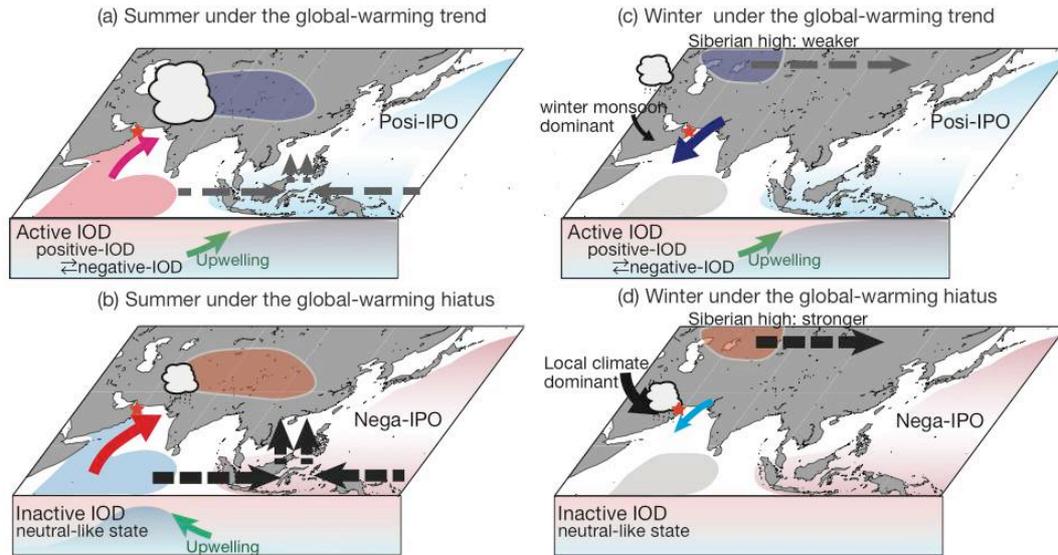
Fig.6-12

Schematic diagram for showing the difference of climate among summer/winter under the global-warming trend (left panels) and summer/winter under the global-warming hiatus (right panels).

On left panel, pink (red) arrow showed weak (strong) summer Indian monsoon. Gray (black) dot arrows showed strong (weak) Walker circulations.

On right panels, blue (red) arrow showed weak (strong) winter Indian monsoon. Gray (black) dot arrows showed strong (weak) easterlies wind. Gray (black) arrow showed frequent (less) winter Shamal

# 7. Conclusions and future perspectives of paleo-climate reconstruction using reef corals

7-1 General conclusions

In this thesis, snap-shots of the winter and summer Indian Monsoon were showed in biweekly or monthly resolution based on Omani and Arabian corals from the Holocene epoch to the present. The modern Omani and Arabian corals recorded upwelling in summer which was unrecorded by satellite-based data [Watanabe et al., 2017]. The modern Omani corals reflected fluctuations of the summer Indian monsoon and local climatic events (winter Shamal) which affected on agricultures in India and the western Asia (Syria and Iraq), respectively. Omani fossil corals suggested that seasonality of Indian monsoon was the important climate factor for transitions of human activities. These conclusions succeed by the following three advantages in coral archives (1) high-precision and long-term reconstruction beyond the satellite-based and in situ data (2) calibration using modern corals and applying it on fossil corals (3) high resolution archives near to cycles of human activity.

(1) Our modern Omani and Arabian coral recorded upwelling in the Gulf of Oman and the Arabian Sea, respectively. Upwelling was difficult to detect using satellite-based data. Previous studies reported in situ SST dataset could revealed upwelling events. Our coral records could extend the evidence of upwelling in the Gulf of Oman.

(2) We could find the fossil and modern corals near to human-living sites. The climate reconstructions from modern corals were comparable with those from fossil corals. Using modern corals, it was possible to calibrate between coral records and climate variabilities, and between coral records and response of human activities against climate changes. This calibration could apply to fossil corals and historical incidents. Because other records (speleothems or sediment cores) easily lost information of climate changes in the present due to sampling process or temporal-resolution, they were difficult to calibrate among reconstructed records, climate changes and human activities.

(3) Coral records are comparable with human activities, because corals could provide high temporal resolution (weekly-monthly) records for decades-centuries (Table. 7-1). Coral records could reveal seasonal change of monsoonal precipitations which are important climate factor for humans' lives. Humans activities to survive were characterized in seasonal changes (Sato et al., 2012). For surviving, it is necessary to secure drinking water and energy (agriculture, hunting and gathering), which is controlled by variations of fresh water (precipitation river water).
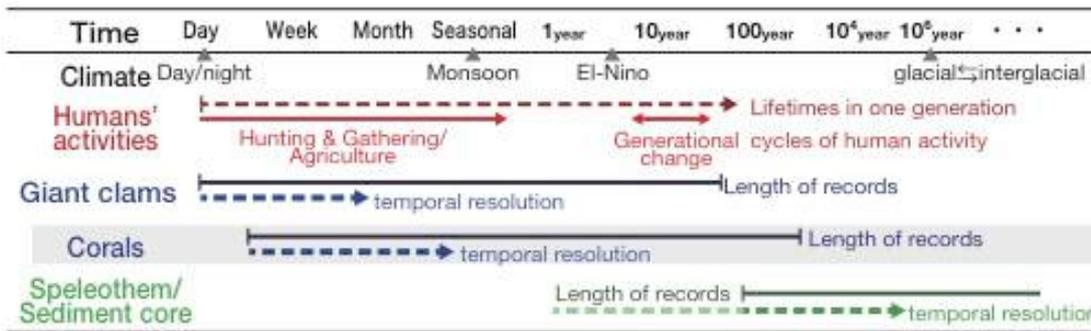
Table 7-1 Table indicate timespans of humans and their activities, and length of records and temporal resolutions of coralgiant calms, speleothems, and sediment core.

7-2 Future perspectives

Improving SST reconstructions

Previous corals archives focused on long-term variability (eg. ENSO and global warming) using SST proxy ($\delta^{18}O_{coral}$ and Sr/Ca) [Abram et al., 2016, Watanabe et al., 2011, Cobb et al., 2013, Cobb et al., 2003]. SST estimations using Sr/Ca have some problems for discussions of absolute SST and monthly-resolution variability.

One problem of coral archives is found on process of inserting time axis in coral records. Now, we mainly inserted time axis by assuming constant growth rate between maximum and minimum SST. However, previous works reported differences of growth rate between in intra-seasons [Barnes and Lough, 1993, Yamazaki et al., 2009, Fallon et al., 1999]. This difference of growth rate would modulate SST variations recorded in coral skeletons from in situ SST. We better improved methods of inserting time axis by conducting U-Th age determination and/or mathematical calculations (eg. Monte Calro simulations between high/lowSST and low/high Sr/Ca) [Scholz andHoffmann, 2011, Hendy et al., 2012].

Intercepts in SST dependency of Sr/Ca were different among the coral sites and species. Previous studies suggested these differences of intercept would come from vial effect of coral [Cohen et al., 2016]. Due to these difference of intercept, precision of absolute SST was huger than the seasonal cycles in coral sites [Gaetani et al., 2009, Correge, 2006, Cohen et al., 2016]. For discussing past absolute SST, we need to improve SST proxy in coral skeletons. Recently, trace element proxy (Li/Mg ratio and Sr-U SST, Reighley based SST based on Sr and Mg) in cold coral which are not divided by Ca try to be used for absolute SST estimation [Gaetani et al., 2009, Cohen et al., 2016, Fowell et al., 2016]. These new proxies try to remove vital effect of corals from Mg/Ca and Sr/Ca ratio. However previous calibration works using Li/Mg ratio and Reighley based SST were calibrated based on small deference of annual/seasonal SST. We could improve Li/Mg and Reighley based SST using corals from the Indian Ocean and the Pacific where difference of SST is huger than previous studies.

136

Relationships of climate variabilities and human activities

Our thesis concluded that high temporal resolution records from fossil corals were comparable with historical human activities. Corals can provide over 100 years records. Long-term coral records can cover lifespans of humans (average: 40-70 years).

Age of fossil corals would be also preciously comparable with archeological ruins. Age determinations of corals were conducted by methods of U-Th, U-Pb, radiocarbon, racemization and electron spins response (ESR) [Shen et al., 2008, Quigley et al., 2012, Hendy et al., Iketani, 1985]. Age determinations used in coral skeletons were also applied for dating of archeological evidences (e.g. EPS in bones, ^{14}C in archeological ruins and U-Th/U-Pb age from cave deposits) [Richter et al., 2017, Weiss et al., 1993, Richards et al., 2015, Pike et al., 2012].

Coral records can provide climate changes which humans experienced in their lives and their histories. Climate changes which humans experienced in the past are unrevealed. These climate changes are important to reveal complex of humans' developments [Dennell et al., 2012]. Coral records are an analogue to reveal how humans survived and expanded their habitat in the historical time-scales.

References

Dennell, R., Petraglia, M. D. & Asia, S. The dispersal of Homo sapiens across southern Asia : how early , how often , how complex ? **47,** (2012).

Fowell, S. E. et al. Intrareef variations in Li/Mg and Sr/Ca sea surface temperature proxies in the Caribbean reef-building coral *Siderastrea siderea. Paleoceanography* **31**, 1315–1329 (2016).

Hendy, E. J. *et al.* Assessing amino acid racemization variability in coral intra-crystalline protein for geochronological applications. *Geochim. Cosmochim. Acta* **86,** 338–353 (2012).

Ikeya, M. Electron Spin Resonance Dating. *J. Geogr. (Chigaku Zasshi)* **94,** 711–716 (1986).

Quigley, M. C. *et al.* U / Pb dating of a terminal Pliocene coral from the Indonesian Seaway. **314,** 57–62 (2012).

Richter, D. *et al.* The age of the hominin fossils from Jebel Irhoud, Morocco, and the origins of the Middle Stone Age. *Nature* **546,** 293–296 (2017).

Richards, Z. T. *et al.* New precise dates for the ancient and sacred coral pyramidal tombs of Leluh (Kosrae, Micronesia). *Sci. Adv.* **1,** e1400060 (2015).

Pike, A. W. G. *et al.* U-series dating of paleolithic art in 11 caves in Spain. *Science (80-.).* **336,** 1409–1413 (2012).

Shen, C. *et al.* Variation of initial 230Th/232Th and limits of high precision U–Th dating of shallow-water corals. *Geochim. Cosmochim. Acta* **72,** 4201–4223 (2008).

Watanabe, T. K. *et al.* Past summer upwelling events in the Gulf of Oman derived from a coral geochemical record. *Sci. Rep.* **7,** 4568 (2017).

Weiss, H. *et al.* The Genesis and Collapse of Third Millennium North Mesopotamian Civilization. *Science (80-.).* **261,** 995–1004 (1993).

Appendix: Improving analytical methods of Sr/Ca ratios in coral skeletons to specialize the paleo-SST reconstruction using ICP-OES.

Abstract

Strontium/Calcium ratios in coral skeletons (Sr/Ca) were widely used for SST reconstruction with bimonthly-weekly resolution. Because reef corals could live thorough over 100 years with high growth rate, reconstructed SST from Sr/Ca was one of the important datasets to discuss variations of coral growth and past climatic variability in the past. For SST reconstruction from Sr/Ca, it is required preciously to measure Sr and Ca in the same time. Because Ca concentrations in coral skeletons were 20times higher than Sr, matrix effect from high Ca concentration would affect on sensitivities of both Ca and other elements on ICP-OES. We evaluated sensitivities of Sr, Ca, and Sr/Ca against Ca concentration using ICP-OES. Based on our evaluation of high Ca effect on spectral intensity, we developed rapid Sr/Ca analysis method using ICP-OES with small amounts of coral powder (< 100ug) for high accurate SST-estimation. Our results suggested Sr and Ca were not affected by matrix-effect of Ca-concentration below 9 ppm. Sensitivities of Sr and Ca over 10ppm Ca concentration were significantly decreased by matrix effect and not suitable for high precision Sr/Ca analysis. In 7 ppm of Ca concentration, the combination of Sr (421.5nm) and Ca (373.6nm) was the most stable in our measured wavelengths.

1. Introduction

Strontium/Calcium ratios in coral skeletons (Sr/Ca) is the one of the most suitable SST proxies among trace-elements in coral skeletons, because Sr/Ca have a possibility to reflect only SST variations [Smith et al., 1987, Shen et al., 1996, Inoue et al., 2007, Delong et al., 2016]. Massive reef-corals over 4m height are lived in 400 years old with high extension rate (> 10 mm/yr) [Zinke et al., 2004, Hendy et al., 2002, Lough and Barnes, 2000]. SST reconstructions from Sr/Ca from reef corals in wide area could provide semi-global oceanic environment changes (*e.g.* global warming, Pacific Decadal Oscillation) [Abram et al., 2016]. High spatial/temporal resolved SST proxy were useful to discuss the seasonal variations of calcification rate [Taylor et al., 1995, Fallon et al., 1999, Yamazaki et al., 2009].

High precision Sr/Ca measurement is necessary for paleo-SST estimation. After improved method of Sr/Ca measurement using Thermal Ionization Mass Spectrometry (TIMS: Beck et al., 1992), precision of Sr/Ca got higher and paleo-SST reconstruction studies using reef-corals started to be widespread [Alibert and McCulloch, 1997; Hendy et al., 2002]. Instead of TIMS methods, Inductively Coupled Plasma Mass Spectrometry (ICP-MS) and Laser Abrasion ICP-MS (LA-ICP-MS) were also used for Sr/Ca measurement.

More rapid analysis of Sr/Ca was widespread after establishing the analysical method with Inductively

Coupled Plasma Optical Emission Spectrometer (ICP-OES: Schrag, 1999, Pfeiffer et al., 2004, Yudawati et al., 2009, Nurhati et al., 2010). However, it would be difficult to measure Sr concentration simultaneously with Ca concentration using ICP-OES, due to a matrix effect from Ca which is the highest concentrated cation in coral skeleton (*ca.* 20 times higher Ca concentration in coral skeleton than Sr concentration) [de Villers, 2002, Okai et al., 2002].

Analytical methods described in de Villers et al. [2002] had a potential to overcome matrix effect of high Ca concentration against analysis of trace element, by direct analysis of Mg/Ca ratio in foraminifera. We improved analytical method of Mg/Ca in foraminifera using ICP-OES [de Villiers, 2002] to SST reconstruction from Sr/Ca in coral skeleton. Analytical method of Mg/Ca in foraminifera [de Villiers, 2002] was evaluated matrix effect of high Ca concentration (over 20 ppm in 10-20ppm steps). The range of Ca concentration evaluated by de Villers (2002) was too high to apply SST reconstruction from Sr/Ca measurement, because 20-400ppm of Ca concentration was equal to ca.200ug-2mg coral skeleton in 5ml solution. We evaluated Sr/Ca analysis method with low Ca concentration solutions to get Sr/Ca records in high temporal resolution using ICP-OES.

2. Method

2-1. Instrumental condition

Sample and standard solutions were analyzed using ICP-OES (iCAP6200, Thermofisher Scientific) loaded in Hokkaido university. Operating conditions of ICP-OES were listed on TableS1. Sample solutions were induced with auto-sampler (, Thermofisher Scientific). Each solution was measured in 5 times respectively. Between each solution, analytical line was washing using 6 wt.%HNO3 in 1 minute to avoid contamination from prior-samples and to keep equilibrium. We calculated averaged intensity and standard deviation (n = 5) at each solution.

We used JCp-1 as a standard material for trace element measurement in coral skeletons, which was provided by AIST and prepared from a modern *Porites* coral colony corrected from Ishigaki Island [Okai et al., 2002]. Certified values in Sr/Ca and Mg/Ca in JCp-1 were determined by Inter-laboratory studies (Sr/Ca: 8.838 mmol/mol; Mg/Ca: 4.199 mmol/mol: Hathorne et al.,2013).

2-2. Evaluation of matrix effect

We evaluated matrix effect from Ca in coral skeleton by measurement of solutions with step-changed Ca-concentrations. JCp-1 were weighed (from 0.39 mg to 3.56 mg) and dissolved with 25% HNO3 acid (prepared from trace element analysis glade: provided by WAKO Pure Chemical Industrials, Ltd). Each sample solutions were diluted ca.3% HNO3 acid in 50 mL solutions, and Ca concentrations were adjusted from 3 to 27 ppm in 1 or 2 ppm steps using Milli-Q (18.0 MΩ-cm at 25ºC, Milli-pore). Ca concentration in each solution were gravimetrically

calculated based on the reported Ca concentration in JCp-1 [Okai et al., 2002]. JCp-1 solutions for test analysis were stored in 50ml PP centrifuge tubes. JCp-1 solutions with each concentration were dispensed 5 ml into five PP centrifuge tubes respectively. In this sequence, we measured blank solution (3 wt.%HNO_3) and running standard solution (JCp1 solution: 15ppm Ca concentration, 3 wt.%HNO_3) after every 5 samples measurement for evaluation an effect of instrumental drifts.

Sensitivities of cations (Sr^{2+}, Mg^{2+} and Ca^{2+}) relative to Ca concentrations were defined as

$$\text{Sensitivity of cations} = \frac{\text{Int}_{Me} - \text{Int}_{Me}}{\text{Conc}} \times 100 \quad [1]$$

where Int_{Me} and $\text{Int}_{BLK\text{-}Me}$ were analytical intensity of cations (Sr, Mg and Ca) in each sample and blank, and Conc was Ca concentration. Sensitivities at each Ca concentration were normalized relative to that at 15 ppm Ca concentration by dividing each value by the value at 15ppm Ca concentration. Intensity ratio were calculated as follows.

$$\text{Intensity ratio}_{Me/Ca} = \frac{\text{Int}_{Me} - \text{Int}_{BLK-Me}}{\text{Int}_{Ca} - \text{Int}_{BLK-Ca}} \quad [2]$$

Sensitivity of intensity-ratio$_{Me/Ca}$ were estimated by dividing each intensity-ratio by that value at 15ppm Ca concentration.

3. Results and Discussions

3-1. Sensitivity of Ca

Estimated Ca concentrations had a good correlation with intensity of Ca (r = 0.999, P < 0.01: Fig1-a). The intensities of Ca were higher in order of Ca(317.9nm) > Ca(373.6nm) > Ca(315.8nm) > Ca(370.6nm) (Fig1-a). Response of Ca-sensitivity to increased Ca concentration was difference among wavelengths of Ca (Fig1-b). Sensitivity of Ca(317.9nm) was significantly decreased from 3 to 27 ppm, as Ca concentrations were increased (Fig1-b). The sensitivities of other spectral wavelengths of Ca (Ca(315.8nm), Ca(370.6nm), Ca(373.6nm)) were stable below Ca 10 ppm concentration. Over Ca 10 ppm, the sensitivities were not stable in all spectral wavelengths of Ca.

To get condition with the highest sensitivity of Sr and Ca, Ca which is the highest concentration cation in coral skeleton should not produce the matrix effect to itself and Sr. To avoid the matrix effect from high concentration cation, it is necessary to enough dilute sample solutions. Our sensitivity evaluation suggest Ca matrix effect appeared on the Ca intensity from 10 ppm Ca concentration without wavelength of Ca(317.9nm). Especially, the high stability from 3-10 ppm Ca concentration (0.26-0.32%) wavelengths of Ca(315.8nm), Ca(370.6nm) and Ca(373.6nm) suggested that the lower Ca concentration than 10ppm got stable against the Ca matrix effect. Sensitivity of wavelength of Ca(317.9nm) showed decreased trend from 3-27 ppm Ca concentration (-0.16 cts×Ca-concentration⁻

[1], r = -0.97, P < 0.01) due to saturations from too high sensitive wavelengths for measurement of coral Ca. For Ca analysis, Ca concentration should be lower than 9ppm to avoid matrix effect using wavelengths of Ca(315.8nm), Ca(370.6nm) and Ca(373.6nm). The difference of Ca wavelengths was not shown among the Ca(315.8nm), Ca(370.6nm) and Ca(373.6nm) until 9ppm.

3-2. Sensitivity of trace element

Linearity between intensity of Sr and Ca concentrations were shown in every wavelengths of Sr (Fig.2-a). The intensities of Sr were higher in order of Sr(421.5nm) > Sr(407.7nm) > Sr(346.4nm) > Sr(216.5nm) (Fig2-c). Intensities of Sr(421.5nm) and Sr(407.7nm) were 10 times higher than those of Sr(346.4nm) and Sr(216.5nm).

We confirmed a difference of response of Sr-sensitivity to increased Ca concentration among wavelengths of Sr by adapted sensitivity calculation to each Sr-wavelengths (Fig1-b). Sensitivities were varied within 5% without Sr(216.5nm). Sensitivities of Sr-wavelength (Sr(346.4nm), Sr(407.7nm), Sr(421.5nm)) were gradually decreasing from 102 to 99 %, as Ca concentration were increasing from 3 to 5 ppm and over 10 ppm. From 5 to 10 ppm Ca concentration, sensitivities of Sr wavelength (Sr(346.4nm), Sr(407.7nm), Sr(421.5nm)) were relatively stable.

3-3. Matrix effect on Sr/Ca sensitivity

Sr/Ca analysis would be affected by the difference of response of sensitivity between Sr-wavelength and Ca-wavelength against high Ca concentration. It is necessary to avoid matrix effect from Ca to both Ca and Sr in simultaneous measurement of Sr and Ca.

To confirm the matrix effect from Ca to Sr/Ca, we checked changes of Sr/Ca sensitivities. Sr/Ca combined between Ca(317.9nm) and any Sr wavelengths showed increasing trend with increasing Ca concentration. The sensitivity of Sr/Ca based on any Sr wavelengths per Ca(317.9nm) correlated with the sensitivity of Ca(317.9nm). Sr/Ca of combination between Ca wavelength (Ca(370.6nm) and Ca(315.8nm)) with low-intensity and any Sr wavelengths showed Sr/Ca sensitivity decreased as Ca concentration decreased. Sr/Ca sensitivity with any Sr wavelengths and Ca(315.8nm) correlated with sensitivities of each Sr wavelengths. Sr/Ca sensitivity with any Sr wavelengths and Ca(370.6nm) correlated with both sensitivities of Ca and each Sr wavelengths. Sr/Ca sensitivities using Ca(370.6nm) with mid-intensity did not correlated with sensitivities of both Ca and Sr. Therefore, Sr/Ca using Ca wavelengths with too high and low Ca intensity were controlled by matrix effect from amounts of coral samples. Sensitivities of Sr/Ca would be more stable due to avoided from the matrix effect from amounts of coral samples based on combinations of Sr(421.5nm or 407.7nm) and Ca(373.6nm) wavelengths with appropriate intensity

4. Analytical procedures and applications

We measured Sr/Ca ratio in JCp-1 solutions and a Porites coral from Kikai island as applications studies of our

method. Precisions of our methods were estimated from this replicated JCp-1 analysis.

4-1. Analytical procedures

4-1-1 Preparations of calibrations solutions

We gravimetrically prepared 6 solution with different Me/Ca ratio values (Sr/Ca values are 0.0, 6.0, 8.0, 8.4, 8.8, 9.2, 9.8 mmol/mol) in same Ca concentrations. Mg^{2+} and Ba^{2+} were also added in standard solutions for matrix matching with solutions dissolved coral skeletons (Mg/Ca: 0.0 - 6.0 mmol/mol, Ba/Ca: 0.0 – 10.0 umol/mol). These solutions were prepared from each element standard solution (WAKO Pure Chemical Industrials, Ltd) and Milli-Q, and stored in 250mL PP bottles. Ca concentrations were constant in *ca.* 7 ppm, and Me (Sr, Mg and Ba) concentrations were varied in these solutions. The calibration line was established for converting from Intensity ratio$_{Me/Ca}$ to Me/Ca ratio based on the analytical results of standard solutions.

4-1-2 Preparations of sample solutions and reference standard

Coral samples were weighed 80-100ug into 10mL PP centrifuge tubes and dissolved with 0.5 ml 25%HNO_3 acid. Dissolved coral samples were diluted in 7 ppm Ca concentration and *ca.* 3%HNO_3 with Milli-Q. We did not conduct pre-treatment after microsampling, because Sr/Ca would be less sensitive to chemical treatments than other proxies (eg. Mg/Ca ratio, Ba/Ca: Watanabe et al., 2001, Nagtegaal et al., 2012). Sample solutions were introduced and analyzed using same analytical line on ICP-OES with standard solutions (Table S1).

JCp-1 solutions (7ppm Ca concentration and 3% HNO_3) were measured for reference/running standard to correct an effect of instrumental drift after every five sample measurements. JCp-1 were weighed and dissolved with 25%HNO_3 acid. Dissolved JCp-1 were diluted in 7 ppm Ca concentration and *ca.* 3%HNO_3 with Milli-Q. JCp-1 solutions were stored in 0.5-1L PP bottle. 5mL JCp-1 solutions were dispensed from the bottle to 10mL PP centrifuge tubes. Calibration line from Intensity ratio$_{Me/Ca}$ to Me/Ca ratio were adapted on the analytical results of Intensity ratio$_{Me/Ca}$ in each sample solutions. Instrumental drift in Me/Ca ratio was de-trended using a best-fit curve estimated from running standard.

4-2 Application-1: Replicated measurement of JCp-1

4-2-1 Materials

As application examples, we conducted replicate measurement of JCp-1using our methods. We weighed JCp-1 and dissolved with 60% nitric acid. JCp-1 solution was diluted until 7 ppm Ca and 3% niric acid concentrations using Milli-Q. We measured two 3% Nitric acid as chemical blanks, 40 JCp-1 solutions as replicate samples and 10 JCp-1 solutions as running standards.

4-2-2 results

Our calibration line had a good correlation between intensity ratio and estimated Sr/Ca (r > 0.9999). Combination of Sr(421.5nm) and Ca(373.6nm) was the highest precision (0.102 %RSD, n = 40) in our consideration (Fig.4, tableS2). Sr/Ca combined with the most intense wavelength of Sr and relatively strong wavelength of Ca can be available under the negligible conditions of for solution in 7 ppm Ca concentration (Fig.1-b, Fig.2-c). The instrumental drift of Sr/Ca are -0.009 mmolmol^{-1}/hour (n = 40: r = -0.714; p < 0.01: Fig.4). After correction, the instrumental drift of Sr/Ca was negligible (slopes of corrected Sr/Ca vs. analysis time: -0.001 mmol*mol^{-1}/hour, r = -0.113, n.s.). Reproductivity of corrected Sr/Ca was 0.072 %RSD estimated from corrected 40 Sr/Ca values of JCp1. Sr/Ca - SST thermometer in Ishigaki Island was described as follows.

$$Sr/Ca = - 0.0608 \; SST + 10.5$$

SST error was within 0.105 ℃ estimated from the slope of thermometer in Ishigaki Island (-0.0608 mmol×mol^{-1}/℃: Mitsuguchi et al., 1993) and analytical error.

Our Sr/Ca method had already loaded 816 JCp1-samples in 34 sequences for 6 months. Average value and %RSD of uncorrected Sr(421.5nm)/Ca(373.6nm) ratio were 8.84 ± 0.10 mmol/mol and 1.12% (n = 816). Our absolute Sr/Ca values of JCp-1 agreed with 8.838 ± 0.042 mmol/mol measured by inter-laboratory studies [Hathorne et al., 2012].

4-3 Application-2: Weekly resolution SST reconstruction using Porites coral from Kikai Island, the northwestern Pacific.

4-3-1 Materials and methods

On October 26th, 2017, we collected a *Porites sp.* coral colony in Kikai island, Kagoshima, Japan (23°30′ N, 58°45′ E). This *Porites* colony was living at a %%m water depth in Somachi bay(?). The coral colony was sliced into 5-mm-thick slabs. We took X-radiographs of the coral slabs to identify the coral growth axis (Fig. S). We prepared a ledge in 2 mm thickness along the maximum growth axis and obtained coral powder from the ledge at 0.2 mm interval for geochemical analysis.

Analytical procedures were conducted same with section of 4-1 analytical procedures.

To compare Sr/Ca variations, we used logger-based SST (HOBO Water Temp Pro v2, accuracy: ±0.2°C) which captured SST from 2015 May in one-hour interval. SST logger was attached in the neighbor Porites colony. To supplement the lack of SST data in logger, we used logger-based SST dataset which were corrected at the nearest port from our sampling site. Maxima and minima of Sr/Ca were selected as anchor points and tied to minima and maxima of daily-SST, respectively. To obtain a time series with equidistant time steps, we resampled the Sr/Ca data at weekly resolution using AnalySeries Softwares, version 2.0.8. SST dependency of Sr/Ca was established using Sr/Ca and logger-based SST in anchor points. The regression slope was used for SST reconstruction on this study. To confirm the precision of SST reconstruction with Sr/Ca, we estimated the residual SST by subtracting the weekly logger-based SST from the reconstructed-SST.

4-3-2 Results and Discussions

We determined 3 annual cycles from 190 samples measurement using our methods (Fig.5). To compare logger-based SST data, we used for 3 annual cycles for this study. As a result of inserting time series, we get Sr/Ca records form 2017 October 27 to 2015 August 21. Averaged Sr/Ca was 9.05 mmol/mol. Maxima and minima of Sr/Ca were 9.53 and 8.71, respectively. SST dependency of Sr/Ca using anchoring data was as follows.

$$Sr/Ca = -0.0624 \times SST(°C) + 10.67 \ (R = 0.9990, p < 0.01)$$

A slope of our SST-Sr/Ca equations was similar with published slopes of SST-Sr/Ca dependency in Kikai island and

compiled equations by Correge, 2006.

The averaged residual-SST was 0.76ºC in all time-series. The standard deviation of residual SST was 1.49 ºC (1σ) in all time-series. Average and standard deviation of residual SST were 0.0± 0.29 ºC (1σ, n = 5) in anchoring points. In periods below mean Sr/Ca (high SST: summer), averaged residual-SST was 0.42 and standard deviation of this was 0.78. In periods over mean Sr/Ca (low SST or winter), averaged residual SST was 1.09 and standard deviation of this was 1.86. These results suggested that summer Sr/Ca variations would suit be reconstructed with higher precisions than winter variations. This residual SST would be affected by coral biological effect. Possible coral-biological effect on Sr/Ca was reported as eg. Sr/Ca in seawater [de Villers et al.,], pH in calcification fluids [Cohen et al., 2016], activity of semibent algae [Cohen et al.,], corallite orientations [Delong et al., 2013] and coral growth rate [Fallon et al., 2003]. Diagenesis (secondary aragonite cement: Hendy et al., 2004) and skeletal morphology on the analytical path [Cohen et al., 2004] also altered Sr/Ca ratio. Annual cycles of coral proxies were altered due to differences of coral growth between seasons. Sr/Ca could still provide high-precious and high-resolution SST variations, although Sr/Ca ratio might be altered by some coral biological effects.

5. Conclusions

To get higher precision of Sr/Ca analysis, the spectral wavelengths of Sr and Ca should be selected Sr (421.5nm) and Ca (373.6nm) with solutions in 7 ppm Ca concentration. These spectral wavelengths in Ca 7 ppm concentration were the most stable in other concentrations. ICP-OES and Sr/Ca as SST proxy widely spread. Our high precision analytical methods of Sr/Ca using small amounts of coral skeleton could help to widely establish high-quality and long term Sr/Ca records. Wide spreading of long term Sr/Ca could also help to reveal changes of global SST and hydro-circulations in interannual-centennial scales.

Method	%RSD (2σ)	Sample weight (μg)	Reference
ID-TIMS	0.05		Beck et al., 1992
ICP-OES	0.14	80-100	Our method
ICP-OES	0.16	500	Zinke et al.,2014
ICP-OES	0.16	-	Nurhati et al., 2009
ICP-OES	0.22	90-336	Delong et al., 2004
ICP-OES	0.3	500	Cahyarini et al.,2008
ICP-OES	0.4	50	Schrag, 1999
ID-ICP-QMS	0.5		Le Conrnec and Correge, 1997
ICP-OES	0.6	100-200	de Villers et al., 2002
ICP-SF-MS	0.9	5-10	Rosenthal et al.,

Previous analytical method of Sr/Ca in coral skeleton

Figure list
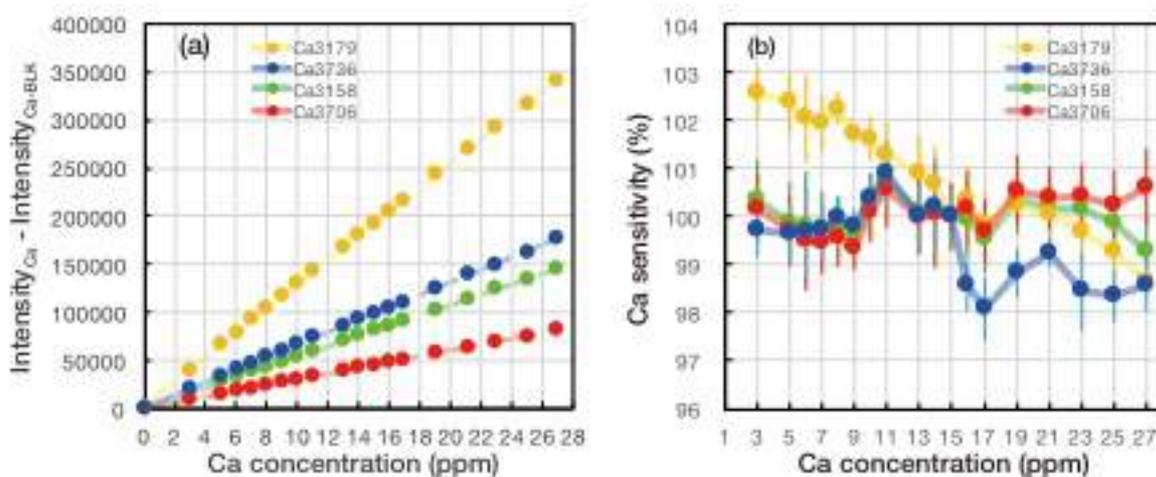
Fig.1 Intensity of Ca wavelength versus Ca concentration from 3 to 27 ppm (a), Ca-sensitivity versus Ca concentration (b). Ca3179 line showed strong curvature, and decreasing-trend as Ca concentration increased.
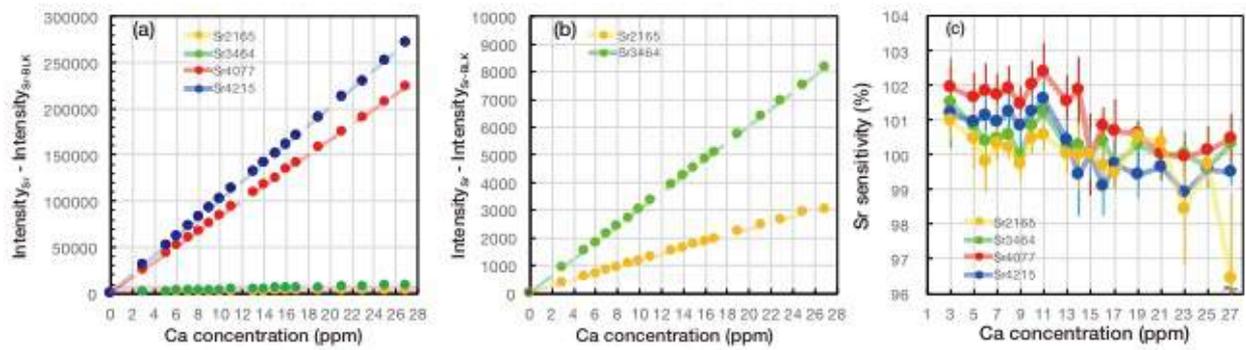
Fig.2.

The sensitivity and sensitivity of Sr results. Intensity of Sr wavelength versus Ca concentration from 3 to 27 ppm (a), Sr-sensitivity versus Ca concentration (b).

Sensitivities of Sr were gradually decreased without 5-9ppm Ca concentration.
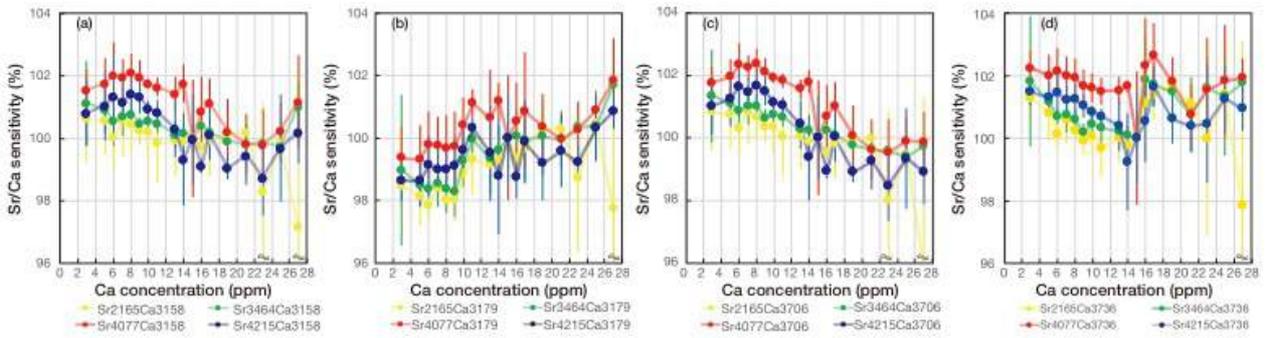
Fig.3

Sensitivity of Sr/Ca-intensity ratio results. Sr4215/Ca3736 intensity ratio was stable from 5 to 10 ppm Ca concentration.
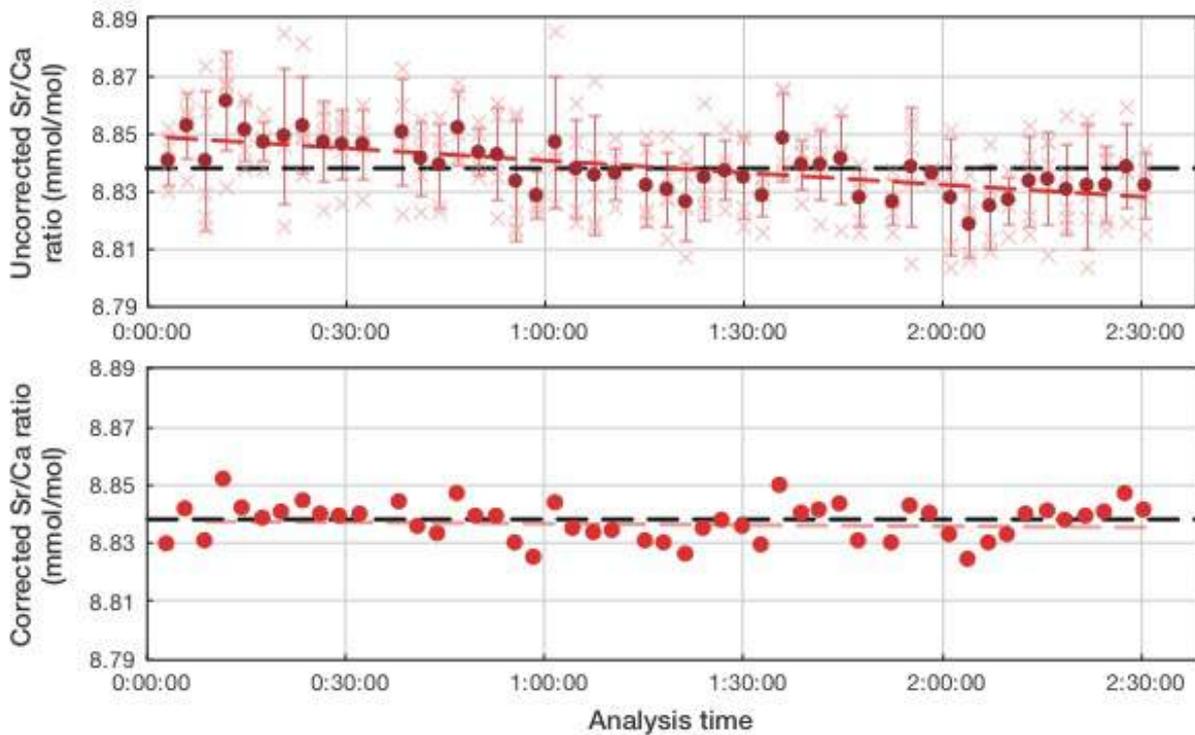
Fig.4

Results of test measurement using JCp-1 in 7ppm Ca concentration. Cross and circle dot showed 5 reprecation and averaged value respectively. Error bar showed standard deviation of 5-reprecation (a) Sr/Ca based on Ca3736 and Sr4215. Slope showed trend between Sr/Ca and analysis time. Black dot-line showed certified value of Sr/Ca in JCp-1 [Hathorn et al., 2012]. Red dot-line showed trend of Sr/Ca thorough 40 JCp-1.
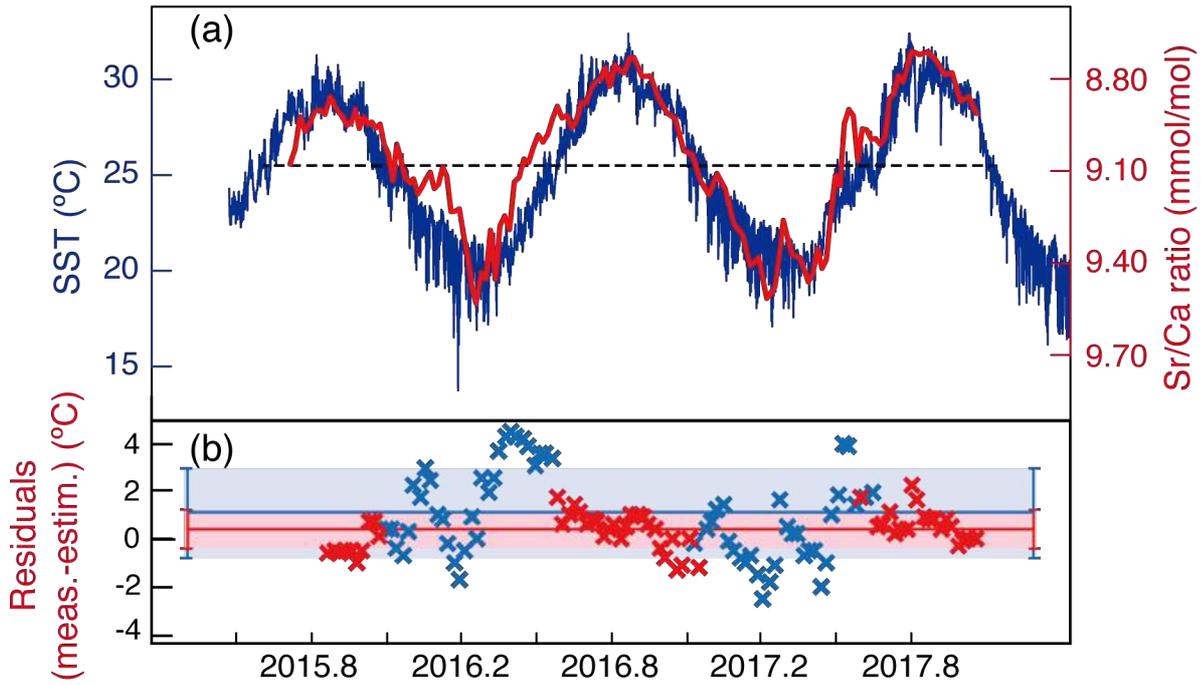
Fig.4

(a) Logger-based SST (blue line) and reconstructed SST using Sr/Ca ratio in coral skeleton (red line)

(b) Residual SST after subtracting the logger-based SST in weekly resolution from the reconstructed in weekly resolution SST. Red dot line was shown an averaged value of SST. Black dot lines were indicated standard deviations (1σ) of residual SST in full records of reconstructed SST.
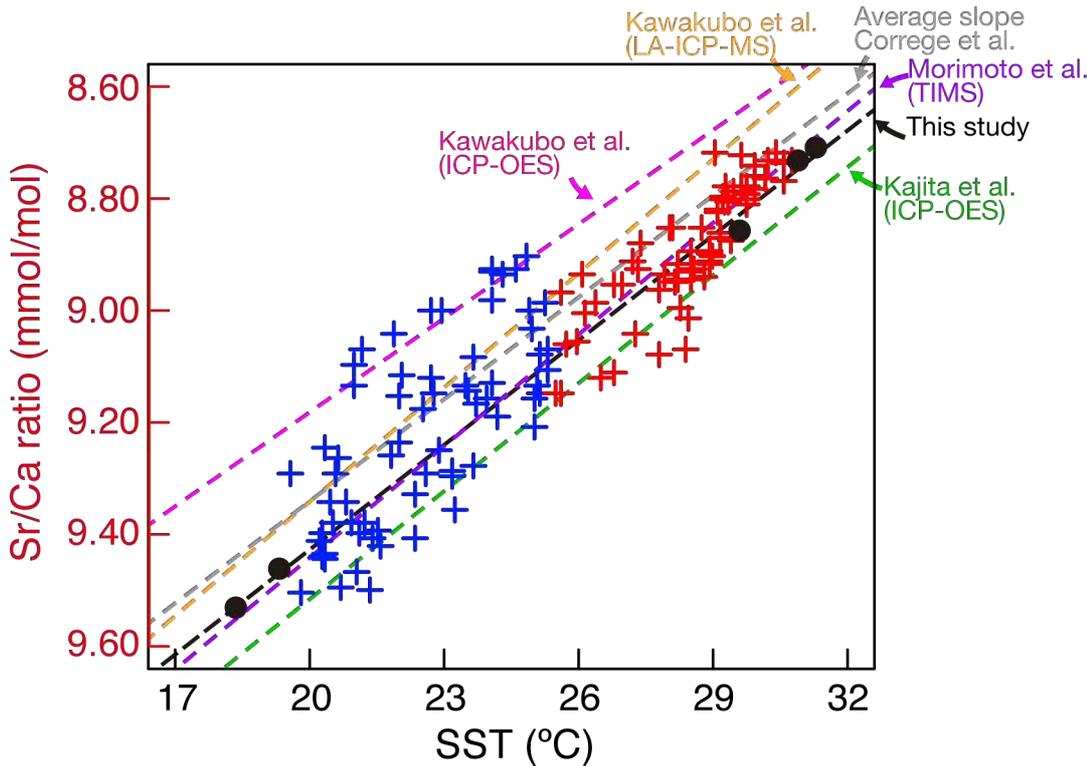
Fig.5

SST dependency of Sr/Ca ratio. Black dots showed SST and our Sr/Ca ratio in anchoring points. Red and blue crosses indicated Sr/Ca over averaged value and below that value, respectively. Equations of slopes and references were as follows

Sr/Ca dependency from Kikai island using ICP-OES: our slope (Sr/Ca = 10.673 - 0.0624 SST: black), Kajita et al. (2017): (Sr/Ca = 10.80 – 0.0643 SST: green), Kawakubo et al., 2014 (Sr/Ca = 10.3 – 0.056 SST: pink). Sr/Ca dependency from Kikai island using LA-ICP-MS: Kawakubo et al., 2014 (Sr/Ca = 10.7 – 0.068 SST: orange). Sr/Ca dependency from Kikai island using TIMS: Morimoto et al. (2007): (Sr/Ca = 10.77 – 0.0665 SST: purple). Average of published slope (Correge, 2006: Sr/Ca = 10.553 – 0.0607 Sr/Ca: grey).
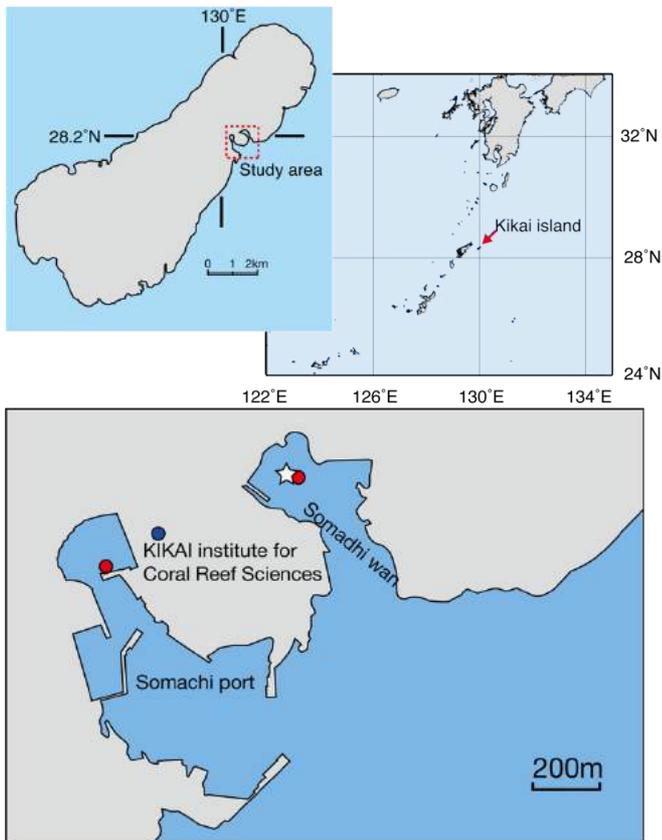
FigS1

Maps of coral specimen (white star) and SST loggers (red circles). The wide map (right upper panel) was generated by GMT. Detailed maps were modified and re-wrote from Google map and Sasaki et al., 2004.
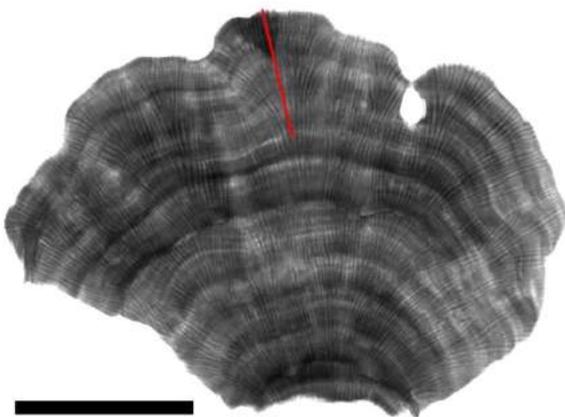
Fig.S2

X-ray image of our *Porites* coral specimen

Acknowledgment